Real time quantification of apical polarity protein reveals novel dynamic processes in lumenal network establishment and remodeling in the pancreas

Abigail Laura Jackson[1*], Silja Heilmann[1*], Christine Ebeid, Jelena Miskovic Krivokapic, Jose Alejandro Romero Herrera, Henrik Semb[1], Pia Nyeng[2]

1: The Danish Stem Cell Center (DanStem), University of Copenhagen, 2200 Copenhagen N, Denmark/Institute for Cell and Molecular Medicine (ICMM), University of Copenhagen, 2200 Copenhagen N, Denmark.
2: Institut for Naturvidenskab og Miljø/Medicinalbiologi/Molecular, Universitetsvej 1, DK-4000 Roskilde, Denmark.
3: Center for Health Data Science (HeaDS), University of Copenhagen, 2200 Copenhagen N, Denmark.

Corresponding author: pnyeng@ruc.dk
* co-first authors

Abstract

During embryogenesis dynamic changes in tissue architecture transform primitive anlages to functional organs. Here we document in real time how pancreatic lumens are derived and transformed using a new apical-polarity mouse reporter. Our 4D imaging data reveals dynamic remodeling of apical proteins and lumens to primarily drive each stage of pancreatic duct development. Furthermore, we pinpoint two unique transitions during lumenogenesis. Contrary to current "*de novo*" models of polarity acquisition, we show that expansion and rearrangement of the pre-existing central primary lumen drives early network growth. We also document how the endocrine promoting niche - a "plexus" of interconnected ducts - is resolved. We show that an arborized network forms by gradual closing of ductal loops, rather than via pruning. These highly novel tissue dynamics provide a new framework within which cell and molecular signaling can be investigated in order to better understand the interplay between organ architecture and cell fate.

Introduction

Tubes are fundamental building blocks of an organism and essential for the function of many organs that transport vital gasses and enzymes around the body. If tube formation is perturbed during embryonic development, congenital conditions such as pancreatic duct anomalies (Dimitriou et al. 2018), autosomal dominant polycystic kidney disease (ADPKD) (Bergmann et al. 2018), and polycystic liver disease (Cnossen and Drenth 2014) can manifest. Understanding how tubes form in development can help us better understand the process that goes awry in such congenital tube defects.

Tubulogenesis has been studied *in vitro* in 3D models based on cell lines such as the Madin-Darby canine kidney (MDCK) cells (Martín-Belmonte et al. 2008) and *in vivo* during organogenesis of the lung, salivary gland, pancreas and many more (reviewed in (Lubarsky and Krasnow 2003)1). Based on these studies, tube formation is traditionally divided into two main categories: A) tubes that emerge from an already polarized epithelium, and B) tubes that emerge independently from an un-polarised epithelium (Hogan and Kolodziej 2002). In (A) the center of a tube - the lumen - is created through processes such as budding (e.g., the lung) and wrapping (e.g., the neural tube). In (B) lumens form *de novo* either by cavitation (B1) where central cells undergo apoptosis (e.g., in mammary gland end buds (Debnath et al. 2002), by hollowing (B2) where cords of lumens form within cells, or by cells

acquiring “de novo” apical polarity (B3) (e.g. in 3D cell culture of MDCK cells, (Martín-Belmonte et al. 2008; Mangan et al. 2016)

The pancreas is an intriguing and complex endocrine and exocrine organ comprised of a branched network of tubes. To achieve a postnatal exocrine function the pancreas must form a tree-like ductal structure, ensuring that acinar derived digestive enzymes, fluid and bicarbonate can flow away from the terminal end buds, through the ductal network to the duodenum (Reichert and Rustgi 2011). The formation of this network and its subsequent remodeling is not fully understood. Congenital anomalies in pancreatic ductal morphology have been associated with symptoms such as recurrent abdominal pain, nausea and vomiting (Türkvatan et al. 2013). The inefficient drainage resulting from developmental defects in pancreatic ductal remodeling can ultimately cause inflammation and pancreatitis. In addition to this structural role, the remodeling pancreatic ducts provide a unique niche necessary for specification of endocrine cells during embryonic development (Löf-Öhlin et al. 2017; Kesavan et al. 2009; Bankaitis, Bechard, and Wright 2015; Azizoglu et al. 2017; Barlow et al. 2023). The duct begins as an epithelial evagination of the foregut endoderm at the center of which lies a central primary lumen (CPL). The CPL is thought to be formed from an outbudding of the foregut lumen during epithelial evagination. Unlike MDCK cells and other simpler branching organs, the pancreatic duct does not remain a simple, unilumenal structure. The secondary pancreatic multi-lumenal network is believed to be created ‘de novo’. It has been proposed that the latter process has four phases, beginning with 1) acquisition of apical polarity in a few scattered cells, followed by 2) formation of a microlumen between neighboring polarized cells and 3) merging of microlumens to form a connected network that eventually 4) connects to the central gut lumen. (Villasenor et al. 2010; Kesavan et al. 2009; Hick et al. 2009; Flasse, Schewin, and Grapin-Botton 2020)

Studies in the mouse show that from E14.5, the ductal system found at the center of the pancreas consists of a network of interconnected ducts, coined the ductal “plexus” (Bankaitis, Bechard, and Wright 2015; Dahl-Jensen et al. 2018; Villasenor et al. 2010; Kesavan et al. 2009). At the periphery of and connected to this structure, are a system of ramifying branches. The plexus resolves into a ramifying tree at perinatal stages by an unknown cellular mechanism. At the molecular level, the ductal transformation has been shown to depend on actomyosin contractility, as co-depletion of RhoA and Afadin arrests plexus remodeling (Azizoglu et al. 2017). Based on in-silico modeling and immunofluorescent staining of whole fixed specimens, Dahl-Jensen and colleagues proposed that superfluous

ductal connections are pruned based on the flux of fluid through the tube (Dahl-Jensen et al. 2018). At the periphery of the pancreas, a live imaging study has demonstrated expansion by lateral branching (Puri and Hebrok 2007). Based on lineage tracing and modeling, this process has been proposed to be driven by proliferating progenitor cells at the ductal termini (Sznurkowska et al. 2018). Immunostaining data points to a disparity between the inner lumen topology and the outer branching pattern of the epithelium, showing that one lobe/branch can contain several lumens at E11.75 (Villasenor et al. 2010). Based on this data it was suggested that lumen formation precedes external branching and that these two processes are likely independent (Villasenor et al. 2010) . This hypothesis is corroborated by the finding that outer branching morphogenesis, but not inner lumen formation, is perturbed by inhibiting extracellular matrix (ECM)-cell interactions (Shih et al. 2016). These data further indicate that only peripheral pancreatic cells in contact with the ECM can undergo branching morphogenesis. Thus, a combination of lumen remodeling and outer peripheral branching seems to underlie pancreatic ductal network morphogenesis. However, it remains unclear how these processes are coordinated to resolve the epithelium into an arborised structure consisting of single lumenal branches.

The unique phases of pancreatic tubulogenesis detailed above suggest that each transition is a highly dynamic process. Yet, with the exception of a few studies by ourselves and others (Azizoglu et al. 2017; Shih et al. 2016; Löf-Öhlin et al. 2017), the majority of research into murine pancreatic tubulogenesis have relied on static analyses. These histochemical data can provide an insight into overt changes in protein location and abundance in a developing epithelium. However, because the epithelium is captured in a static state, accurate information about protein dynamics and the hierarchy of cellular and topological events cannot be evaluated. To advance our understanding of mammalian tubulogenesis, we must observe and quantify the dynamics of lumenal network development. This can only be achieved through analysis of high frequency 4D (x, y, z, time) data. Most “real time” branching studies have been performed in either low frequency or only in 2D (Riccio et al. 2016; Mederacke et al. 2022; Metzger et al. 2008), but a few high frequency 4D studies in other species and models of branching organs exist and have contributed to the advancement of the field (Araújo and Llimargas 2023; Mullapudi et al. 2019; Scheele et al. 2017; Packard et al. 2013).

Thus, many gaps in our knowledge remain, especially about the transition between different lumenal architectures, because of the lack of dynamic data. With respect to the pancreas, the mechanisms driving peripheral, secondary lumenal network formation and growth are

unknown. Data from fixed tissue suggest that polarity is acquired de novo (Kesavan et al. 2009; Villasenor et al. 2010; Hick et al. 2009), but we do not know if all lumen growth is de novo, nor how polarity can be transmitted to surrounding unpolarized cells to enable plexus formation. Additionally, how the pancreatic plexus resolves to an arborized structure, and whether lumen formation and epithelial branching are coordinated remain unknown.

Here, we introduce a new mouse strain we created for the live imaging of apical proteins - the Muc1-mCherry fusion-protein reporter. Mucin 1 (Muc1) is a large transmembrane protein which is expressed at apical membranes and developing lumens of many branched organs (Lacunza et al. 2010; Sakurai et al. 2007; Chambers et al. 1994; Fanni et al. 2012), including the pancreas (Cano et al. 2004; Kesavan et al. 2009; Villasenor et al. 2010; Kopinke and Murtaugh 2010), with the exception that it is mislocalized in cancer (Bafna, Kaur, and Batra 2010; Luan et al. 2022). Muc1 is heavily glycosylated on the extracellular N-terminal domain and interacts with multiple signaling pathways on the intracellular side (Bafna, Kaur, and Batra 2010).

In this study we use the Muc1-mcherry reporter in combination with other reporters to uncover unique mechanisms driving pancreatic lumenogenesis. We confirm that the CPL is derived from an outbudding of the foregut, but show that the budding lumen does not remain patent during this process. Contrary to previous models we observe that the secondary pancreatic lumenal network is primarily generated from a highly dynamic expansion and rearrangement of the pre-existing CPL, rather than *de novo*. The fusion of disparate lumens results in a network of interconnected ducts - a pancreatic plexus - that contains multiple loop structures, which provide several unique pancreatic progenitor niches depending on their size. We discovered that the plexus is resolved by a novel mechanism, which we term "loop-closing". Measurements and modeling indicate that loop closing is correlated with specific topological and spatial features.

Overall our study provides real time observations of highly novel tissue dynamics during pancreatic organogenesis. By providing a new dynamic framework for lumen network formation and transition we hope future studies will be well placed to decipher how organ architecture and cell fate are interconnected at a cell and molecular level. In addition we provide a new tool for visualizing apical polarity proteins in real time and believe our Muc1-mCherry reporter will be of great benefit to the cell polarity, development and cancer research communities.

Table 1: Definition of descriptive terminology:

Topological structure (abbreviation)	**Synonym**	**Text Description**	**Visual description**
Nascent lumen	N/A	An area of epithelium where consecutive Multipotent Pancreatic Progenitors (MPPs) are apically polarized but no space is visible between facing MPPS.	*Fig S4 D-H, filled arrows*
Central Primary Lumen (CPL)	Primary Central Lumen (PCL, (Villasenor et al. 2010)	The initial lumen that forms by budding at the center of the pancreatic bud at E9.5-E10.5. Although patent at the beginning, this lumenal patency is not consistent during the entire period of growth. At its most mature the CPL has a shape that echoes the stalk and head of the outer epithelium. The CPL just prior to transformation ca E10.5 is a variably patent lumen with a mushroom like shape.	*Fi2 3i-iii and Movie 2 (explant data), Fi2 BiI-iV and Movie 4-6 (in vivo data)*
Secondary foci/microlumens/network	Peripheral lumina (Villasenor et al. 2010; Hick et al. 2009)	Apical proteins and lumens that form subsequent to the initial CPL. In studies using fixed tissue these appear at a distance and disconnected from the CPL. Our dynamic data demonstrates that they primarily stem from the CPL and already formed lumens.	*Movie 14*
Outer epithelial bud morphology (not lumen), summarized from (Villasenor et al. 2010)	N/A	E9.5: fin like E10.5: fist like E11.5: teardrop like	N/A
Lumenal Category 1:lumenal extension - unidirectional (LEU)	N/A	A continuous lumenal structure that in 4D imaging maintains its topology as one entity, and (in 4D) over multiple time frames can be seen to extend in proximal distal length.	*Fig 3Ai, ii and iv and Movie 12, single tracking spot marking a lumen*
Lumenal Category 2: lumenal extension - bifurcation (LEB)	N/A	A continuous lumenal structure forms a second lumenal branch, seemingly by budding, at its apex. This bifurcated topology frequently extends the	*Fig 3Aii, iii and iv Movie 12 two*

		proximal distal length of the network. In some instances one of the lumenal bifurcates can also regress, so the lumenal branch returns to being a singular topological entity.	*tracking spots marking a lumen*
Lumenal Category 3: Lumenal break points - temporary (BPT).	N/A	A continuous lumenal structure that becomes dis-continous, topologically separating into 2 or 3 parts. In 4D data these parts usually remain in close proximity and will eventually (during the period of imaging) unify to become one continuous lumen again.	*Fig 3Bi-iv Movie 13*
Lumenal Category 4: Lumenal break points - permanent (BPP).	N/A	A continuous lumenal structure that becomes dis-continous, topologically separating into 2 or 3 parts. In 4D data one or more of these parts will often become displaced from the others. The displaced fragment will form a new area of peripheral lumenal growth that (during the period of imaging) will not immediately unify with the original fragments.	*Fig 3Ci-iv and Movie 14*
Lumenal Category 5: Contribution by Derived Foci. (DF)	N/A	Apical protein located <10uM from the nearest lumen/nascent lumen. The close proximity (an average cell length, (SFig 5F) of the foci to an existing apical membrane suggest it is likely to be derived from a polarized MPP.	*Fig 3Dii-iV and Movie 15 (blue tracking spot)*
Lumenal Category 6: Contribution by De Novo Foci.(DNF)	N/A	Apical protein located >10uM from the nearest lumen/nascent lumen. The distance between the foci and an existing apical membrane suggest it is likely to be generated by a non polarized MPP i.e. *De Novo*	*Fig 3Di-iV* and *Movie 15 red tracking spot.*
Secondary lumenal network (SLN)	Peripheral lumenal network/pre-plexus network	A multi-lumenal structure primarily derived from the transformation of the CPL and contributed to by some *de novo* apical lumen generation. Overall the structure is morphologically a mix of forming loops, disconnected lumenal fragments and continuous	*Fig 2 Ci-iv, Movie 7b*

		branches. The secondary lumenal network can be observed from E10.0-E11.5, most frequently after E11.0.	
Plexus (Bankaitis, Bechard, and Wright 2015)	Ductal network	A network of interconnected ducts derived from the secondary lumenal network in mid-late gestation. At this stage the lumen is patent, connected and contains loop structures.	*Fig 4A*
Mature ductal system	Ductal tree	An arborized tubular duct system derived from the plexus. This is the final postnatal stage of pancreatic tubulogenesis and remodeling where most loops are thought to have been resolved. It is part of the exocrine compartment and drains enzymes from the acini into the duodenum.	N/A
Loop	Plexus unit	Epithelial tubes that form rings while staying connected to the rest of the network. Has the same topology as a roundabout.	*Fig 4E-G* (*in vivo*), *Fig 6A* and movie 21 *(in vitro, live)*
Inner hole	N/A	The volume in the middle of the loop. Analogous to the central island in the middle of a roundabout. Contains ECM and epithelial or mesenchymal cells.	*Fig 4E-G* and SFig8A and D (*in vivo*)
Loop-closure	Plexus remodeling	Gradual constriction of loops. Will gradually diminish the inner hole volume/area.	*Fig 6A-B* and movie 21-22 *(in vitro, live)*
Inner network/tree	N/A	*The topology of the lumens*	*Fig 8Aiii-iv and Fig 8 Ciii-iv*
Outer network/tree	N/A	The topology of the epithelium	*Fig 8Ai-ii and Fig 8Ci-ii*

Results

Generation of a novel Mucin1-mcherry apical reporter mouse for live imaging

To visualize endogenous Muc1, and thereby apical polarity, we created a BAC transgenic mouse expressing a Muc1-mCherry red fluorescent fusion protein. Upon translation, this apically targeted fusion protein absorbs light in the range of 540-590 nm and emits light in the range of 550-650 nm (Shu et al. 2006). mCherry was chosen because of the protein's fast maturation, high photostability (Shaner et al. 2004) and compatibility with GFP based reporters. The 171 kb BAC RP24-365K20 spanning the Muc1 gene was ordered from BACPAC Resources Center at Oakland Research Institute.

The construct was created by BAC recombineering using galK selection (Warming et al. 2005) (see Fig 1A for the targeting strategy). To maintain glycosylation at the N-terminal, the *Muc1* gene was targeted in frame at the intracellular C-terminal. Three rounds of mouse oocyte injections gave rise to five transgenic founder animals. One female founder was infertile, and the remaining four founders were named Muc1-mcherry 0M, 5M, 12M (male founders) and 2F (female founder). Transgenic offspring from the 0M lineage were smaller at birth and born at a 25% sub-Mendelian ratio. The other lineages were viable, fertile, phenotypically normal and born at expected Mendelian ratios. At 8-9 weeks of age the weight of most transgenic mice was not significantly different from their non-transgenic littermates. A few exceptions were females from the 0M and 5M substrains and males from the 2F substrain that had a slightly reduced weight compared to non-transgenic littermates (SFig1 A, C, E, G).

Expression of Mucin-mCherry was detectable in multiple internal organs including the pancreas, intestines, stomach and lung (Fig 1B-C). In freshly isolated adult tissue, the mCherry fluorescence could be detected in adult pancreas, colon, duodenum and lung by fluorescence microscopy (Fig 1B-E). After paraformaldehyde fixation, mCherry fluorescence was still detectable and closely resembled Muc1 antibody staining at embryonic and adult stages (Fig Fi-Kii). mCherry was expressed on the apical membrane of the cells lining the apical membranes in the intestine, stomach, lung and pancreas (Fig 1Fi-Kiii). We did occasionally observe structures (arrowhead in Fig 1Ii and Iii) that were mCherry positive, but did not stain with the Muc1 antibody. As this fluorescence was found along ductal structures, we ascribe this difference to a higher sensitivity of the reporter which contains an amplified pmCherry-N cassette, that enables low level endogenous Muc1 expression to be detected.

Our model system for understanding how epithelial organs generate tubes is the embryonic pancreas. To establish that introduction of the BAC had no effects on pancreatic architecture and differentiation, we performed whole mount (WM) staining for Mucin 1 (Muc1), Insulin (Ins) and E-cadherin (E-cad) in E14.5 pancreata, visualized pancreatic architecture and quantified the relative volumes. We did not find any significant changes in transgenic embryos from any substrains as compared to wild type (WT) littermates (SFig 2). We further confirmed that the fasting blood glucose of transgenic mice was normal at 8-9 weeks, indicating that the pancreas was functioning normally (SFig 1 B, D, F, H).

We successfully detected mCherry by live-imaging of explanted embryonic pancreas and lung from reporter mice by confocal microscopy (Fig 1Li-Mii). Live-imaging of *ex vivo* cultured dorsal pancreas from each substrain revealed a lower mCherry expression in the 0M substrain, and a delayed onset in the 5M substrain (results not shown). However, the 12M and 2F substrains had comparable, strong, Mucin-mCherry signals, detected in pancreatic explants that reflect the *in vivo* onset of endogenous Muc1 expression at E9.5 (Movie 1 and Fig 1Ni-Oiii). Pancreas ductal development and branching appeared normal in explant cultures from all substrains at all stages of culture compared to explanted pancreas from reporter-negative littermates (Fig 1Li-ii and Ni-Oiii and SFig 2). We henceforth proceeded using the 12M substrain, unless otherwise denoted in the figures.

The pancreatic central primary lumen is derived from outbudding of the foregut, followed by stochastic apical domain maturation, and reduction of lumenal patency.

Literature states that the lumenal network is derived from two independent processes at the beginning of pancreatic bud development: CPL budding and the merging of *de novo* formed microlumens (Hick et al. 2009; Villasenor et al. 2010). However, we lack information about the spatiotemporal dynamics surrounding early lumen network growth. And so, questions remain about how these two independent lumen generating processes can become unified into one continuous lumenal plexus.

First we aimed to define the spatiotemporal dynamics of (CPL) budding using the Mucin1-mCherry reporter. To do so we established a protocol for live imaging embryonic day (E) E9.75 to E10.0 foregut explants (see methods). We imaged live explants expressing Mucin-mCherry to determine the origin of this structure and to visualize, in real time, how the CPL is shaped as the pancreatic epithelium evaginates from the foregut. Intriguingly,

there was no detectable expression of Mucin-mCherry in explanted E9.75 pancreatic buds at the onset of imaging *(Movie 1 & SFig 3ai, asterisk highlights a lack of signal in the bud after 9 hours of imaging)*. To confirm that this observation was not an artifact of the 4D imaging, we analyzed the pattern of endogenous Mucin protein by whole mount immunofluorescence (WMIF) in E8.5 to E10.0 pancreata (data not shown). We corroborated that before E10.0, the *in vivo* gut tube does not express Mucin. At E10.0 Mucin was detected in polarized cells most distal to the foregut (i.e the forming CPL) *(SFig 3eii pink dashed line)*. In contrast ZO1-GFP was expressed in the CPL head, stalk (proximal and connecting to the foregut) and the foregut itself, *(SFig 3 eiii green dashed line and large green brackets)*. This pattern of Mucin-mCherry acquisition in the pancreatic epithelium more distal to the foregut was also evident in the 4D movies of E9.75 early pancreatic lumens. In *Movie 1 and SFig 3* Mucin-mCherry reporter first appears in the most distal area of the evaginating bud (e.g. white arrow arrows in *SFig 3aii show Mucin foci close to the mesenchyme*) and over time is acquired more posteriorly, i.e. in pancreatic epithelium closer to the foregut (*SFig 3aiii and iv).*

The pattern of Muc1 localisation could indicate that all lumens are formed *de novo*, with the first microlumens initiated at the site where the CPL forms. However, immuno-histochemisty stainings for alternative apical proteins shows their apical expression throughout the CPL cap (white dashes), stalk (yellow dashes) and into the foregut *(Fig 2bii-iv (Movies 4-6) and SFig 4aiiii, aiv EZRIN and SFig 4ai, aii ZO1-GFP.* aPKCi not shown). Interestingly, orthogonal cross sections through 3D maximum intensity projections (MIPs) of foregut epithelia highlighted a distinction between pancreatic and other epithelial with patent lumens i.e. reported in the lung bud. In S*Fig 4Dii-Gii* one can appreciate that CPL patency (open arrowhead denotes lumenal space/patency, filled arrowhead denotes no lumenal space/no patency) is variable across all CPL morphological stages (3D MIPs S*Fig 4Di-Gi),* with a trend toward earlier stages being more patent. The amount of patency also varied within samples S*Fig 4Hi-Hiii*, reflecting that the loss (and regaining) of lumenal patency is a dynamic process occurring over time.

Thus we concluded that the Mucin-mCherry reporter faithfully depicts endogenous Mucin - or lack thereof - in the early pancreatic bud. The 3D morphology of the CPL visualized by EZRIN, ZO1 and aPKCi (not shown) expression in fixed pancreata suggests, as per the dogma from 2D imaging data (Hick et al. 2009), that the CPL forms from an outbudding of the foregut lumen. To validate this hypothesis with dynamic data we utilized a second reporter

line in which Zona-Occludin 1 is fused to green fluorescent protein (ZO1-GFP) (Foote, Sumigray, and Lechler 2013).

In the early (pre-midgestation) pancreatic epithelium ZO1 is localized to apical membranes (Villasenor et al. 2010; Hick et al. 2009). We isolated and imaged ZO1-GFP expressing dorsal foreguts from E9.5-10.0 where pancreatic dorsal or ventral bud evagination had not yet fully occurred. We found that ZO1-GFP marked the entire CPL and observed that the CPL's growth mirrors the shape and direction of the evaginating epithelial tissue *(Movie 2, Fig2Ai-iii)*. We also observed a distinct 'fast moving' ZO1-GFP signal in the movies that appeared to be expressed outside the epithelial bud. We hypothesized from the movement and morphology of this 'extra epithelial' signal that it could be marking a type of blood cell or vessel. To test this hypothesis we fixed explants directly after live imaging, stained them for the endothelial PECAM and compared the shape of the PECAM marked signal to the ZO1-GFP signal. In Fig S5AandB we can see that the Mucin (Magenta) marked lumenal shape matches the bright ZO1-GFP in the center of the live imaging frame (SFig 5C).In Fig S5A we can see that the Mucin (Magenta) marked lumenal shape matches the bright ZO1-GFP in the center of the live imaging frame (SFig 5C). Moreover there is no overlap between the PECAM and Mucin (compare SFig5Ai and Bi). Conversely, there is high overlap between the endogenous ZO1-GFP signal seen outside the epithelial bud (red dashed outline *SFig 5Ci*) and the Pecam signal (red dashed outline *SFig 5Bii*). Thus we conclude that ZO1-GFP is also expressed in the endothelial cells surrounding the pancreatic epithelium, but that the dynamics of this signal distinguish it from the apically expressed epithelial ZO1-GFP signal.

During this medial-lateral growth toward the mesenchyme, the CPL remains perpendicular to and continuous with the foregut lumen *(insets of Fig 2Ai-iii show overview of the gut tube during CPL budding)*. The gradual budding morphology that forms the cap and stalk of the CPL *(Fig 2bii-iv (Movies 4-6)* was also detected *in vivo* by WMIF. By imaging ZO1-GFP and Mucin-mCherry double positive foreguts *(SFig 3Bi-iii overview)*, we were able to observe the same hierarchy of Mucin and ZO1 expression observed in WMIF stainings (e.g.S*Fig Ei-iv*). In single orthogonal slices through the evaginating dorsal bud (panels *SFig 3Ci-iii, MIP inset)* one can see Mucin-mCherry is highly co-expressed with ZO1-GFP both in the cap (*S3Ciii* white arrow) and stalk (*SFig 3Ciii* yellow arrow) of the CPL. In contrast, single orthogonal slices through the newly evaginating ventral bud (panels *SFig 3Di-iii, MIP inset)*, there is minimal co-expression in the distal cap of the CPL *(SFig 3Diii white arrow)*, and no detectable co-expression in the CPL stalk (*SFig 3Diii yellow arrow*). Thus, we conclude that a hierarchical

protein expression pattern exists, where first ZO1-GFP is expressed apically t in the entire CPL and foregut, in both dorsal and ventral buds. Subsequently Mucin-mCherry is acquired, when the lumens are more developmentally mature, often first detected in the distal cap of the dorsal bud's CPL.

From these live imaging data we conclude that the CPL forms from an apically polarized, patent lumenal tissue (the foregut) via budding. Importantly, we were also able to show in WMIF stainings of E8.5-E10.0 pancreatic buds that these morphological lumenal changes are also present *in vivo*. Combined our live and WMIF data also suggests that during budding the CPL is stochastically remodeled to reduce lumenal patency whilst increasing apical domain maturation, defined by Muc1 expression.

CPL remodeling marks the onset of a secondary, multi-lumenal network growth

Our next aim was to utilize our live imaging reporters to visualize, define and quantify the generation of a multi-lumenal, secondary network. First we wanted to test the hypothesis that this network forms by fusion of de novo generated foci, located peripheral to the CPL. Thus, we focused on analyzing ZO1_Mucin reporter expressing explants, (ca E10.0-E10.5) in which the CPL was identifiable but no peripheral lumenal sites were evident. Movies sampling lumenogenesis at 8 minute intervals in dorsal and ventral pancreatic buds displayed a consistent pattern of topological changes. In all datasets, the first event to occur to initiate the network was a remodeling of the central primary lumen *(Movie 7a and 7b)*. At the initiation of imaging each explant's CPL had an ellipsoid morphology *(Fig 2Ci).* Over time the ellipsoid CPL thinned in width, extended in length, and became bifurcated/branched (*Fig 2Ci-cii* yellow and white arrows show CPL branching). Apical foci could be detected at distance from the CPL at the initiation of imaging. However, these distant foci did not appear to simply merge together to establish a secondary network. The foci behavior was much more variable and seemingly unpredictable *(Movie 7a and 7b)*; some never contributing, others merging directly to an established lumen (*Fig 2Civ* red arrow) and some merging together at later stages of imaging *Fig 2C ii and iii* blue arrow). In addition, some foci were found at close proximity to an existing lumen (<10 µm i.e. less than average cell length as quantified from data shown in SFig 5D). Other foci were located distal to any lumen (>10 µm i.e. less than average cell length as quantified from data shown in SFig5 D). We termed foci derived if they were found <10 µm from a lumen and thus likely from an already polarized cell. Conversely, we termed foci de novo if they were found >10 µm from a lumen and thus were likely generated de novo by an un polarized cell.

Another novel event evident in these live imaging datasets is the breaking apart of continuous and re-unification of disparate lumenal structures discussed further in the next section (e.g the lumenal structure highlighted by the yellow arrow in *Fig 2Cii-iv*).

CPL remodeling and branching was also evident *in vivo,* prior to a peripheral lumenal network establishment (white arrows in Fig *2Biv and 2Di)*. *Fig 2Di (Movie 8)* shows an E10.5 whole mount pancreata in which the CPL is transformed (no longer ellipsoid) and projects nascent lumens distally (white arrows). Foci are detected proximally (blue arrow) and distal (red arrow) to the CPL but no peripheral lumens are observed. We conclude that these nascent lumenal CPL extensions, visible in 3D *in vivo* epithelia, are likely a static depiction of lumenal continuity seen in the live data. Importantly these nascent lumenal projections are visible before the appearance of secondary lumenal sites, supporting our *ex vivo* observations. Together these data lead us to conclude that CPL remodeling is the first event in the establishment of a secondary lumenal network.

Diverse morphological events contribute to CPL remodeling and subsequent growth of the peripheral network

From our 8-minute interval live imaging datasets it was clear that diverse morphological events occur to generate a multi-lumenal pancreatic network, whose growth is not stereotypical. We observed six categories of lumenal behavior: lumenal extension - both 1) unilateral and 2) bilateral i.e a bifurcation *(Fig 3Ai-iv and Movie 12)*, lumenal break points - 3) temporary and 4) permanent *(respectively Fig 3Bi-iv and Movie 13, Fig 3Ci-iv and Movie 14)* and foci contribution- 5) derived and 6) *de novo (shown together in Fig 3Di-iv and Movie 15).*

To validate our ex vivo live imaging observations, we analyzed lumenal morphologies in fixed whole mount pancreata at stages of development spanning our live imaging data. Importantly, we were able to identify lumenal structures reminiscent of those categorized by their live behavior. We observed that overall the remodeled CPL and secondary network had highly comparable morphology over developmental (E10.5-E11.5, Movies 8-11) and imaging time of ca. 20 hours (Movie 7a and *Fig 2, Ci vs 2Di, Cii vs 2Dii, Ciii vs Diii and Civ vs Div).* As time proceeds (both developmentally and in real time) the CPL becomes increasingly extended and branched, remodeling to form a singular lumenal branch (dashed white line in *Fig 2Diii and Div, annotated CPL in 2Ci-iv*). Interestingly, this lumenal branch remains in

contact with the foregut lumen (dashed yellow line in *Fig 2Diii and Div, annotated CPL in 2Ci-iv).* Overall the WMIF samples echo the live data's transition from single transformed lumen (*Movie 8* and *9*), to disparate lumenal sites (*Movie 10*) into a more unified pre-plexus structure (*Movie 11)*. Analyzing the WMIF samples in more detail we found examples of unilateral (white open arrowhead *Fig 2Di-iv*) and bilateral (white filled arrowhead *Fig 2Dii-iv)* lumenal branches. Comparing fixed 3D samples with our live imaging data we find it credible that many of the 'disconnected' secondary lumenal sites (yellow arrowheads *Fig 2Dii-iv)* and foci visible in fixed tissue are static depictions of dynamic remodeling events. For instance, one can appreciate in the WMIFs the proximity between nascent extensions from the CPL and secondary lumenal sites *e.g. Fig 2Di boxed area and Movie 10.* Thus rather than forming de novo, many of these secondary lumenal sites in live data would likely be generated from lumenal breakpoints and derived foci.

Lumenal network growth and transformation largely occurs by remodeling of the central primary lumen

In order to directly measure how much of the secondary network derives from lumen remodeling events we recorded high frequency live imaging, 4 minute interval datasets. We tracked three 4 minute interval imaging datasets that capture varying early stages of secondary lumenal network growth, i.e. CPL to secondary lumenal network. In all explants at the start of imaging the CPL was still identifiable and during recording we observed all six categories of lumen events. Importantly, tracking of each category of lumenal event was feasible, including tracking foci which was not possible in the 8 minute interval data.

In each dataset we picked a minimum of 6 lumenal branches visible at the last time point of imaging to manually track. To simplify the tracking we chose to only follow the proximal-distal growth (CPL toward mesenchyme) and transformation of a lumen. In Imaris we used the spot function to manually track every category of lumenal event occurring per branch on a time frame basis (*Movies 16A-C*). In order to classify foci as derived or de novo, we measured the distance of each foci to a pre-existing lumen *(SFig 6D and E)*. To visualize how coordinated in time each lumenal event is, at the explant level, we devised a new way to integrate the data as a tracking plot. The tracking plot is a convenient but elegant way to visualize complex dynamic data counts in a static plot *(Fig 3E, SFig 6F & G)*. Each tracked lumenal branch's continuous growth over time is displayed horizontally across the X-axis of the plot. Bifurcation points resulting in another tracked lumenal branch are visualized by a perpendicular solid line from the mother lumenal branch. Any BPTs occurring in the branch

are visualized by a dashed line above the branch, so both their frequency and persistence in time can also be gauged. In order to simplify the plot we chose to only mark the time frame at which derived (circles) and de Novo Foci (squares) appear to contribute to the lumen. Thus the plot only summarizes the frequency with which foci contribute to a lumenal branch. By viewing all the tracks in the plot simultaneously we were unable to detect any pattern or symmetry in the lumenal events occurring within one explant. Thus, we believe that lumenal events within one branch occur independently and are likely regulated at the cellular level *(e.g. Fig 3E, BPT dashed lines persist for variable times in each lumenal branch).* Furthermore, the independent remodeling of each lumenal branch also indicated that the events are unlikely an artifact of explant culture.

From the tracking data, we quantified the collective frequency of the events across all three explants and statistically tested that they were not likely to have occurred by chance (chi squared test df 67.26, P value <0.0001. The quantitative data showed us that pre-existing lumenal structures were observed most frequently in the tracked network (*Fig 3F, BPTs and derived foci)*. Of the total events tracked and counted, 64% were BPTs, 26% were derived foci and only 3.5% were de novo foci (366, 149 and 20 events out of 570 respectively). To determine the frequency with which a lumenal event contributed to the network, we analyzed how persistent these events are over time. Both BPTs (*SFig 6A)* and derived foci (*SFig6B*) were much more transient in nature than *de novo* foci (*SFig 6C*). On average BPTs and derived foci had approximately 10 fold lower duration time in the network than *de novo* foci (average duration time respectively of 15.6 and 17.6 versus 155.6 minutes). Whilst our data on duration of each lumenal category is only correlational, it is tempting to speculate that unique cellular behaviors regulate the generation, retention and contribution of *de novo* foci in the network.

One additional lumenal category - also likely to have a unique mechanism of cellular regulation - was not represented in the tracking plots. Across the 3 imaged and tracked explants we detected 35 permanent lumenal break points events. Although permanent lumenal break points were only observed in 6% of total events (35/570) they still appear more frequently in the network than de novo foci. It is important to highlight that the permanent breaking apart of a once continuous lumen can foster new unique sites of lumenal network growth. Again, if viewed statically these BPPs would appear disconnected from the original network and lead to the reasonable hypothesis that they were derived from the fusion of de novo foci and microlumens. However, our live data observations contradict this and show that transformations of already polarized lumenal structures drive

secondary network generation. Once this naive, often disconnected primitive network is generated it begins to transition to a more unified structure. An example of this can be seen in the tracking plot in *Fig 3F* data and *Movie 16A* where branch 5 (cyan) can be seen to merge into and contribute to branch 6 (purple). The secondary network transitions to become a unified, multifurcated structure containing many loops, termed the plexus. As with all the stages of morphological change we have defined so far, the transition from one to the next is not binary but happens gradually and often in concert with other stages of transformation. The formation and resolution of loops during the transformation of lumenal plexus to arborised network is a phenomena we analyze in detail below.

Epithelial loops of varying sizes provide unique pancreatic progenitor niches

During tip-trunk patterning the embryonic pancreas creates a unique lumenal network - the plexus - that shapes and defines the trunk region. The plexus consists of multiple interconnected lumenal loops (see definition in Table 1) which are primarily located within the endocrine rich trunk region (Bankaitis, Bechard, and Wright 2015). Thus, it has been hypothesized that the loops could provide a unique niche within which endocrine progenitors are specified. Here we characterize loop formation and properties based on live imaged explants and fixed 3D samples.

Loop formation happens by lumen fusion and can be observed in all lumenal network live imaging datasets post CPL transformation, (e.g from ca E10.75 onwards). Examples of loop formation at early stages can be seen in *SFig 7A-C* and movie 17 and at later stages in *SFig 7D* and Movie 18). Thus, loop formation is not specific to any particular stage during formation of the secondary network.

To define the spatiotemporal distribution of loops and their size distribution within the interconnected plexus, we focused our analysis on late gestation pancreata, when loops are frequently observed (*Fig 5Ai*). We segmented the lumenal network in three different sample types (illustrated in *Fig 5B*): Fixed whole mount E14.5 organs stained with Muc1 and E-cadherin (*in vivo* fixed), were compared to organs explanted at E11.5-E12.5 and grown *ex vivo* for up to 4 days. The latter were fixed and stained for Muc1 and E-cadherin after 3 days of culturing (fixed *ex vivo*), or imaged as live explants starting 48 hours post explanting (live *ex vivo*). For the latter, only approximately one quarter of the total pancreas was kept in the field of view and tracked. We used a random forest based method for segmenting lumens in 3D images of fixed and immunostained samples and a semi-automated feature based

method for segmenting lumens in 3D live imaging data. The segmentations (*Fig 5Ai*) were used for creating midline skeletons and identifying loops (*Fig 5Aii*).

We first confirmed that the loop size distribution between our three different sample types were comparable, signifying that we are analyzing a biologically relevant sample of the loop structures in the live imaging experiments. In all sample types, loops were detected in a range of sizes over four orders of magnitude from approx. 10 μm^2 to 100.000 μm^2 inner hole area (*Fig 5C*). We choose to divide the loops into four size categories based on the combined size feature, as explained in materials and methods section: Small (S, blue, 0-90 μm^2 inner hole area) Medium (M, orange, 90-260 μm^2) Large (L, yellow, 260-505 μm^2) and extra large (XL, purple, from 505 μm^2 and above) as exemplified in figure *5Ei-Gii*.
Our live imaging experiments showed that formation of new loops occurs in all four size categories but is more common in the two smaller size groups, where ~87% of all new loops are formed, S (56,4%), M (30.4%), L (8.3%) and XL (4.9%). We find that loop structures in the late gestation network can form in two topologically different ways 1) without a pre-existing loop, through merging of two lumenal extensions (*Fig 6A*, *SFig 7D* and movie 18) and 2) when an already existing loop structure 'cinches' in the middle to form two smaller loops (*Fig 6D* and movie 20). Lumen merging leads to new loops in all size categories (*Fig 4Di*), while cinching leads to new loops only in small-medium sizes post-cinching (*Fig 4Dii*). When a loop cinches in two, we record the largest as a continuation of the old loop, and the smallest as the new loop. Cinching thereby contributes to overall loop size reduction, as the loops were in sizes M-XL pre-cinching (*Fig 4Diii*).

We further determined that loops of different size categories also had different topology. As evidenced by E-cadherin expression in fixed samples, we found that small to large loops contained epithelial cells in their inner hole, (the volume in the middle of the loop, see definition in Table 1). Small loops had just a few epithelial cells in their inner hole, whereas medium and large loops typically have more epithelial cells (*Fig 4Ei-Fii*). In contrast, the inner space of half of the XL loops was devoid of epithelial cells (*Fig 4Gi-ii*). These results were confirmed by quantification of loop structures from fixed *in vivo* and *ex vivo* samples (*Fig 4H*).

Further analysis of the fixed *ex vivo* pancreata showed that the inner hole in M-XL loops contains mesenchymal cells expressing the fibronectin receptor integrin α5 (ITA5), which is also expressed on the basal side of epithelial cells facing the basement membrane (*SFig*

8A-F). The mesenchymal cells do not fill the inner hole in Xl loops, and thus most of the inner hole in XL loops appears empty (*SFig 8A-B)*. We next analyzed extracellular matrix (ECM) proteins, finding that the cell-free part of the inner holes contains ECM. Fibronectin (FN) was deposited as fibrils in close proximity to the basement membrane of epithelial cells, and in the interstitial matrix (*SFig 8D*). FN was seldom observed in small holes (*SFig 8F*), and only in a few medium-large loops (*SFig 8E*), but consistently present in XL loops (*SFig 8D*). Interestingly, some lumenal structures also contained FN deposits (*SFig 8G*). Laminin (LN) was detected in the basement membrane at the periphery of the pancreas, and minimally inside L-XL loops at the boundary between epithelial and mesenchymal cells (*SFig 8H*). Thus, the small loops provide an epithelial niche with little contact to FN, LN or mesenchymal cells. On the other hand, epithelial cells in the larger loops are exposed to mesenchymal cells, fibronectin, and low amounts of laminin. Cells in the loop-sparse environment at the periphery of the pancreas are exposed to mesenchymal cells, fibronectin, and high levels of laminin. These findings shed light on the unique microenvironments provided by different loops within the pancreas resulting in distinct cell-cell and cell-ECM interactions.

Loop closing resolves the ductal network

Previous studies (Bankaitis, Bechard, and Wright 2015; Dahl-Jensen et al. 2018; Kesavan et al. 2009) have reported that the ductal plexus resolves into an arborized structure starting from E14.5 resulting in a purely branched structure without loops by birth, but the mechanism remains unknown. To address the mechanism of how the plexus resolves we analyzed lumen remodeling in time-lapse data from Muc1-mcherry pancreata explanted at E12.5 and grown *ex vivo* for 2 days, followed by up to 48 hours imaging. All loops were manually tracked in 2D maximum projections of filtered data and visually verified in 3D. We tracked 172 loops in 7 different time-lapse datasets. An example of loop tracking and segmentation can be seen in Fig *5Ai-Bii* and movie 19), and a graphical representation of all tracks in *Fig 5E*.

We first analyzed for broader temporal trends, and observed that the rate of new loops forming and the rate of loop removal approximately balance out during the imaging period, with a slight tendency for loop removal to dominate, resulting in a gradual net reduction in the number of loops in the network over time (*Fig 5C*), thus reducing the number of branch points (*SFig 9A*). Although our data is influenced by growth of the explant, which pushes some loops out of the imaged frame of view, this data replicates what has been documented *in vivo* (Dahl-Jensen et al. 2018). Interestingly, while lumenal branch points decreased, end points increased (*SFig 9B-D*), and the ratio of end points relative to total nodes is significantly

larger after 10 hours (*Figure 5D*). This topological change indicates a non-branching type of network remodeling, as classical branching with bifurcation should not increase the relative number of end-points.

We next analyzed our data to find the mechanism of remodeling. To our surprise, we found that loop structures are removed from the lumenal network primarily by a novel mechanism involving gradual constriction of the loop resulting in loop closing and elimination. We coin this mechanism “loop closure”. Examples of loop closure can be seen in *Fig 6A-B* and movie 21 & 22. Loop removal through pruning or breaking of lumens was only very rarely observed (*Fig 6B* and movie 23). Quantification of all time-lapse data confirmed that loop closing was significantly more frequent than lumen breaking (*Fi. 6E*). Of note, the loop closure mechanism is consistent with the observed temporal decrease in branch points.
Out of the 172 tracked loops 123 closed during the imaging, while 49 stayed open (*Fig 5E*). Even though the sizes of the tracked loop structures tended to fluctuate with time in a seemingly stochastic manner, there were clear trends for different size classes. Small (S) loops mostly contract and close fast, especially after reaching 8-12µm, while M-L loops fluctuate in size but tend towards closing. XL loops tend to maintain size or even increase in size (*Fig 5E* with examples in *SFig 9E* and movie 24). XL loops are thus mostly not observed to close in the time span of our imaging. Only 7 (30%) of the loops that start off as XL are observed closing; 3 of these have one or more cinching events on the way to closing (*Fig 6D*). Cinching events naturally produce two loops of smaller size than the original loop and thus both loop closing and cinching events contribute to the overall reduction of loop sizes over time (*Fig 6F*).

Long term, but not short term, loop dynamic behavior can be predicted from static features with some confidence

In order to further characterize the loop closure mechanism, we tested if static loop features relating to size, geometry, and placement in the organ could be used to classify loops as either contracting or expanding, or allow us to predict how much time left a loop had before closing. In other words we wanted to answer the questions "can short term and long term dynamic loop behavior be predicted accurately from static loop properties alone?" We defined two dynamic target parameters: 'Time left in hours before loop closure' (hereafter 'Time left') as a metric for long term dynamic loop behavior and 'current loop normalized contraction/expansion speed' (hereafter 'Contraction/expansion speed') as a metric for short term dynamic loop behavior (*Fig 7A-B*). To investigate if these two targets can be predicted

we extracted static loop features related to size (loop perimeter, inner hole area, loop diameter, length of minor loop axis, length of major loop axis), shape (eccentricity, width of the lumen surrounding the loop) and placement in organ, (the number of lumens branching of a loop, distance to epithelial-mesenchymal interface) from individual time-lapse frames, in movies where the loop dynamic behavior is known (*Fig 7C*). These features were chosen based on assumptions that they could be correlated with the physical forces acting on the loop structure. We then tried to fit regression models in order to predict the two target variables.

We trained feedforward, fully connected neural networks (NN) for regression of 'Time left' and 'contraction/expansion speed' based on the static features, and used a validation dataset for early stopping to avoid overfitting. We also fitted linear regression models, which due to their simplicity does not overfit. For comparison we include two base models, which are constant models that simply always return the median target value of the training dataset, (i.e. the median of time left in training data for one model and the median of contraction/expansion speed in training data for the other model), regardless of the input, and thus serves as our control. We use the base model mean absolute error (MAE) to normalize MAE for the NN and linear models, (*Fig 7D and E*). We see that the NN model's performance (in terms of normalized mean absolute error, here after NMAE) is not far from the linear model for both targets, meaning that the added model complexity of a NN model is not adding much explanatory power (*Fig 7D and E*). Model predictions on the unseen validation data sets have slightly larger errors (NMAE) than on the training set, which is to be expected. Models (both NNM and LM) predicting contraction/expansion speed have similar errors to the base models (their NMAE is close to 1). The models (both NNM and LM) predicting the time left before loop closure on the other hand are doing significantly better than the base model (their NMAE is 0.5-0.6), reflecting that although the instantaneous dynamic behavior of the loops is highly stochastic, there are dynamic trends, which do depend on the static features, and this allow us to predict long term behavior with some confidence.

Loop closing is correlated with loop size, shape and placement in lumenal network and organ

The most important features for predicting time left before loop closure, are the loop size features (*'inner hole diameter', 'convex area', 'perimeter of convex hull', 'minor axis length', 'major axis length', 'lumen loop and hole total area'*), which are highly correlated with both targets (‘Time left’ and ‘Contraction/expansion speed’, see *Fig 7AB*). See Materials and

Methods (Data analysis section) for details on how the six size features were combined into one. The next most important feature for predicting time left was placement in the organ. We found that proximity to the epithelial-mesenchymal interface is associated with faster closure (*Fig 7H*). However for loops in the small (S) size category this is less pronounced than for loops in the medium (M) and large (L) categories; small loops close relatively fast regardless of where they are located. For loops in the XL category the association between organ placement and faster closure is not significant (*SFig 10F*), albeit this could be due to the fact that we have only a few time courses in this size category which reach closure in the time span of the movies (*SFig 10F*). Next feature in line of importance, was placement in the lumenal network. A higher number of branch points (indicating that the loop has more outgoing lumen connections) is associated with longer time left before loop closure (*Fig 7F*). We also find that the shape of a loop is associated with cinching behavior. Elongated loops with high eccentricity (circle has eccentricity = 0, line has eccentricity = 1) are associated with cinching: L and XL loops that experience 1>= cinching events have a higher median eccentricity than non-cinching loops in the same size category (*Fig 7G*). Eccentricity is however not significantly correlated with faster constriction of non-cinching loops (results not shown). Using eccentricity for analysis of fixed tissue, we find that loops (in the L and XL groups) with mesenchyme/ECM/non-epithelial cells types going through them, are on average less elongated. These two observations combined suggest that cinching is less likely to occur, when non epithelial cells types are present in a loop. Mean lumen width (of the lumens participating in the loop structure) did not correlate significantly with dynamic behavior (*SFig 10H*).

Formation of the inner lumenal network does not follow the structure of the outer epithelial branching

In our live imaging analysis of pancreatic lumenal network establishment and remodeling we have focused on imaging apical polarity, and therefore the “inner” architecture of the ducts. In order to compare our results with previous fixed imaging and modeling of epithelial branching, which are mostly based on epithelial outlines of ducts, we next compared the “inner” topology, i.e the lumens demarcated with apical protein, with the “outer” topology, (i.e. the epithelial tissue architecture), (*Fig 8A and C*).

E14.5 fixed *in vivo* specimens (n=7) were used for extraction of inner and outer mid-line map based on segmentations of Muc1 and Ecad staining and differential interference contrast (DIC) images, (see methods). A comparison of these maps showed that the inner tree had on average 3.1 nodes per outer tree node. Of these, the ratio is 3.2 for branch points and 2.5 for

endpoints (*Fig 8B*). Loops with holes inside also exist as loops in the outer tree, while loops with only epithelium inside are not detected as loops in the epithelial outer tree (*Fig8A and C*).

In order to determine the hierarchy of inner and outer tree clefting, we next tracked the changes in inner and outer topology during formation of new ductal peripheral branches. For this purpose we analyzed two live imaging datasets of Muc1-mcherry E14.5 +2 days culture dorsal pancreata, which showed peripheral parts of the explant and included formation of new branches. Muc1-mcherry was used for detection of the inner topology and a combination of autofluorescence and DIC images for detection of the outer epithelial borders (*Fig 8D-E*). We tracked branching events in the outer tree and backtracked the inner tree to the time point immediately preceding an outer three branching event and recorded the number of lumens. We here define clefting as the bifurcation (type Gi/Gii event) of a pre-existing epithelial lobe, and lateral branching (type Giii/Giv event) as the occurrence of a new epithelial lobe on a straight branch (See *Fig 8G* for illustration of event types).

In the first dataset, 9 type Gi/Gii clefting events and no type Giii/Giv events were observed in the outer tree consisting of 5 epithelial main branches. In the second dataset, 8 Gi/Gii clefting events and one lateral branching type Giii/Giv event were observed in the outer tree consisting of 2 epithelial main branches (*Fig 8D-F*). To our surprise, we also detected fusion of epithelial branches in several instances (data not shown), demonstrating that pancreatic epithelial remodeling, at least *in vitro*, is less stereotypic than previously assumed. All type Gi/Gii clefting events were preceded by at least two lumenal tips inside the lobe. We observed only one type Giii/Giv branching event, which was preceded by one lumen protruding at the branching site. For type Gi/Gii clefting events, the number of lumen tips observed inside lobes before clefting was [3 2 2 3 4 3 3 2 2 2 3 3 4 3 2 3 2], mean-+std = 2.7059+- 0.686, median = 3, min = 2, max = 4. This data suggests that branching is always preceded by the formation of an inner lumen. However, we also often observe the presence of multiple lumen tips in one lobe without a subsequent lobe splitting event, so having a preceding lumen appears to be necessary, but not sufficient to trigger a branching event.

In conclusion, the lumenal inner tree is more complex than the outer epithelium tree. Branching events in the outer epithelial structure were always preceded by the formation of an inner lumen, suggesting that lumenal remodeling drives epithelial branching.

Discussion

The formation and growth of tubular structures in branched organs have been studied extensively. However, in order to uncover the main mechanisms driving tubulogenesis, findings from multiple studies have often been connected and extrapolated. For instance, fixed data has been used to describe dynamic processes and live imaging of simplistic cellular models have been used as a proxy for more complex tissue. Whilst these data are valuable, their extrapolation can oversimplify or mislead how we view tissue and cell behavior in complex organs. Our study records lumenogenesis live across multiple overlapping stages of *ex vivo* pancreatic development and provides stage-matched *in vivo* data. As a result we have identified a number of novel lumenal mechanisms that drive the transformation of the pancreatic ductal system from a simple tube to an interconnected arborized network.

The generation of our new reporter mouse for the live imaging of apical polarity was imperative for visualizing the novel mechanisms in lumen transformation. The Muc1-mcherry reporter faithfully recapitulates endogenous Muc1 expression and localization in multiple epithelial organs making it a valuable tool for exploring apical polarity in many research fields. As opposed to the Cre-inducible Crb3-EGFP apical reporter (Pan et al. 2015), we found no evidence of gain of function phenotype in Muc1-mcherry heterozygous carriers. This is likely due to the use of the normal Muc1 promoter and regulatory regions in the BAC construct. Importantly we show that the Muc1-mcherry reporter is compatible with other live imaging reporters. In order to capture the fluorescent reporter's expression in real time we utilized an established *ex vivo* pancreas explant culture protocol. The explant's growth, though slightly compressed in depth, supports cell differentiation and morphogenesis that is relative to an *in vivo* dorsal bud (Löf-Öhlin et al. 2017; Puri and Hebrok 2007). In this study we further validated the pancreas explant culture model by verifying key live imaging findings in stage matched whole *in vivo* pancreata.

To our knowledge our study is the first to analyze the early stages of CPL formation and transformation using lumenal markers in high resolution 3D and 4D detail. By combining the ZO1-GFP and Muc1-mcherry reporter to mark immature and mature apical domains respectively, we confirm in real time that ZO1 is first localized apically, and later becomes restricted to tight junctions. This interesting expression pattern was first described in static *in vivo* sections of the pancreas by Villasenor *et al (Villasenor et al. 2010)*. In contrast to ZO1-GFP, which is expressed in all stages of early lumen formation, we find that Mucin1

apical expression is a relatively late event in the cascade of apical polarity establishment - often first detected in the distal CPL cap of evaginated dorsal pancreatic buds. Thus we conclude that Mucin1 is a more mature apical polarity marker in the developing pancreatic bud. We confirm that the CPL forms through a process of budding, during which the CPL stalk remains continuous with and extends perpendicularly from the foregut lumen. Thus we conclude that the CPL stems from an already polarized site. The process of budding is thought to contribute to the formation of other foregut endoderm primordia such as lung (Metzger et al. 2008) and thyroid (Pierreux 2021). However, while other budding primordia e.g. the lung buds, retain a patent lumen, we find that the lumen at the center of the early pancreatic bud does not. We speculate that a lack of classical polarity hallmarks, such as tight junction localized ZO1 and non patent lumens, could permit a more dynamic cellular behavior to enable the lumenal transformations we observe during network formation.

Current models of pancreas duct formation depict the immature pancreas network arising *de novo* from fusion of secondary lumenal sites (Hick et al. 2009; Villasenor et al. 2010; Kesavan et al. 2009). These microlumens are purported to coalesce and unify into a lumenal plexus. However, only one other study (Azizoglu et al. 2017) to date has provided live data documenting apical foci contribution to the lumenal plexus. This study included imaging of network remodeling and expansion at E11.5+1 day and found that foci only contributed to network growth at the tips/periphery of the network at this time. In contrast we observed foci contribute to growth across the network during early establishment.

In agreement with previous studies, our live imaging data detected several isolated lumenal foci distant to the CPL, which would appear “de novo” if visualized statically. However, by back-tracking these foci, we demonstrate for the first time that the vast majority of the foci which contribute to the network stem from the original CPL lumen, and thus do not form “de novo”. We document and quantify six dynamic mechanisms of lumen transformation, of which de novo lumen formation contributed least (3.2%) to network growth and change. We conclude that whilst secondary network growth is complex, it is largely driven by the reshaping of already established lumenal structures. The founding transformative structure is the CPL itself which, as Hick et al observed in their static study, first forms naive secondary lumenal branches (Hick et al. 2009). In contrast to previous studies (Shih et al. 2016; Hick et al. 2009), we find that lumenal branch extension from the CPL and the formation of peripheral foci are not independent processes. We observe apical foci that both stem from and then later re-contribute to forming lumenal branches. Moreover continuous lumens can

fragment, become disparate and then reunify. To our knowledge, this is the first study to report a tubulogenesis process which combines budding, dynamic remodeling and foci contribution. Follow up studies utilizing cell membrane reporters will be necessary to understand the cellular behaviors that contribute to each category of lumen transformation. We speculate that cell proliferation drives network growth, but how this could contribute to the temporary breaking apart of lumenal sites remains to be defined.

Multipotent pancreatic progenitors (MPPs) that form the pancreatic buds are uniquely specified within the foregut to express a pancreas transcriptional profile (Jørgensen et al. 2007). We and others in the field (Azizoglu et al. 2017; Shih et al. 2016) have now shown that MPPs also have unique cellular behaviors and properties. The primitive bud provides a MPP niche within which complex inner lumenal networks and outer epithelial tubes are initiated. These structures form an intermediate network stage (the plexus) within which endocrine cells are specified. Eventually the plexus is remodeled into a branched architecture within which cells acquire their mature exocrine or endocrine function. We show that the lumenal loops found in the plexus provide unique niches, which differ in their dynamic behavior and ECM composition depending on their size. This observation is especially interesting given earlier studies showing that endocrine progenitors are preferentially specified in and depend on this environment (Bankaitis, Bechard, and Wright 2015; Mamidi et al. 2018) as evidenced by genetic perturbation of plexus formation which decreases endocrine differentiation (Kesavan et al. 2009; Barlow et al. 2023), while prolongation of the plexus stage enhances endocrine cell numbers (Azizoglu et al. 2017). We speculate that endocrine differentiation could be driven by loop remodeling driven exposure to unique ECM profiles, and aim to address this hypothesis using live imaging reporters of endocrine differentiation in future studies. Additionally, the ECM could be a driver behind loop closing, as ECM driven changes affects individual cell behavior such as cell migration, cell reorientation and polarity establishment (Wang et al. 2017; Walma and Yamada 2020; Chen et al. 2019), transcending the individual cell level and actively modulating morphogenesis at the tissue level (Isabella and Horne-Badovinac 2016).

Our analysis of later stages of pancreas development led to the discovery of a novel mechanism for ductal remodeling which we term “loop closure”. We show that the ductal network is remodeled into an arborized structure by gradual closing of ductal loops, rather than via pruning, which has previously been suggested (Flasse, Schewin, and Grapin-Botton 2020). One study has suggested that the network is remodeled based on liquid flux in the

lumen (Dahl-Jensen et al. 2018). We do not find any evidence in our live imaging data to support this hypothesis as we do not observe any correlation between lumen width and loop closure. We instead hypothesize that loop closure depends on physical forces acting on the loop epithelial cells' cytoskeleton depending on the size, geometry and topology of the loop. This hypothesis is based on our attempts to predict dynamic behavior based on static features, which showed that although the instantaneous dynamic behavior is highly stochastic, there are dynamic trends which depend on features such as number of lumenal connections, size of loop, and placement in organ, which allow us to predict long term closing behavior with some confidence. Specifically the fact that we observe that a higher number of lumenal connections is associated with slower loop closure we hypothesize is due to forces transmitted through the lumenal network hindering loop closure and/or causing loop widening. Such forces we pose are caused by growth and spreading of the organ. Findings from analysis of perturbed actomyosin contractility support this hypothesis, as the plexus fails to remodel in a RhoA/Afadin double KO model (Azizoglu et al. 2017). However, this hypothesis needs to be explored further in an *in vivo* setting, to determine if the forces are different *in vitro*.

Branching morphogenesis studies of the pancreas tend to focus either on epithelial branching morphogenesis or internal lumen remodeling. We aimed to reconcile these studies by tracking lumen and epithelium in parallel. Early live imaging studies using the Pdx1-GFP reporter concluded that the predominant mode of early stage pancreas growth is lateral branching (85%), with some bifurcation (15%) (Puri and Hebrok 2007). We tracked epithelial branching at a slightly later stage and predominantly found bifurcations, which is in agreement with the finding of clefted morphology of tip-ends at this stage. Discrepancy between our study and Puri and Hebrok could also be due to the scoring method, as we counted bifurcation of all branches, while the former study appears to only count bifurcation of the tip of the primary branch.

At the cellular level, epithelial branching has been explained by localized proliferation, coordinated cell shape changes, and/or cell rearrangements, as summarized in (Varner and Nelson 2014). Proliferation happens preferentially at the tip during branching (Sznurkowska et al. 2018; Zhou et al. 2007; Larsen et al. 2017), but a direct coupling between proliferation and branching has not been reported in the pancreas. Studies manipulating cytoskeletal components (Azizoglu et al. 2017; Shih et al. 2016) and cadherins (Shih et al. 2016; Nyeng et al. 2019; Marty-Santos and Cleaver 2016) suggest that cell shape changes and cell

rearrangements could be a driver behind pancreatic branching morphogenesis, but no clear inductive mechanisms for a new branch-site have been demonstrated. Our finding that a new epithelial branch is always preceded by a lumen, suggests that apical polarity could be an inductive signal for branching. Although our data also indicates that lumen formation is not sufficient for branching, suggesting that additional input, perhaps from the ECM, is required.

Several models/simulations of branching morphogenesis have been proposed (Hannezo et al. 2017; Dahl-Jensen et al. 2018; Metzger et al. 2008; Sznurkowska et al. 2018). They tend to be developed with the principle of parsimony in mind. While it is fascinating that a few simple rules can govern the generation of some developmental patterns, we would argue that live imaging data such as ours demonstrate that the formation of complex patterns during organogenesis often requires more complex models. As a case in point, comparative studies of pancreas and other branched organs led to the proposal of a unified model of branching morphogenesis based on tip splitting, tip elongation, and tip growth termination (Sznurkowska et al. 2018; Hannezo et al. 2017). Although this model may explain branching at the periphery of the pancreas, it fails to incorporate plexus remodeling, and is incompatible with the existence of loop closure, branch fusion, and loops with non-epithelial cell-types or ECM in the center, as described in this study. It would be interesting to test whether models incorporating the features reported in our study better replicate pancreatic morphogenesis.

In summary, our novel findings highlight the importance of utilizing live imaging to define dynamic processes such as lumenogenesis. Similar live imaging studies in other organs are beginning to uncover the underlying mechanisms in branching morphogenesis, which appears to be an umbrella term, covering diverse mechanisms in various organs (Varner and Nelson 2014). Whether the specific dynamic events we report in the pancreas, such as lumenal dynamics and loop closing, can be found in other branched organs deserves more detailed studies in the future.

Materials and Methods

Key reagents and equipment can be found in the supplementary tables.

Generating Muc1-mcherry reporter line:

The Muc1-mcherry fusion protein construct was created by BAC recombineering using galK selection (Warming et al. 2005) (Fig 1A). The 171kb BAC RP24-365K20 (Oakland Research Institute BACPAC resources) was targeted in frame at the intracellular C-terminal of the *mucin1* gene (after exon 7). After verification of the BAC by PCR for Muc1 exon1 and 7, it was transformed into DH10B derived SW102 bacterial cells (National Cancer Institute biological Resources Branch). These bacteria contain a fully functional gal operon, except the galK gene is missing. The first targeting step introduced a galK construct flanked by 50bp homology arms. After selection on minimal medium with galactose, a second targeting step replaced the galK cassette with an amplified pmCherry-N1 plasmid (kind gift Roger Tsien) PCR fragment flanked by the same homology arms used in the first selection step and with or without a Gly-Gly-Ser linker. This is achieved by negative selection on minimal medium containing 2-deoxy-galactase (DOG) with glycerol as the sole carbon source. Amplification primer sequences with homology arms are included in STable5. 6 out of 50 recombinant clones were verified with PCR of insertion sites and sequenced. 5 of these were correct. The targeted BAC (with and without linker) was purified (using the BAC100 kit from Nucleobond), but not linearized before oocyte injection at 1 ng/µl in NFR x C57bl/6 (Lund University transgenic core) or C57Bl/6N (University of Copenhagen core facility for transgenic mice) oocytes. Purified BACS were verified by SpeI digest.

Three rounds of oocyte injection with the entire purified targeted BAC (Two at Lund University transgenic core and one at University of Copenhagen core facility for transgenic mice) gave rise to two founders in Lund and three in Copenhagen. Only the BAC with targeted construct without the linker sequence gave rise to positive offspring.

One female founder was infertile. The four remaining founders were named Muc1-mcherry 0M, 5M, 12M (male founders) and 2F (female founder). The mouse lineages were maintained on a C57BL/6BomTac genetic background.

Animal studies

All mice were housed at the Department for Experimental Medicine at Copenhagen University and their use in experiments approved by “Miljø- og fødevarelseministeriet – Dyrforsøgstilsynet”. Heterozygous Muc1-mcherry reporter mice of breeding age were plugged with C57BL6 mice or ZO1_GFP mice (Foote, Sumigray, and Lechler 2013) (or vice

versa) to generate embryos for static and live analyses. Plugging males (12 weeks-2 years of age) were single housed, while females (8 weeks-20 weeks of age) were group housed. For timed mating, 1-2 females were added to the male cage in the afternoon and a vaginal plug was checked every morning for up to 3 days. Littermates were used as controls in all experiments. Embryonic day 0.5 (E0.5) was designated as noon on the day a vaginal plug was detected. Somite pair numbers were used to accurately stage embryos between the ages of E9.0-11.0. After this stage, anatomical features such as limb and craniofacial morphology were used to verify the embryos developmental stage. At least three embryos were analyzed per experiment.

In vivo studies

Male and female embryos at gestational age E8.5-E18.5 were used for experiments as indicated in the results section and below. Organs were dissected from embryos at noon on the indicated day and immediately fixed in 4% paraformaldehyde (PFA) for 30 minutes to 16 hours depending on size of the tissue and either transferred through an ascending gradient to 100% methanol for storage at -20°C or used immediately for immunostaining . For a more detailed description of embryonic mouse pancreas dissection and processing see (Heilmann, Semb, and Nyeng 2021).

Genotyping

Tissue from one limb bud (older embryos), yolk sacs (young embryos) or ear biopsies (3 week old pups) was used for PCR based genotyping using the REDExtract-N-Amp kit (Sigma-Aldrich) with the primers listed in STable5. PCR for Muc1-mcherry was performed using the following program, and analyzed by gel-electrophoresis:

1) 94°C x 3 minutes, 2) 94°C x 45 seconds, 3) 61°C x 1 minutes, 4) 72°C x 1.30 minutes, 5) GO TO STEP 2 AND REPEAT 34 X, 6) 72°C x 8 minutes

PCR for ZO1_GFP was performed using the following program, and analyzed by gel-electrophoresis:

1) 94°C x 3 minutes, 2) 94°C x 30 seconds, 3) 61°C x 1 minutes, 4) 72°C x 1 minute, 5) GO TO STEP 2 AND REPEAT 34 X, 6) 72°C x 2 minutes

Fasting blood glucose and weight

Muc1-mcherry 0M, 5M, 12M and 2F heterozygous males were crossed to C57bl/6 females and the offspring was genotyped. Muc1-mcherry heterozygous and negative pups were kept

until 8 weeks of age, when they were fasted overnight. The next morning, the mice were weighed and a blood drop was collected from the tip of the tail and directly measured for blood glucose using a glucose meter. 2-4 litters were analyzed per sub-strain.

Analysis of mCherry expression in unfixed tissue

Pancreas, colon, duodenum and lung were dissected from adult female Muc1-mcherry mice (age 21-37 days). A small fresh biopsy from each tissue was placed on a microscopy slide, squashed between slide and a coverglass, and immediately imaged using a Zeiss axioplan2 widefield fluorescence microscope.

Ex vivo studies

35mm dishes or 8-well µ-Slides with #1.5 coverglass bottoms were used for culturing and imaging *ex vivo* whole embryonic pancreata and lung. Silicon inserts (Ibidi) were applied to 35mm dishes to ensure explants could be identified for genotyping after imaging and for increasing the explant attachment rate. All culture vessels were pre-coated for 45 minutes at RT^{o}C with 100 µg/ul of Fibronectin (Invitrogen) to allow explant attachment, after which explant media (Media 199 with phenol red supplemented with 10%FBS, 50 U/mL of penicillin and Streptomycin and 0,25 µg/ml of Fungizone) was added to culture vessels. Explants were cultured at 37°C at 5% CO_2 for 6 to 48 hours before imaging (see below for experiment-specific pre-imaging and imaging culture times). Shortly before imaging, the explant medium was replaced with imaging media (Media 199 without phenol red supplemented with 10%FBS, 50 U/mL of penicillin and Streptomycin and 0,25 µg/ml of Fungizone).

Pre-midgestation embryos (E9.0-E11.0)

Embryos were collected from their mothers dam and the posterior half of their gut tubes or lung buds were isolated by fine dissection under a stereoscope in sterile PBS. The lung buds were directly transferred to a coated culture vessel for evaluation of Muc1-mcherry expression by live imaging.

To determine which mechanism is responsible for establishing the pancreatic CPL we established a protocol for live imaging of whole E9.75 to E10.0 posterior foregut explants. This method includes dissecting out and explanting the dorsal and ventral pancreatic buds, the biliary bud, foregut and some of the prospective stomach. Keeping so much of the posterior foregut intact aids identification of the early anlage, increases explant survival and

attachment and maintains tissue physiology. To minimize the thickness of tissue to be visualized and to aid explant attachment, the epithelium and a thin layer of mesenchyme was removed from the ventral side of the gut tube.

Midgestation embryos (E11.5-E12.5)

E12.5 Embryos were collected from their mothers and the dorsal pancreas was isolated by fine dissection under a stereoscope in sterile PBS and explanted onto fibronectin coated culture vessels. The medium was changed to fresh explant media the following day. Explants were cultured for a total of 48 hs before live imaging or fixation. For the ECM expression studies, dorsal pancreas was explanted from E11.5 embryos and cultured for 3 days before fixation and immunostaining.

Immunofluorescent staining of cryo-sectioned tissue

Embryonic tissues were processed for cryo-sectioning after fixation in 4% PFA and washing in PBS. Samples were incubated overnight in 30% sucrose diluted in 1x PBS, equilibrated through 30% sucrose:OCT 1:1 for one hour into 100% OCT for one hour and finally transferred into cryo-molds filled with fresh OCT for freezing on blocks of dry ice. Cryo-sectioning at 6µm was performed using a Leica cryostat.

For immunofluorescent staining, tissue was first cleared of OCT and permeabilized by washing three times for 5 minutes in PBST (1x PBS with 0.5% or 0,01% Triton-X) and then incubated in a blocking solution of 5% neonatal donkey serum (NDS) in PBST for a minimum of 1 hour. Primary antibodies were diluted in a blocking solution and applied to the sections and incubated at 4°C overnight (16 hs) in a humidified chamber. For a list of antibodies and dilutions see STable 2.

Subsequently, the primary antibodies were removed and the slides washed in PBST three times before application of diluted fluorophore-conjugated secondary antibodies, (STable 3), in a humidified chamber for a minimum of 1 hour. The secondary antibody solution was removed and the slides washed in PBST. After a final wash in PBS, slides were mounted in DAKO mounting solution with or without Hoechst 33342 (Invitrogen, H3570/23363w, 1:1000) using #1.5 cover glasses.

Whole mount immunofluorescence staining

Embryos were collected from their mothers dam and the posterior half of their gut tubes (pre-midgestation embryos) or the stomach, pancreas and duodenum (late gestation

embryos) were isolated by fine dissection in sterile PBS. 4% PFA was used for fixation of all samples; pre-midgestation gut tubes were fixed 30 mins -1 hour at RT, post-midgestation embryos, gut tubes and organs were fixed overnight at 4°C. After fixation, samples were washed in PBS and dehydrated through methanol:PBST gradations into 100% MeOH. mid-late gestation samples were bleached in a 1:1:4 dilution of 30%H2O2: DMSO:MeOH (Dent's Bleach) for up to 2 hours at RT. Samples were then rehydrated through methanol:PBT2 gradations into PBT2 and blocked in 5%NDS;0.5%PBST or blocking buffer for 2 hours at RT. Primary antibody was then applied (see STable 2) and samples left to incubate, shaking, for 16-24 hours at 4°C. The following day primary antibody and samples were washed in 0.5%PBST once an hour for 5–8 hours at RT to remove any unbound antibody from the tissue. Subsequently, secondary antibody in 0.1%PBST was applied to samples and incubated overnight at 4°C (see STable 3). The following day, unbound secondary antibody was removed by washing samples in 0.1%PBST once an hour for 5–8 hours at RT. To prepare for clearing, the tissues were dehydrated in methanol: 0.1%PBST gradations to 100% MeOH. Finally, samples were transferred to a clearing solution i.e. BABB (1:2 benzyl alcohol and benzyl benzoate) for late gestation samples, Methylsalicylate for pre-midgestation gut tubes and explants.

For immunohistochemistry of *ex vivo* cultured explants, medium was removed and explants fixed in the culture vessel for 30 mins in 4% PFA at RT. After fixation, explants were washed in PBST and incubated with blocking buffer overnight at 4°C. Explants were then incubated with primary antibodies (see STable 2) in blocking buffer over 3 nights at 4°C for optimal antibody penetration. Subsequently, explants were washed with PBST for 5-6 hrs, followed by secondary antibody (see STable 3) incubation overnight at 4°C. Explants were directly imaged in PBS after washing. No clearing agent was used as it degrades the plastic surrounding the glass bottom surface.

Imaging acquisition

A subset of images in figure 1 was recorded on a Zeiss axioplan2 widefield fluorescence microscope. All other image acquisition was conducted with inverted laser scanning confocal microscopes. A Leica SP8 system with 20x and 63x glycerol immersion objectives was used for a subset of fixed imaging. Zeiss LSM780 or LSM880 systems with 40x water immersion objectives were used for live imaging, and 40x and 63x oil immersion objectives for fixed imaging. See specifications of systems and objectives in STable 7

Live imaging

STable 1 contains individual imaging settings for each live imaging experiment.
Before imaging, explant media was removed from the sample dish and pre-heated imaging media added. The on-stage incubation chambers were pre-heated to 37°C with 5% CO2 supply for a minimum of 2 hours prior to image acquisition. Image acquisition was performed using Zeiss LSM780 or LSM880 Airyscan (in regular scanning confocal mode) confocal systems. Multi-position images were acquired at an interval of either every 4, 8, 10 or 12 minutes (as indicated in figure legends and STable 1). Pixel resolution was as standard at 512 X 512 for pre-midgestation embryos and 1024 x 1024 for post-midgestation embryos unless stated otherwise. Laser lines were kept to a minimum in all imaging sessions to reduce phototoxicity and DIC light was collected with the PMT detector. The imaging session was carried out for a minimum of 20 hours and a maximum of 72 hours for one dish of samples. For a subset of imaging sessions the explants were fixed and stained post-imaging by immunohistochemistry to assess epithelial integrity, lumenal network morphology and, where relevant, cell differentiation. Assessments were made within the same dish for explants that had been exposed to the confocal laser and those that had not (i.e were not imaged). For experiments where enough embryonic material was available a non-imaged control set of explants were also kept in the incubator and used as a second control for any effect of the microscope on-stage incubator.

Image processing, rendering and analysis

Image processing, rendering and analysis was performed using Imaris, Fiji/ImageJ or Matlab. All confocal images are shown as either 2D single Z-slices or 3D maximum intensity projections (MIP). Image intensity and contrast has been adjusted across the entire image/stack to aid in visualization. Any further processing is mentioned in the legends or below for each experiment.

Processing and rendering of live imaging movies of pre-midgestation (E9.5-E10.5) pancreata

For analysis of lumenal network morphogenesis the following pre-processing steps were applied in Imaris:

1) Files were split into single positions
2) A median (3x3x3) smoothing filter was applied to ZO1-GFP and Mucin-mCherry channels.

3) Where necessary to improve visualization Z-slices at either end were deleted from the image stack to remove non-epithelial signal (e.g. ZO1-GFP in endothelial cells, see S Figure 5 and main text for explanation of how to identify this signal) or to reduce noise. Raw data files are provided for comparison. No data was removed during quantifications.
4) Because of the unstereotypical/heterogeneous expression of lumen and foci marked by the live imaging reporters, Imaris could not faithfully segment all lumenal structures automatically. Hence all tracking was undertaken manually. For lumenal network tracking the Imaris spot function was used as a rendering method (see below).

Pre-midgestation lumenal network tracking and quantification in Imaris:

1) After rendering (see above) movies were cropped in time to a point where most lumenal branches could be tracked backward in time i.e. out of frame data was deleted.
2) Each unique lumenal branch during the imaging interval was defined in a new folder. The Imaris spot function was used in each 4 minute time frame to mark - independently - whether a branch was contributed to by: i) extension of an existing lumen, ii) a temporary or iii) permanent break point, or, iv) a derived or v) de novo foci. We also observed lumenal merging events but did not track these. Events were tracked back and forth in time to ensure the tracking was accurate.
3) To simplify the tracking we only tracked events that contributed to permanent proximal-distal growth of a lumen. In other words, foci or breaking events that may contribute to media-lateral growth of the lumen, or to temporary structures such as lumenal spikes, were not quantified. This means that the number of total events were underrepresented in this dataset.
4) When a foci was tracked, a measurement was also taken of the distance of this foci to surrounding lumenal structures. We presume that foci less than the average epithelial cell length away (<10 µm) are foci derived from already polarised MPPs and those more than a cell length away (>10 µm) could be generated 'de novo' from unpolarised MPPs.
5) At the end of the Imaris tracking we exported the tracking count data in excel table and inputted the data into Prism for analysis and visualization as scatter graphs.

Processing and rendering of fixed in vivo pre-mid-gestation (E9.5-E10.5) pancreata:

All fixed data was processed by applying the median (3x3x3) smoothing filter in Imaris, any channels lacking signal were also deleted. In some samples there was a strong autofluorescence, derived from red blood cells covering the pancreatic bud, or from debris in mesenchyme. In these cases to be able to view the lumenal signal in the 3D MIP we segmented the ECCD2 or PDX1 channel. Once we had a faithful pancreatic epithelium segmentation, we could view the lumenal channel within the segmentation as a unique 'masked lumenal channel'. For an example see SFig4Gi.

Processing, rendering and analysis of live imaging movies of late gestation (E14.5-E16.5) pancreata:

Movie preprocessing:

Noise filtering: First we performed 3D gauss filtering (sigma=0.5) then 3D median filtering (3x3x3 neighborhood) of original Muc1 channel images, ORG_IM, producing IM.

Filtering out small bright artifact vesicles removed from lumenal network: The Muc1-mCherry channel contains small and very bright spots that are most likely Muc1-mCherry concentrated in intracellular vesicles. We removed these, by constructing a REMOVE_MASK, as they interfere with the analysis of ducts.

1) We determine the 99 intensity percentile threshold, T_99, using as input 10 consecutive timepoints at a time. We use T_99 to threshold IM and obtain a mask (MASK1) containing only the very brightest objects (bright vesicles inside epithelial cells and lumenal tips). We then produce a second mask, MASK2 by taking the 97 percentile threshold (T_97) of IM. From MASK2 we keep only connected components larger than 3000 voxels, by using MASK2=bwareaopen(MASK2,3000). Our REMOVE_MASK is then all connected components (cc's) in MASK1 that do not have an overlap with connected components in MASK2.
2) We then produce a third mask, MASK3 by taking the 95 percentile threshold (T_95) of IM. We produce MASK4 by keeping only cc's larger than 3000 voxels from MASK3 and dilating the remaining component with a spherical structuring element of radius 1 pixel. REMOVE_MASK is then set to include objects in MASK3 which do not have an overlap with objects in MASK4.
3) We dilate the REMOVE_MASK with a spherical structuring element of radius 1 pixel. Intensity values or IM inside REMOVE_MASK are replaced with those of voxels from 3D medfilt(ORG_IM) (15x15x3 neighborhood), producing the 'cleaned/filtered' IM_CLEAN result. See examples of raw image and filtered image in SFig11

Loop tracking: Maximum intensity projections (MIPs) of the prepossessed/cleaned IM_CLEAN (see steps above) Muc1 channel movies were produced. Using a custom designed GUI we tracked/detected all loop structures and detected lumen breaking events in 2D. The human annotator determined beginning and end times for a given loop event and clicked on the approximate x,y coordinates of the loop center at every 5 time points, (the loop position in the 4 unannotated timepoints between two annotated timepoints were then determined by linear interpolation). All such manually detected loop events were then extracted from the data as 4D (3D plus time) cropped movies and inspected visually in Imaris to confirm that they were indeed bonafide loop structures when examined in 3D, and not just lumen structures crossing each other in different image planes. The dark area (without Muc1 signal) inside each loop was then segmented in MIP 2D movies in a semi automated fashion with final hand corrections done by a human in itk-snap, when need be. The rest of the lumenal network (i.e. areas outside the cropped/extracted loop movies) was segmented in a fully automated manner.

Processing, rendering and analysis of fixed *in vivo* pancreas and fixed *ex vivo* pancreas from mid gestation (E14.5)

Image preprocessing:

Intensity rescaling: Original 2 color images (Ecad and Muc1) were stored as 16 bit but in reality less than 14 bit was used (Zeiss czi files have a true bit depth of 14). The images all had their intensities rescaled to fit 8 bit by recasting to double type, normalizing/dividing with 99.9 percentile intensity value of the respective channel multiplying with 255 and recasting to uint8.

Spatial rescaling: All 3D images where rescaled spatially to become isotropic with xyz resolution [1 micron x 1 micron x 1 micron] per pixel, interpolation to new grid was bicubic, (the output pixel value is a weighted average of pixels in the nearest 4-by-4 neighborhood). We used the MATLAB imresize() function.

Semantic segmentation:

Random forest prediction: A random forest (RF) model was trained using ilastik (https://www.ilastik.org/), based on sparse annotations performed by hand on select images in itk-snap. In ilastik, all possible image features were selected at all possible spatial scales. Using the trained ilastik RF model, pixels/voxels of all images were segmented into four

classes: 1) lumen, 2) epithelial cell 3) mesenchymal cell and 4) medium/glass/nothing, with simple segmentation output.

Post prediction processing:

Morphological operations performed on RF output:

Step by step operations performed on pixel class 1 / Lumen:

- Close of small 'holes' in *Lumen* by performing morphological closing with a spherical structure element with radius=1. MATLAB function imclose(*Lumen*,strel('sphere',radius)).
- Fill holes in *Lumen*. MATLAB function imfill(Lumen,'holes'). Based on 6-connectivity.
- Remove isolated pixels, (isolated based on 26-connectivity), with MATLAB function bwmorph3(Lumen,'clean').
- Fill all holes in *Lumen* again.
    - Make a mask, *LumenConnMask*, which includes the entire lumenal network by performing morphological closing with a cubic structure element with radius=20. MATLAB function imclose(im,strel('cube',radius)).
    - From *LumenConnMask*, keep only connected objects larger than 1e4 pixels.
- Remove pixels in *Lumen* that are outside *LumenConnMask.* This gets rid of small objects further away than 20 pixels from the main lumenal network

Label different connected components in *Lumen* (connectivity 26) with different indices and inspect visually in itk-snap. Join up disparate elements if needed by hand (sometimes classification fails for very small/thin lumens which can cause the lumenal network to break).

Step by step operations performed on pixel class 2 + Lumen (from above):

- Join pixel class 2 with *Lumen* as *Epi* (epithelium mask). (MATLAB: Epi = P==2 | Lumen);.
- Fill holes in *Epi*.
- Remove isolated pixels.
- Keep a pixel set to 1 if 14 or more voxels (the majority) in its 26-connected neighborhood are 1; otherwise, set the pixel to 0. with MATLAB function bwmorph3(Epi,'majority').
    - Make a mask, *EpiConnMask*, which includes the entire epithelium by performing morphological closing with a cubic structure element with radius=15.
    - From *EpiConnMask*, keep only connected objects larger than 2e6 pixels.
- Remove pixels in *Epi* that are outside *EpiConnMask.* This gets rid of small objects further away than 15 pixels from the main epithelium.

Step by step operations performed on pixel class 3 / Mesenchyme:

- Small 'holes' in class 3/mesenchyme (*Mesen*) were closed by performing morphological closing with a spherical structure element with radius=4.

Lumen overrules Epi which overrules Mesen in terms of pixel identity.

Network feature extraction:

lumenal/epithelial graph extraction and loop count/detection: From Lumen and Epi we made a 1 pixel width skeleton representation (LumenSkel and EpiSkel) of the lumenal network using the MATLAB bwskel() function. E.g. bwskel(Lumen,'MinBranchLength',15) (which uses the medial axis transform). We then made the skeleton images into a MATLAB graph object where each pixel=1 in the skeleton image was considered a node and edges were introduced between nodes closer than $\sqrt{3}$ pixels apart, (the distance of the internal diagonal of a 1x1x1 cube). Forming a graph in this way has the unfortunate side effect of forming some small 'false' loops/cycles (with 3-6 nodes) near branch points. Using a custom written function we removed select edges in order to remove/break such loops of size less than 15 nodes. Using the MATLAB function cyclebasis() we found all loops/cycles in the graph. The cyclebasis() function returns a cycle basis (a set of cycles with which one can construct all possible cycle paths in the graph) for the graph but not necessarily the basis with minimal overlap between node sets of each cycle. Using a custom written function we rearranged cycles to get the basis with the least amount of overlap possible between node sets in each cycle.

Locating endpoints, branch points and mid-length points in skeleton images: Using the MATLAB function bwmorph3(skelIM,'endpoints') and bwmorph3(skelIM,'branchpoints') we located endpoints and branch points in the lumenal network. We found the points on the skeleton at mid length between branch points in two steps: First we determined the distance transform (along the skeleton) to the nearest branch point with D=bwdistgeodesic(skelIM,branchPointIM). We then found the 'mid length points' by locating the regional maxima in D with imregionalmin(D).

Determining lumen and epithelial width: We used the MATLAB distance transform function (bwdist()) to make Dlum=bwdist(imcomplement(Lumen)) and Depi=bwdist(imcomplement(Epi)), the approximate short axis x 1/2 of the lumen/epithelium (in microns) could then be found by extracting the pixel value of distance image D along the skeleton image pixels.

Processing and rendering of images from fixed *in vivo* late gestation (E14.5) pancreata from Muc1-mcherry embryos

For analysis of any phenotype of the Muc1-mcherry reporter mouse, dorsal pancreas whole mounts from reporter positive and negative littermates, stained for Muc1, Insulin and

E-cadherin and imaged in 3D using the Sp8 confocal were analyzed using Imaris. Segmentation of all channels was done using Imaris Surfaces wizard with identical settings for all embryos. Volume (μm^3) E-cadherin, Insulin and Muc1 was exported to Excel, where volumes of Insulin and Muc1 were normalized by dividing with E-cadherin volume.

Data analysis

Statistical analysis

All statistical tests were based on at least n=3, as indicated in figure legends. Before statistical testing, data was checked for normality and equal variance. Statistical analysis was performed in GraphPad Prism or Matlab.

In Graphpad Prism, data following a Gaussian distribution was analyzed by unpaired t test when F test for equal variance showed no statistical difference (p>0,05) and otherwise with unpaired t test with Welch's correction.

For the count data pertaining to the tracking of early lumenal events contributing to secondary network formation, we performed a Chi-Squared test in Prism to check that the observed counts were not likely to have occurred by chance.

In MATLAB normality was checked via the Anderson-Darling test using the function adtest(), equal variance was checked using vartest2(). The 2 sample t-test was performed using the function ttest2(). For distributions that did not pass the normality test, we used the Wilcoxon rank sum test (using the function ranksum()) to test for unequal medians. Rank correlation (Spearmans' Rho) between variables X and Y was determined using the function corr(X,Y,'type','Spearman').

Models

Design of the 'combined size feature'

We engineered a new combined size feature that is simply a linear combination of different features quantifying loop size. This was done for several reasons: 1) to reduce dimensionality of the feature space in a way where we retain information relevant to the prediction of the two target/response variables, 2) to tackle the problem of collinearity between these features and 3) to arrive at a combined size feature which is more robust to measurement error/noise in the individual features. This new combined size feature was used when dividing the loop data into our size categories S,M,L and XL, see S Fig10A. The original size features contributing to the combined feature were:

1. *'inner hole diameter',*
2. *'convex area',*
3. *'perimeter of convex hull',*
4. *'minor axis length',*
5. *'major axis length'*
6. *'lumen loop and hole total area'*.

(These were log transformed if needed and z scored). These original size features where weighted in the new combined size feature according to their correlation with the two target variables 'Time Left' (hereafter 'TL' - time left before loop closes) and 'loop contraction rate' (hereafter 'dP/dt' - signed contraction speed of loop perimeter per unit length). I.e. the feature weights are proportional to the sum of Spearmans rho with respect to rho_TL and rho_dPdt. We checked that our new combined size feature is as correlated with TL and dPdt as any of the individual size features are.

Linear model specifications

We used the 'fitlm()' MATLAB function when fitting the linear regression models, which contain an intercept (constant) term and one linear term per predictor variable, (*1. 'combined size feature', 2. 'number of outgoing lumenal network connections', 3. 'mean distance to the epithelial mesenchymal border', 4. 'mean lumen width', 5. 'loop eccentricity')*.

Neural network model specifications

We used the 'fitrnet()' MATLAB function for fitting our regression neural networks.
Hyperparameters:
Input layer = 5 features, (the features are: *1. 'combined size feature', 2. 'number of outgoing lumenal network connections', 3. 'mean distance to the epithelial mesenchymal border', 4. 'mean lumen width', 5. 'loop eccentricity'*.
Number of hidden layers = 2. The first layer has 100 neurons and the second 10, first layer is followed by a ReLu activation layer. The final output layer is one neuron (with identity function). An explorative hyperparameters search (varying width and depth of the NN) was performed showing that other models with similar total numbers of parameters gave similar prediction results.
Loss function: Mean squared error, (MSE).
Solver/Optimizer: limited-memory Broyden-Fletcher-Goldfarb-Shanno quasi-Newton algorithm (LBFGS).

Mini batch size = 1.

Training was stopped if the validation loss was smaller than the minimum validation loss recorded so far, for more than 6 iterations in a row, (since this indicates that further training is overfitting the model on the training data and causing an increase in validation loss).

Division of data into training and validation:

One loop time course consists of all the images of the same loop tracked over time. We divided the time course dataset in two: training and validation. (Training - 106 loop time courses, 7515 images, Validation 66 loop time courses, 4146 images). Note that for some of the time courses (49 out of 172) we do not observe loop closure (either because the loop moves out of frame or because the movie ends before loop closure or in rare cases because the lumen breaks). This means that the dataset used for predicting 'Time left' is smaller than the one used for predicting 'Contraction/expansion speed'. 76 time courses for training (4651 images) and 47 time courses for validation (2315 images).

The training/validation division of the data set was done by finding closets pairs of loop time courses via k nearest neighbor search in the space spanned by the time course features *'total time course duration', 'average number of lumen branch points on loop', 'average distance of loop to border of explant', 'average loop size'* and *'average loop long axis'*. Each member of such a *'closest pair'* was then put in the training set and in the validation set respectively. The remaining time courses were all put in the training dataset. This pairing and division of loop time courses was done to make sure that training and validation sets contained relatively similar types of data. Note that we never want training and validation sets to contain data/images from the same time course, since the similarities that a loop image has to itself taken at an earlier/later time point causes more complex models to overfit.

Tracking plot scripts for plot generation

The tracking plots (*Fig 3E and SFig 6F-G*) were generated using custom scripts made in R (v 4.2.2) and several R packages (see STable6). The code and datasets used to generate the plots have been deposited in Zenodo and can be accessed using the following link https://doi.org/10.5281/zenodo.8248940.

Tables

STable 1: Live imaging acquisition specifications

Figure (Fig) or Movie (M)	Description	Imaging system	Imaging type	Time steps (min)	Laser Lines (%)	Gain	Pinhole	X,Y,Z resolution (µm)
Fig2A/ M2	Explanted E9.5 posterior foregut expressing ZO1-GFP visualizing the evaginating pancreatic buds.	Zeiss LSM780	Z-stack, sequential acquisition	8	488:1% 561: 1.5% (PMT for DIC acquisition in the 488 track)		GFP: 2.01AU mCherry: 2.40AU	0,69 x 0,69 x 1 µm
Fig2C/ M7a and M7b	Explanted E10.5 posterior foregut expressing Mucin-mCherry:ZO1-GFP that visualizes the onset of secondary network transformation.	Zeiss LSM780	Z-stack of 40 µm, sequential acquisition (unidirectional scan)	8	488:1% 561: 1.5% (PMT for DIC acquisition in the 488 track)		GFP: 2.01AU mCherry: 2.40AU	0,69 x 0,69 x 1 µm
Fig3A-D/M12-15	Explanted E10.5 posterior foregut expressing Mucin-mCherry:ZO1-GFP to visualize the unique modes of secondary network transformation.	Zeiss LSM780	Z-stack of 40 µm, sequential acquisition (unidirectional scan)	8	488:1% 561: 1.5% (PMT for DIC acquisition in the 488 track)		GFP: 2.01AU mCherry: 2.40AU	0,69 x 0,69 x 1 µm
Fig3Gi-iii and	Explanted E10.5	Zeiss	Z-stack of 40	4	488:1%	GFP:	GFP:	0,69 x 0,69

Movies16a-c	posterior foregut expressing Mucin-mCherry:ZO1-GFP recorded to track the frequency of each event during secondary network transformation.	LSM880	µm, sequential acquisition		561: 1.5% (PMT for DIC acquisition in the 488 track)	1150 mCherry: 1000 T-PMT : 300	1.88AU mCherry :2.25AU	x 1 µm
SFig3B-D/ M3	Explanted E10.5 posterior foregut expressing Mucin-mCherry:ZO1-GFP that demonstrates the acquisition of Mucin in more mature pancreatic lumens already marked by ZO1.	Zeiss LSM780	Z-stack of 50µm, sequential acquisition	8	488:1% 561: 1.5% (PMT for DIC acquisition in the 488 track)	GFP: 1150 mCherry: 1000 T-PMT : 300	GFP: 1.88AU mCherry :2.25AU	0,69 x 0,69 x 1 µm
Fig5A, Fig6A-D, SFig7, SFig9, SFig 11 / M17-24	Muc1-mcherry mid gestation live imaging	Zeiss LSM780	Time-lapse, multi position, Z-stack, Simultaneous acquisition	10	488:1% 561: 1,5%	GFP: 973 mCherry: 1009 T-PMT : 250	1,73AU	0,35 x 0,35 x 1 µm

STable 2: Primary Antibodies:

Name	**Host**	**Dilution**	**Source**	**Identifier**
Ezrin [3C12]	mouse	1:1000	Abcam	ab4069 RRID:AB_304261

E-cadherin	Rat	1:100	Takara Bio	M108 RRID:AB_2895157
Fibronectin	Rabbit	1:200	Abcam	ab2413 RRID:AB_2262874
GFP	Chicken	1:500	Abcam	ab13970 RRID:AB_300798
GFP	Goat	1:500	Abcam	ab5450 RRID:AB_304897
Glucagon	Mouse	1:1000	Sigma/Merck	G2654 RRID:AB_259852
Integrin a5	Rabbit	1:100	Abcam	ab150361 RRID:AB_2631309
Insulin	Guinea Pig	1:750	Agilent	A056401-2 RRID:AB_2617169
Laminin	Rabbit	1:200	Sigma	L9393 RRID:AB_477163
Mucin 1	Armenian Hamster	1:1000	Thermo Scientific	HM-1630-P0 RRID:AB_54620
Pdx1	Guinea Pig	1:1000	Beta Cell Biology Consortium	AB2028 RRID:AB_10014623
Pdx1	Guinea Pig	1:1000	Abcam	ab47308 RRID:AB_777178
RFP-biotin IgG	Rabbit	1:100	Abcam	ab34771 RRID:AB_777699

STable 3: Secondary Antibodies:

Name	Host	Dilution	Source	Identifier
Cy3 anti Rat IgG	Donkey	1:1000	Jackson ImmunoResearch	712-165-150 RRID:AB_2340666
Alexa Fluor® 647 anti Armenian hamster IgG	Goat	1:1000	Jackson ImmunoResearch	127-605-160 RRID: AB_2339001
Alexa Fluor® 488 anti Rabbit FAB fragment	Donkey	1:1000	Jackson ImmunoResearch	711-547-003 RRID: AB_2340620
Dylight® 405 anti Guinea Pig IgG	Donkey	1:1000	Jackson ImmunoResearch	706-475-148 RRID: AB_2340470
Alexa Fluor® 647 anti Rat IgG	Donkey	1:500	Jackson ImmunoResearch	712-605-153 RRID: AB_2340694
Cy3 anti Armenian hamster IgG	Goat	1:500	Jackson ImmunoResearch	127-165-160 RRID: AB_2338989

STable 4: Mouse strains:

Name	Source	Identifier
C57BL/6BomTac	Taconic	B6JBOM-F/M
Zo1-GFP	Terry Lechler lab, Duke University	(Foote, Sumigray, and Lechler 2013)

Muc1-mcherry	This paper	N/A

STable 5: Oligonucleotides

Purpose	**Name**	**Source**	**Sequence**	**Product size**
Recombineering primer for GalK cassette (50bp homology arms in lower case)	**RPgK1**	This paper	gcagtctctcttataccaacccagctgtggtgaccacttctgccaacttgCCTGTTGACAATTAATCATCGGCA	1331bp with RPgK2
Recombineering primer for GalK cassette (50bp homology arms in lower case)	**RPgK2**	This paper	tgagggagcagaccgccaaagctgccccaagtgggtgggggtgacttgctcTCAGCACTGTCCTGCTCCTT	
Recombineering primer for mCherry with Gly,Gly,Ser linker (green cursive) (50bp homology arms in lower case)	**RPmC1**	This paper	gcagtctctcttataccaacccagctgtggtgaccacttctgccaacttg*GGTGCCTCA*ATGGTGAGCAAGGGCGAGGAG	820bp with RPmC3
Recombineering primer for mCherry without linker (50bp homology arms in lower case)	**RPmC2**	This paper	gcagtctctcttataccaacccagctgtggtgaccacttctgccaacttgATGGTGAGCAAGGGCGAGGAG	811bp with RPmC3
Recombineering primer for mCherry (50bp homology arms in lower case)	**RPmC3**	This paper	tgagggagcagaccgccaaagctgccccaagtgggtgggggtgacttgctcCTACTTGTACAGCTCGTCC	
PCR insertion site primer Also used for genotyping	**pAf**	This paper	ATC GGG GTT TTA CCT GGA AG	190/199 bp with pAr
PCR insertion site primer Also used for genotyping	**pAr**	This paper	ACC TTG AAG CGC ATG AAC TC	

PCR insertion site primer	**pBf**	This paper	CAC CAT CGT GGA ACA GTA CG	218 bp with pBr
PCR insertion site primer	**pBr**	This paper	ACG TAG TTG AGG CGC TTG AC	
Genotyping primer	**ZO1-GFP transgene forward**	(Foote, Sumigray, and Lechler 2013)	GCT TTC AGA TGA TTG TAG CC	ZO1-GFP forward and reverse transgene should together amplify a 400bp product.
Genotyping primer	**ZO1-GFP transgene reverse**	(Foote, Sumigray, and Lechler 2013)	GAA CTT GTG GCC GTT TAC GTC G	
Genotyping primer	**ZO1-GFP forward unmodified**	(Foote, Sumigray, and Lechler 2013)	CTT TCA GAT GAT TGT AGC CAG C	ZO1-GFP forward and reverse unmodified should together amplify a 420bp product.
Genotyping primer	**ZO1-GFP reverse unmodified**	(Foote, Sumigray, and Lechler 2013)	CCT TCA TCA GTT CCA ACA AAT GC	

STable 6 : Software and Algorithms

Name	**Source**	**Webpage**
Fiji 2.0/ImageJ version 1.53t	(Rueden et al. 2017)	http://imagej.nih.gov/ij
Imaris Essentials version 8.4, 9.0-10.0	Bitplane/Andor	https://imaris.oxinst.com
MATLAB R2022b with the Statistics and Machine learning toolbox and Computer Vision Toolbox	MathWorks	https://se.mathworks.com/products/matlab.html
R version 4.2.2	(The R core Team 2021)	https://www.R-project.org
R packages	tidyverse (v 1.3.2) (Wickham et al. 2019), plotly (v 4.10.1) (Sievert 2020) and GenomicRanges (v 1.50.2) (Lawrence et al. 2013)	N/A

STable 7 : Additional key reagents, equipment and resources

Name	**Source**	**Identifier**
35 mm glass bottom dish	WillCo	GWST-3512
µ-Slide 8 Well high	Ibidi	80801
TSA-Fluorescein kit	Akoya BioSciences	NEL701A001KT
Blocking Reagent	Akoya Biosciences	SKU FP1012 RRID: N/A
Fibronectin bovine protein	Thermo-Fisher	33010018
Media M-199 with phenol red	Gibco/Thermo Fisher	31150022

Media M-199 without phenol red	Gibco/Thermo Fisher	11043023
Zeiss LSM 780 inverted confocal scanning microscope equipped with PECON XL incubator, heating insert, and temperature, humidification, and CO2 modules	Zeiss and PECON	RRID:SCR_020922
Objective: C-Apochromat 40x/1.20 Water Corr	Zeiss	RRID: N/A
Objective: Plan-Apochromat 40x/1.30 Oil DIC	Zeiss	RRID: N/A
Objective: Plan-Apochromat 63x/1.40 Oil DIC	Zeiss	RRID: N/A
Zeiss LSM 880 with Airyscan inverted confocal scanning microscope equipped with PECON XL incubator, heating insert, and temperature, humidification, and CO2 modules	Zeiss and PECON	RRID:SCR_020925
Leica SP8 inverted laser scanning confocal microscope	Leica	RRID: N/A
Objective: Plan-Apochromat CS2 20x/0.75 IMM CORR	Leica	RRID: N/A 11506343
Objective: Plan-Apochromat CS2 63x1.30 Glyc CORR	Leica	RRID: N/A 11506353
Zeiss axioplan2 widefield fluorescence microscope	Zeiss	RRID: N/A

Acknowledgements

We thank Jette Larsen, Anna Månsson and Diana Klüver Hansen for technical assistance. We thank Roger Tsien, Howard Hughes Medical Institute Laboratories for the pmCherry-N1 plasmid, and Terry Lechler at Duke University for the ZO1-GFP mice. We acknowledge

assistance and support for computational resources and infrastructure via the Health Data Science Sandbox (https://hds-sandbox.github.io) funded by the Novo Nordisk Foundation (grant number NNF20OC0063268). We acknowledge the Danstem Imaging platform and the Core Facility for Integrated Microscopy, Faculty of Health and Medical Sciences, University of Copenhagen for use of microscopes and image analysis work stations. We acknowledge the Lund University Transgenic Core and the University of Copenhagen Core Facility for Transgenic Mice for oocyte injections. We thank and acknowledge Casper Øbro for his expertise and skills used to generate the 3D illustrations used in the schematic figures of this paper. PN and JMK was supported by the Novo Nordisk Foundation grant number NNF17OC0028360 and JARH by the Novo Nordisk grant number NNF20OC0063268. SH was supported by DFF grant number 6110-00091B. The Novo Nordisk Foundation Center for Stem Cell Biology was supported by Novo Nordisk Foundation grant number NNF17CC0027852.

Author contributions

PN and AJ conceived the study; designed, conducted, and analyzed the experiments and wrote the manuscript. SH conceived the study, analyzed the experiments, developed the image analysis methods, performed the computational modeling, created artwork and wrote the manuscript. CE performed the ECM staining and imaging and edited the manuscript. JMK assisted with embryo dissection, explant culture, immunostaining, and image analysis. JARH developed the tracking graph plots (computational script and aesthetics). HS conceived the study, acquired funding and edited the manuscript.

Declaration of interests

The authors declare no competing interests.

Figure legends

Figure 1:

Generation of the Mucin1-mCherry reporter line and validation of the reporter's representation of endogenous Mucin expression. A: Schematic of the targeting strategy for the reporter construct which consists of the mCherry sequence fused to exon 7 of the Mucin1 gene. Primer sequences are found in STable 5 B-E: mCherry as detected directly in freshly isolated tissue including the adult pancreas (B), colon (C), duodenum (D), and lung (E) of an adult transgenic (TG) mouse by fluorescence microscopy. Fi-Hii: Direct mCherry

detection in TG embryonic tissue by fluorescence microscopy after fixation matches Muc1 antibody staining in E12.5 duodenum (Fi-ii), stomach (Gi-ii) and E13.5 lung (Hi-ii). Ii-Kiii: Detection by fluorescence microscopy after fixation in adult TG (Ii), but not wiltype (WT) (Ji) and embryonic TG (Ki) pancreatic epithelium also matches Muc1 antibody staining (Iii-Kiii), with exception of a few duct-like structures which are not detected with the Muc1 antibody (arrowhead). Li-ii: Stitched confocal mosaic tile scan from a whole E12.5 pancreatic explant after 3 days ex vivo culture. Mi-ii: Confocal scan from the tip of a E9.5 lung bud after 6 days ex vivo culture. Ni-Oiii: Maximum intensity 3D projection of confocal images of pancreatic TG (Ni-Niii) and WT (Oi-Oiii) explants cultured for 2 days after explanting at E10.5 and fixation and staining for RFP and Muc1. Bar is 20 µm in B-K and 100 µm in L-O. DIC= Differential Interference Contrast.

Figure 2: Lumenal network transformation is comparable in vivo and ex vivo

Ai-iii: Representative time frames from 4D imaging of a ventral pancreatic bud expressing ZO1_GFP reporter (Cyan). The TIFFs depict CPL budding out from and perpendicular to the foregut. White dashed outline estimated the outer epithelium, inner dashed lines mark the foregut, yellow dashed line marks the CPL. Inset shows an overview of the entire pancreas on which direction of growth (A, anterior, P, posterior) is marked by arrows. Bi Is a schematic to help orient the WMIF images in panels B and D, Bii-iv: MIP of embryonic foreguts (espectively at E9.0, E9.5 and E10.0) depicting equivalent lumenal topology observed in the 4D imaging of CPL budding (see A). Ci-iv: Representative time frames from 4D imaging of a ventral pancreatic bud expressing the Mucin-mCherry(magenta) and ZO1_GFP (Cyan) double reporter. The TIFFs depict the transformation of the CPL into a secondary primitive plexus network. Arrows/spots highlight examples of different transformative topological events observed in the 4D imaging dataset (white large open = extension, white small closed = bifurcation, red = De Novo, Blue = BPP, Yellow = BPT). Di-iv: MIP of embryonic foreguts (i and ii E10.5, iii E11.0, iv E11.5) depicting equivalent lumenal topology observed in 4D imaging of a CPL transforming into a secondary network (C). Arrowheads denote the same structures detailed in Ci-iv. Grey boxed areas in Diii highlight the close proximity between the branching CPL and secondary lumenal site that are likely a static depiction of BPT. Gray arrows in panels B and D are used to point out autofluorescence from blood cells.

Figure 3: The pancreatic lumenal network is largely derived from the central primary lumen through expansion and rearrangement of apical membranes

A-Di-iii: Representative time frames from 4D imaging of the remodeling lumenal pancreatic network expressing ZO1_GFP (Cyan) and Mucin_mCherry (magenta). The TIFFs depict the different lumenal events occurring during network growth. (A) extension (B) temporary break points (C) permanent break points (D) derived and de novo foci. A-Div are skeletonised lumenal schematics summarizing the lumenal events. Arrows and spot colours highlight different lumenal events: white = the original lumenal branch, or fragment, yellow is a BPT, purple is a BPP, red is a de novo foci and blue is a derived foci. In panels D the tracked foci are further highlighted by a dashed outline.

E: A tracking plot displaying the frequency of tracked lumenal events, occurring over time, to contribute to the proximal distal growth and transformation of discrete lumenal branches). The plot visualizes the high frequency of lumenal breaking events (dashed line, downward arrows define the point at which the lumen unifies) and derived foci (unfilled circles) are observed during lumen growth. In contrast de novo foci (unfilled square) occur relatively infrequently. F: Bar chart displaying the quantified frequency of each lumenal event observed in the 3 tracked live imaging datasets. Gi-iii: Representative time frames from 4D imaging of the remodeling lumenal pancreatic network expressing ZO1_GFP (Cyan) and Mucin_mCherry (magenta). The TIFFs shown are a visual representation of the quantitative tracking data shown E and data set 3 in F. Each spot colour represents a different lumenal branch, light spots mark lumenal extension, dark spots mark breaking events and foci (Imaris tracking spots are further highlighted with an arrow of the same color .

Figure 4:

Characterization of loops and loop formation.

A: Segmented and 3D reconstructed mucin1 stained E14.5 *in vivo* pancreas (left) and corresponding midline skeleton with loops highlighted in different colors (right). White bar is 100 µm. **B:** Cartoon illustrating the three different samples types used for analysis of loops: Bi) Muc1 and Ecad stained E14.5 WT fixed *in vivo* pancreas Bii) Muc1 and Ecad stained fixed explants (*ex vivo*) from E11.5 WT embryos cultured for 3 days, Biii) Muc1-mcherry pancreas explanted at E12.5 and grown *ex vivo* for 48 hs, followed by live time lapse imaging for up to 48 hs. For the latter, only approximately one quarter of the total pancreas was kept in the field of view and tracked. **C:** Loop size distribution for the three sample types, measured as

the projected area onto the 2D xy plane of the loop formed by lumen midline (this feature was chosen to enable a size comparison between the fixed and live datasets). The size classes Small (S, blue), Medium (M, orange), Large (L, yellow) and Extra Large (XL, purple) are color coded in subsequent figures. The count is normalized by the total number of loops observed in each size bin. n=7/3/7 in vivo/ex vivo fixed/ex vivo live samples. Black dotted line signifies approx. upper size limit for loops in *ex vivo* live due to field of view limitation. **D:** Quantification of cinching and loop neoformation in n=7 movies of *ex vivo* live samples. (Di and Dii) hole size is here the size of the loop right after formation. (Diii) hole size is here the size of the loop right before cinching occurs. **E:** Examples of loops from different size categories from ex vivo samples explanted at E12.5, grown for 4 days, and stained for Muc1 and E-cadherin. The upper row shows a single z-plane from the middle of the loops. The lower row shows a maximum intensity projection. Arrows point to holes in loops. The bars are 20 µm. **F:** Quantification of loops without epithelial cells in the central hole of the loop as a function of size group in *ex vivo* fixed (n=3) and *in vivo* fixed (n=7) samples. Size group S is significantly different from group L and XL, and size group M is significantly different from XL (Krusksal Wallis test P<0,05).

Figure 5:

Tracking of ductal loop structures in mid-gestation pancreas

A-B: Tracking loop structures and segmenting lumen plus epithelial/mesenchymal border in live imaging of pancreatic explant culture imaged every 10 min, (MIP from one out of 6 experiments/movies shown in C and D, (corresponding to light blue dots/Exp. 1) at (Ai) T= 0 hours 10 min, (Aii) T = 12 hours 30 min and (AiiI) T = 28 hours 20 min). **B:** Same data as A but showing lumen segmentation in gray, tracked loop structures with unique color ID (same color across time means same loop). Note that there may be loop structures besides those highlighted, the ones highlighted have all been inspected and verified as bonafide loop structures in 3D. For some parts of the tissue, the thickness was too high and signal thus too low to properly distinguish loop structures. White lines are approximate placement of epithelial mesenchymal interface. **C:** Colored dots: Median number of loop structure per lumen length for each experiment/movie separately. Black line: Mean number of loops per lumen length across all experiments/movies with moving mean smoothing (window size 30 timepoints) +-SEM. Pearson's correlation coefficients (ρ) between median number of loops and time for each experiment/movie separately are [-0.8848 -0.9327 -0.2786 -0.9659

-0.6325 -0.9624], median ρ = - 0.78, (all p values are below 0.001). **D:** Analysis of the ratio between number of end points and branch points before and after 10 hours of imaging, showing that the fraction of nodes that are end points go up with time. n=6 experiments. p= 9.23e-6 with Wilcoxon rank sum test. **E:** 172 loop structures segmented and tracked in 7 movies (of 5 different explants). Of these, two movies have duration 50 hours, five have duration 28 hours and 30 min, imaging was done every 10 min. A range of features of the loops projected onto the XY plane, where extracted over time: *'inner hole area', 'inner hole diameter', 'convex area', 'perimeter of convex hull', 'minor / major axis length of an ellipse fitted to the inner loop hole segmentation', 'lumen loop and hole total area', 'number of branch points/outgoing lumens', 'distance to epithelial/mesenchymal interface', 'mean lumen width', 'eccentricity of an ellipse fitted to the inner loop hole segmentation'.* Here we show loop trajectories of the size feature '*inner hole area*' measured in $(\mu m)^2$ over time, separated between trajectories where we observed loop closure (Ei) and trajectories where we did not (Eii). Hollow circle marks a loop forming event. Triangle marks a loop cinching event. A line ending/starting with no symbol means that the loop exits/enters the field of view. Full circle marks a loop closure event.

Figure 6:

Loop closing dynamics in mid-gestation pancreas

A: Example of a branch with 8 different loops forming, contracting, and closing over time. Magenta: Muc1. Colored lines: segmentation of loops. **B:** Example of a gradually constricting loop structure that ends up closing. Magenta: Muc1. White line: segmentation of loop. **C:** Example of a loop breaking event. Magenta: Muc1. White line: segmentation of loop. **D:** Example of a loop 'cinching' event'. Magenta: Muc1. White line: segmentation of loop. **E:** Events that reduce the number of loops in the network are lumen breaking events (if the lumen breaking is participating in a loop structure) and loop closing events. These two types of events were counted for n = 7 different explants (data gathered from 14 movies. 5 explants have 2 positions/movies, 1 explant 3 positions/movies and 1 explant have 1 position/movies). Distributions pass Anderson-Darling normality test so p value = 2e-7 is found via two sample T test. **F:** Cartoon of the two types of loop closure dynamics. (Fi) Gradual constriction followed by loop closure (Fii) cinching off smaller loop that then undergoes loop closure.

Figure 7:

Static loop features associated with dynamic behavior (contraction and loop closure):

A: Y axis: Metric for long term dynamic loop behavior - *'Time left before loop closure in hours'*. X axis: Loop size groups. **B:** Y axis: Metric for short term dynamic loop behavior - *'Mean loop contraction/expansion rate in cell loss/gain per day'* (contraction speed of loop perimeter per unit length), X axis: Loop size groups. **C:** Overview of the 5 static loop features extracted from the live imaging data. 1) Combined size feature. The loop features that are most correlated with both the two long term and short term target variables (*time left* and *contraction speed*) are those that quantify loop size in different ways. We therefore designed a combined size feature and divided our loop time courses into 4 size categories (S, M, L, XL see also S Figure 10) in order to study the effect of other static features relating to shape and placement in the organ within groups of similar loop size. The original six size features contributing to the combined size feature were: *'inner hole diameter', 'convex area', 'perimeter of convex hull', 'minor/major axis length of an ellipse fitted to the inner loop hole segmentation', 'major axis length', 'lumen loop and hole total area'*, z scored and weighted in the new combined size feature according to their correlation with the two target variables. 2) Connectivity feature, the mean number of branch points/outgoing lumens. 3) Organ placement feature, the mean distance to epithelial/mesenchymal interface in microns. 4) Lumen width feature, the mean lumen width in microns. 5) Elongation feature, the eccentricity of an ellipse fitted to the inner loop hole segmentation. **D-E:** Mean absolute error (MAE) on training/validation data for linear and neural network models predicting 'Time left before loop closure' and 'loop contraction speed' normalized by base model MAE. **F:** We estimated the change in time left when the number of branch points is changed (i.e. finding the slope dTL/dnumBRP of a linear fit) within even smaller loop size groups, than S, M, L and XL, in order to make sure that the correlation we observe between time left and number of branch points is not caused by the strong correlation between number of branch points and loop size. We see that these slopes were consistently positive as expected, if the effect still holds even when loops of the same size are compared. The colored 'notch' areas show the 95% confidence intervals of the median slope for each size group (S, M, L and XL). None of these confidence intervals cross zero which shows that a higher number of branch points is associated with slower closure. Note that the apparent trend that L and XL size groups have a steeper slope is not significant. **G:** Mean eccentricity of loops in size groups L and XL (mean is taken over time) is higher in loops that go through one or more cinching

events during the time course, P value is 0.0262 (Wilcoxon Ranksum test). **H:** We found a positive correlation between *time left* and *mean distance to epithelial/mesenchymal interface*. Since there is also a slight positive correlation between category and distance to the organ edge we look at correlation in our size categories separately (S Hi, M Hii, L Hiii) and note that the strongest effect of placement in the organ on *time left* seems to be in the M and L groups, where Spearman's rho is >0.4. Number of time courses in each category is, Small: n=114. Medium: n=72. Large: n=33.

Figure 8:

Comparative analysis of epithelial and lumenal networks

A: (Ai) - Segmented and 3D reconstructed epithelium E14.5 *in vivo* pancreas. (Aii) - 'Outer tree', corresponding midline skeleton of epithelium segmentation. (Aiii) - Segmented and 3D reconstructed lumenal network E14.5 *in vivo* pancreas. (Aiv) - 'Inner tree', corresponding midline skeleton of lumen segmentation. **B:** The number of endpoint point (ENP) nodes in 'inner tree' per 'outer tree' (ENP) (median ~2.5) and the number of branch point (BRP) nodes in 'inner tree' per 'outer tree' (BRP) (median ~3.2). In vivo fixed. N=7. **C:** Ci - detail of epithelial branch, Cii - epithelium midline with branch points (BRP) and end points (ENP) highlighted in blue and pink, Ciii - detail of lumen in same branch, Civ - lumenal midline with branch points (BRP) and end points (ENP) highlighted in blue and pink. **D-E:** Example of lobe clefting event. Di-Ei: T = 8h 50 min. Dii-Eii: T = 14h 30 min. Diii-Eiii: T = 25. **D:** Green: MIP of probability of pixel lumen class predicted by Random Forest. Blue: MIP of probability of pixel epithelial/mesenchymal interface class predicted by Random Forest. White dashed line: highlighting a clefting lobe. **E:** Red: Raw Muc1 signal (appears yellow because of green overlay). Green: probability of pixel lumen class predicted by Random Forest. Gray: Raw DIC channel. **F:** Count of the number of lumenal tips present in lobes before clefting. **G:** We tracked branching events in the outer tree and backtracked the inner tree to the time point immediately preceding an outer three branching event and recorded the number of lumens in two live imaging datasets of Muc1-mcherry E14.5 +2 days culture dorsal pancreata. We here define clefting as the bifurcation (type Gi and Gii event) of a pre-existing epithelial lobe, and lateral branching (type Giii and Giv). In the first dataset, 9 type Gi/Gii clefting events and no type Gii/Giv events were observed in the outer tree consisting of 5 epithelial main branches. In the second dataset, 8 Gi/Gii clefting events and one lateral branching type Giii/Giv event was observed in the outer tree consisting of 2 epithelial main branches. All type Gi events were preceded by at least two lumenal tips inside the lobe. We observed only

one type Giii event, which was preceded by one lumen protruding at the branching site. For total 17 type Gi events, the number of lumen tips observed inside lobes before clefting was [3 2 2 3 4 3 3 2 2 2 3 3 4 3 2 3 2], mean-+std = 2.7059+- 0.686, median = 3, min = 2, max = 4.

Supplementary Figure Legends

S Figure 1:

Weight and fasting blood glucose is not perturbed by the expression of the Mucin-mCherry transgene.

A: Muc1-mCherry 0M females had reduced body weight (p=0,001 unpaired t-test), while males had a tendency at reduced body weight at 8-week of age compared to WT. **B:** Muc1-mCherry 0M had normal fasting blood glucose at 8-weeks. n= 4 TG males, n= 2 WT littermate males, n= 3 TG females, n= 6 WT females. **C:** Muc1-mCherry 5M females had a slightly reduced body weight at 8-week of age compared to WT (p=0,0002 unpaired t-test), while males had the same bodyweight. **D:** Muc1-mCherry 5M had normal fasting blood glucose at 8-weeks.n= 6 TG males, n= 2 WT littermate males, n= 3 TG females, n= 8 WT females. **E:** Muc1-mCherry 12M mice had a normal body weight at 8-week of age compared to WT. **F:** Muc1-mCherry 12M had normal fasting blood glucose at 8-weeks.n= 8 TG males, n= 7 WT littermate males, n= 7 TG females, n= 6 WT females. **G:** Muc1-mCherry 2F male mice had a slightly reduced body weight (p=0,04 unpaired t-test, while female mice had a normal body weight at 8-week of age compared to WT. **H:** Muc1-mCherry 2F had normal fasting blood glucose at 8-weeks.n= 3 TG males, n= 3 WT littermate males, n= 4 TG females, n= 7 WT females.

S Figure 2: Muc1 expression and the differentiation of pancreatic precursors to mature cell types is not perturbed by the expression of the Mucin-mCherry transgene.

A-B: Representative maximum intensity projections of whole mount IF on a E14.5 Muc1-mcherry **(A)** and a WT litter mate **(B)** pancreata stained for insulin, E-cadherin and Mucin1 and cleared in BABB. Bar=100µm in A-B. **C-D:** Quantification of antibody positive volumes as segmented using Imaris software. **C:** E-cadherin total volume (µm3). **D:** Muc1 volume as fraction of E-cadherin volume. **E:** Insulin volume as fraction of E-cadherin volume. T-tests comparing r all WT and all TG E14.5 embryos shows no significant difference between TG and WT. n=9 TG embryos and n=6 WT littermate embryos. n=2-4 embryos of 5M, 12M and 2F substrains were tested and the results pooled, as these substrains were not

significantly different by one-way ANOVA (p=0,60 for Muc1/Ecad, and p=0,1 for Ins/Ecad). **F-G:** Representative maximum intensity projection of IF staining of E12.5 explants from the 5M substrain after 4 days ex vivo growth including either 48 hours imaging **(F)** or 48 hours culture in the same on-stage incubator without imaging **(G)**. Stained for E-cadherin,Muc1, Amylase and insulin. These samples were not cleared and thus appears darker in the middle. Bar=150µm in F-G.

S Figure 3: Hierarchy of endogenous and reporter visualized Mucin expression comparative to ZO1-GFP expression in live and WMIF pancreatic foreguts.

Ai-iii: Representative time frames from 4D imaging of an E9.75 pancreatic bud expressing Mucin-mCherry (Magenta). The TIFFs depict the gradual onset of Mucin expression (absent in time point T0 (ai, asterisk)), that begins as distal foci (aii, white arrowheads) that over time expands proximally toward the foregut (i.e. toward the time stamp). White dashed outline marks the edge of the pancreatic epithelium approximated from the DIC channel (shown as inserts top right). **Bi:** Representative time frames from 4D imaging of an E10.5 pancreatic bud expressing Mucin-mCherry (Magenta) and ZO1-GFP (Cyan) reveals consistent ZO1-GFP expression and variable Mucin-mCherry reporter expression in dorsal and ventral buds (visible by DIC, outlined in white dashed line), **Bii-iv:** same frame as (B) with Mucin-mCherry (Magenta) and ZO1-GFP (Cyan) alone in tandem, or alone. **Ci-iii and Di-iii:** Magnified views of the expression data shown in B panels displayed as a single optical Z-plane focusing on the dorsal (C panels) and ventral (D panels) buds (inset shows the same area as a MIP). We observe very little Mucin-mCherry expression in the ventral bud CPL compared to the dorsal bud CPL (Di vs Ci). In contrast ZO1-GFP expression is expressed apically throughout both buds lumens (Dii vs Cii). Arrowheads highlight yellow CPL stalk and white CPL cap, VB= ventral bud, DB= dorsal bud. Ei-iv MIP of an E10.0 dorsal bud stained for endogenous Mucin, ECDD2 and the reporter ZO1-GFP shows a similar hierarchy of Mucin and ZO1-GFP expression in fixed in vivo samples. Eii shows Mucin is absent in most of the CPL stalk (pink brackets) and in the foregut, in contrast to ZO1-GFP was detected throughout the CPL stalk (green brackets) and into the foregut. Green arrows highlight ZO1-GFP marked endothelial cells.

S Figure 4: WMIF of multiple apical proteins reveal consistent CPL transitions and variable luminal patency during secondary network establishment.

A-C: MIP of WMIF imaged embryonic foreguts (ranging from E10.0 to E11.0) stained for either ZO1-GFP (Ai, ii – Ci,Cii) or EZRIN (Ai, ii – Ci,Cii) depict similar CPL morphologies also

visualized with Mucin WMIF in Fig 2Di-iiii. Di-Gi and Hiii show MIP of WMIF imaged embryonic foreguts (ranging from E10.0 to E11.0) stained for various apical proteins to visualize different stages of CPL and network morphology. **Dii-Gii, Hi and Hii:** For each MIP we viewed the sample orthogonally and identified areas of luminal patency (open arrowhead) and lack of patency (filled arrowhead), both between samples and within samples. Panels Hi and Hii are orthogonal slices through the MIP (Hiii) at different levels of the CPL.

S Figure 5: Identifying endothelial expression of ZO1-GFP outside the pancreatic epithelium and estimating the average cell length of a pancreatic epithelial cell.

A and B: MIPs of an explant (i = overview of all tissue, ii = zoom in on pancreatic tissue) fixed directly after live imaging and WMIF stained for endothelial (PECAM, green), pancreas (PDX1, blue) and luminal (MUC1, magenta) proteins. Panel C is the last frame from the live imaging movie (endogenous ZO1-GFP signal, green). We found that the non-lumenal domains of ZO1-GFP in Ci and ii were comparable to the domain of the PECAM expression in Bi and ii (outlined in dashed red line). We could further see that the MUCIN expression domain (outlined in white dashed line in Bii) was absent of PECAM expression. **E and F:** representative samples used to quantify average cell length Di, ii, Ei ii: MIPs of pancreata stained for membrane (D panels B-CATENIN, E panels ECDD2, yellow) markers and luminal markers (Mucin, magenta). From the cap and body layers of 3 independent E10.0, E10.5 and E11.0 dorsal buds, 3 rounded and 3 elongated cell lengths were measured. Diii- iv and Ei ii are representative optical Z-slices through the MIP illustrating examples of how cell measurements were performed. **Graph F:** A scatter plot of cell length measurements, including the mean (red values along the X-axis) and SD (bars in red) of lengths grouped by cell morphology (elongated or rounded) and cell layer (cap or body) for E10.0-E11.0 dorsal buds samples. The average cell length of all the data was 8.35uM and the average of the longest (elongated cells) was 10.81uM, thus we settled on a length of more than 10uM to be a reasonable cell length cut off for categorizing a foci as de novo generated.

S Figure 6: Quantitative data to further support the conclusion that lumenal network is largely derived through expansion and rearrangement of apical membranes.

A-C: Scatter Plots visualizing the duration (i.e. length of time) - respectively - of every BPT, derived and de novo foci tracked in 3 live imaged explants forming a secondary network. **D-E**:

Scatter Plots visualizing at detection, the distance - respectively - of every derived and de novo tracked foci to a pre-existing lumen in 3 live imaged explants forming a secondary network. All scatter plots display the mean and SD bars . **F and G:** Tracking plots displaying the frequency of tracked lumenal events, occurring over time, to contribute to the proximal distal growth and transformation of discrete lumenal branches in two additional explants. The plot visualizes the high frequency of lumenal breaking events (dashed lines, downward arrow marks the point at which the lumen unifies) and derived foci (unfilled circles) are observed during lumen growth. In contrast de novo foci (unfilled square) occur relatively infrequently. **Hi-iii:** Representative time frames from 4D imaging of the remodeling lumenal pancreatic network expressing ZO1_GFP (Cyan) and Mucin_mCherry (magenta). The TIFFs shown are a visual representation of the quantitative tracking data shown in F and data set 1 in Fig 2F. **Gi-iii:** Representative time frames from 4D imaging of the remodeling lumenal pancreatic network expressing ZO1_GFP (Cyan) and Mucin_mCherry (magenta). The TIFFs shown are a visual representation of the quantitative tracking data shown in G and data set 2 in Fig 2F. In panels H and G each spot color represents a different lumenal branch, light spots mark lumenal extension, dark spots mark breaking events and foci. Imaris tracking spots are further highlighted with an arrow of the same color .

S Figure 7: Loop formation is a continuous feature through early and mid-gestation lumenal network transformations.

A-C: Representative time frames showing loop formation in the 4D imaging of pre-plexus pancreatic networks found in early gestation pancreata expressing ZO1_GFP (Green) and Mucin_mCherry (magenta). A-Ci gives an overview of the whole pancreatic explant within the imaging frame . A-Cii-iv are magnified areas, (white box in Ai-Ci) in which loops are forming over time, (inside the white box). A-C are 3 independent biological explants, in C one can see that the loop forms transiently and is not present in Civ. **D:** Example of loop formation in live *ex vivo* data. Magenta: Muc1, white dashed line: lumen outline before loop formation. White line: inner loop segmented area.

S Figure 8:

Representative maximum intensity projections (MIP) of loops (z=4-5µm) in E11.5 + 3 days *ex vivo* pancreas. **Ai-Ci:** Stained for E-cadherin, Muc1, DAPI and IT5. **Di-Gi:** Stained for E-cad, Muc1, Fibronectin (and DAPI in Gi). Gi-ii shows a single 1µm section. **Hi-ii:** Stained for

E-cadherin, Muc1 and Laminin. Bar is 20µm in Ai-ii,Di-ii and Hi-ii. Bar is 15 µm in Bi-ii and Ei-ii. Bar is 10 µm in Ci-ii, Fi-ii and Gi-Hii.

S Figure 9:

A: Data from segmenting and tracking lumenal structures in live data. Colored dots: Number of branch points measured in the XY plane for each experiment/movie separately. Black line: Mean number of branch points across all experiments/movies with moving mean smoothing (window size 30 timepoints) +-SEM. Pearson's correlation coefficients (ρ) between mean number of branch points (BPs) per lumen length and time for each experiment/movie separately are [-0.5075 -0.4790 -0.3447 -0.6437 -0.7963], median ρ = -0.51, (all p values are below 1.0e-5). **B:** Data from segmenting and tracking lumenal structures in live data. Colored dots: Number of end points measured in the XY plane for each experiment/movie separately. Black line: Mean number of end points across all experiments/movies with moving mean smoothing (window size 30 timepoints) +-SEM. Pearson's correlation coefficients (ρ) between mean number of branch points (BPs) per lumen length and time for each experiment/movie separately are [0.5781 0.3593 0.7327 0.5270 0.6805], median ρ = 0.5755, (all p values are below 0.003). **C-D:** Analysis of absolut number of end points (C) and branch points (D) before and after 10 hours of imaging normalized with total lumen length or total lumen volume visible in the movies. n=6 experiments. p= 0.0012 (C) and p= 5.44e-6 (D) with Wilcoxon rank sum test. **E:** An example of a stable rounded loop from the XL size group, widening/maintaining size over time.

S Figure 10:

A-C: Distribution of loop sizes. We study dynamic loop behavior in 4 size categories (S, blue M, orange L, yellow and XL, purple). Number of data time points per size category: small n= 2986, medium n= 3708, large n= 2706, extra large n=2122. Number of loop time courses in the different size categories: S n=133, M n= 95, L n= 54, XL n=24. Number of loop time courses in the different size categories ending with loop closure: S n=114, M n= 72, L n= 33, XL n=9. **A:** The combined size feature was used when dividing the loop data into size categories (S x>0.25, M 0.25<x <0.5, L 0.5<x <0.8, XL 0.8<x). The comb. size feature is a linear combination of the following highly correlated features: *'inner hole diameter', 'convex area', 'perimeter of convex hull', 'minor axis length', 'major axis length', 'lumen loop and hole total area'*. **B:** Inner loop hole equivalent diameter (the diameter of a circle with the same area as the segmented inner loop hole). Distribution of time points. **C:** Inner loop hole equivalent diameter (the diameter of a circle with the same area as the segmented inner loop hole).

Distribution of loop time courses. **D:** Fixed *ex vivo* data of lumens and epithelium E14.5 *in vivo* pancreas (n=3) shows that L and XL lumenal loops without non epithelial cell types present in the middle are more elongated. p value 0.028 (Wilcoxon rank sum test).
E: Fixed *in vivo* data of lumens and epithelium E14.5 *in vivo* pancreas (n=7) shows that L and XL lumenal loops without non epithelial cell types present in the middle are more elongated. p value 0.003 (Wilcoxon rank sum test). **F:** Time left before loop closure in XL loop size groups is not significantly associated with placement in the organ, (see figure 8 for S, M and L). n=9 time courses. **G:** Mean squared error loss monitored during training of 8 NN models predicting either 'Time left before loop closure' or 'loop contraction speed'. Training was stopped if the validation loss was smaller than the minimum validation loss recorded so far, for more than 6 iterations in a row, (since this indicates that further training is overfitting the model on the training data and causing an increase in validation loss).

S Figure 11:
A: Single slice (middle of z stack) from live movie time point. Green Muc1 one signal. Orange/yellow: Areas where Muc1 signal was removed. **B:** Cleaned slice from live movie time point before (Bii) and after (Bi) removal of small round bright Muc1 signals.

Movie titles

Movie metadata is included in STable1

Movie 1: Onset of Mucin-mCherry reporter expression in the pancreatic bud.
Movie 2: ZO1-GFP reporter expression illustrating CPL cap and stalk formation by lumenal evagination in the ex vivo pancreatic bud.
Movie 3: Dynamics of ZO1-GFP:Mucin-mCherry reporter expression in the early pancreatic bud
Movie 4: Immunohistochemistry illustrating in 3D lumenal evagination/budding in an E9.0 in vivo pancreatic bud.
Movie 5: Immunohistochemistry illustrating in 3D lumenal evagination/budding in an E9.5 in vivo pancreatic bud.
Movie 6: Immunohistochemistry illustrating in 3D, the oval cap and stalk CPL morphology in an E10.0 in vivo pancreatic bud.

Movie 7a: ZO1-GFP:Mucin-mCherry reporter expression illustrating in 4D secondary network generation through lumenal expansion and rearrangement initiated at the CPL (annotated, zoom

Movie 7b: ZO1-GFP:Mucin-mCherry reporter expression illustrating in 4D secondary network generation through lumenal expansion and rearrangement initiated at the CPL (un-annotated, overview).

Movie 8: Immunohistochemistry illustrating in 3D transformation and extension of the CPL prior to secondary network establishment in an E11.0 in vivo pancreatic bud.

Movie 9: Immunohistochemistry illustrating in 3D secondary lumenal network establishment surrounding a highly transformed CPL in an E11.0 in vivo pancreatic bud.

Movie 10: Immunohistochemistry illustrating in 3D an elaborate, highly disparate secondary lumenal network in an E11.5 in vivo pancreatic bud.

Movie 11: Immunohistochemistry illustrating in 3D a more connected, pre-plexus-like secondary lumenal network in an E11.5 in vivo pancreatic bud.

Movie 12: ZO1-GFP:Mucin-mCherry reporter expression illustrating in 4D lumenal network transformation through lumenal extension and bifurcation.

Movie 13: ZO1-GFP:Mucin-mCherry reporter expression illustrating in 4D lumenal network transformation via break points in lumenal extension that are temporary (BPT).

Movie 14: ZO1-GFP:Mucin-mCherry reporter expression illustrating in real time/4D, lumenal network transformation via break points in lumenal extension that are permanent (BPP).

Movie 15: ZO1-GFP:Mucin-mCherry reporter expression illustrating in real time/4D, lumenal network transformation via the contribution of foci appearing close to (<10uM, derived) and far from (>10uM, de novo) existing lumens.

Movie 16a-c: ZO1-GFP: Tracked lumenal features Mucin-mCherry reporter expression illustrating in real time/4D, lumenal network transformation via the contribution of foci appearing close to (<10uM, derived) and far from (>10uM, de novo) existing lumens.

Movie 17a-c: Examples of loop forming in Muc1-mcherry early-gestation pancreas.

Movie 18: Loop forming and closing in Muc1-mcherry mid-gestation pancreas.

Movie 19: Relating to Fig 5a. Loop tracking in Muc1-mcherry mid-gestation pancreas.

Movie 20: Relating to Fig 6d. Loop cinching in Muc1-mcherry mid-gestation pancreas.

Movie 21: Relating to Fig 6a. Multiple loops forming and closing in Muc1-mcherry mid-gestation pancreas.

Movie 22: Relating to Fig 6b. Loop constricting and closing (lower right corner) in Muc1-mcherry mid-gestation pancreas.

Movie 23: Relating to Fig 6c. Loop breaking in Muc1-mcherry mid-gestation pancreas.

Movie 24: Relating to SFig 9e. Loop widening and maintenance in Muc1-mcherry mid-gestation pancreas.

References

Araújo, Sofia J., and Marta Llimargas. 2023. "Time-Lapse Imaging and Morphometric Analysis of Tracheal Development in Drosophila." *Methods in Molecular Biology* 2608: 163–82.

Azizoglu, D. Berfin, Caitlin Braitsch, Denise K. Marciano, and Ondine Cleaver. 2017. "Afadin and RhoA Control Pancreatic Endocrine Mass via Lumen Morphogenesis." *Genes & Development* 31 (23-24): 2376–90.

Bafna, S., S. Kaur, and S. K. Batra. 2010. "Membrane-Bound Mucins: The Mechanistic Basis for Alterations in the Growth and Survival of Cancer Cells." *Oncogene* 29 (20): 2893–2904.

Bankaitis, Eric D., Matthew E. Bechard, and Christopher V. E. Wright. 2015. "Feedback Control of Growth, Differentiation, and Morphogenesis of Pancreatic Endocrine Progenitors in an Epithelial Plexus Niche." *Genes & Development* 29 (20): 2203–16.

Barlow, Haley R., Neha Ahuja, Tyler Bierschenk, Yadanar Htike, Luke Fassetta, D. Berfin Azizoglu, Juan Flores, et al. 2023. "Rab11 Is Essential to Pancreas Morphogenesis, Lumen Formation and Endocrine Mass." *Developmental Biology* 499 (July): 59–74.

Bergmann, Carsten, Lisa M. Guay-Woodford, Peter C. Harris, Shigeo Horie, Dorien J. M. Peters, and Vicente E. Torres. 2018. "Polycystic Kidney Disease." *Nature Reviews. Disease Primers* 4 (1): 50.

Cano, David A., Noel S. Murcia, Gregory J. Pazour, and Matthias Hebrok. 2004. "Orpk Mouse Model of Polycystic Kidney Disease Reveals Essential Role of Primary Cilia in Pancreatic Tissue Organization." *Development* 131 (14): 3457–67.

Chambers, J. A., M. A. Hollingsworth, A. E. Trezise, and A. Harris. 1994. "Developmental Expression of Mucin Genes MUC1 and MUC2." *Journal of Cell Science* 107 (Pt 2) (February): 413–24.

Chen, Dong-Yuan, Justin Crest, Sebastian J. Streichan, and David Bilder. 2019. "Extracellular Matrix Stiffness Cues Junctional Remodeling for 3D Tissue Elongation." *Nature Communications* 10 (1): 3339.

Cnossen, Wybrich R., and Joost P. H. Drenth. 2014. "Polycystic Liver Disease: An Overview of Pathogenesis, Clinical Manifestations and Management." *Orphanet Journal of Rare Diseases* 9 (May): 69.

Dahl-Jensen, Svend Bertel, Siham Yennek, Lydie Flasse, Hjalte List Larsen, Dror Sever, Gopal Karremore, Ivana Novak, Kim Sneppen, and Anne Grapin-Botton. 2018. "Deconstructing the Principles of Ductal Network Formation in the Pancreas." *PLoS Biology* 16 (7): e2002842.

Debnath, Jayanta, Kenna R. Mills, Nicole L. Collins, Mauricio J. Reginato, Senthil K. Muthuswamy, and Joan S. Brugge. 2002. "The Role of Apoptosis in Creating and Maintaining Luminal Space within Normal and Oncogene-Expressing Mammary Acini." *Cell* 111 (1): 29–40.

Dimitriou, Ioannis, Anastasios Katsourakis, Eirini Nikolaidou, and George Noussios. 2018. "The Main Anatomical Variations of the Pancreatic Duct System: Review of the Literature and Its Importance in Surgical Practice." *Journal of Clinical Medicine Research* 10 (5): 370–75.

Fanni, D., N. Iacovidou, A. Locci, C. Gerosa, S. Nemolato, P. Van Eyken, G. Monga, S. Mellou,

G. Faa, and V. Fanos. 2012. “MUC1 Marks Collecting Tubules, Renal Vesicles, Comma- and S-Shaped Bodies in Human Developing Kidney Tubules, Renal Vesicles, Comma- and S-Shaped Bodies in Human Kidney.” *European Journal of Histochemistry: EJH* 56 (4): e40.

Flasse, Lydie, Coline Schewin, and Anne Grapin-Botton. 2020. “Pancreas Morphogenesis: Branching in and Then out.” *Curr Top Dev Biol* 143 (November): 75–110.

Foote, Henry P., Kaelyn D. Sumigray, and Terry Lechler. 2013. “FRAP Analysis Reveals Stabilization of Adhesion Structures in the Epidermis Compared to Cultured Keratinocytes.” *PloS One* 8 (8): e71491.

Hannezo, Edouard, Colinda L. G. J. Scheele, Mohammad Moad, Nicholas Drogo, Rakesh Heer, Rosemary V. Sampogna, Jacco van Rheenen, and Benjamin D. Simons. 2017. “A Unifying Theory of Branching Morphogenesis.” *Cell* 171 (1): 242–55.e27.

Heilmann, Silja, Henrik Semb, and Pia Nyeng. 2021. “Quantifying Spatial Position in a Branched Structure in Immunostained Mouse Tissue Sections.” *STAR Protocols* 2 (4): 100806.

Hick, Anne-Christine, Jonathan M. van Eyll, Sabine Cordi, Céline Forez, Lara Passante, Hiroshi Kohara, Takashi Nagasawa, et al. 2009. “Mechanism of Primitive Duct Formation in the Pancreas and Submandibular Glands: A Role for SDF-1.” *BMC Developmental Biology* 9 (December): 66.

Hogan, Brigid L. M., and Peter A. Kolodziej. 2002. “Organogenesis: Molecular Mechanisms of Tubulogenesis.” *Nature Reviews. Genetics* 3 (7): 513–23.

Isabella, Adam J., and Sally Horne-Badovinac. 2016. “Rab10-Mediated Secretion Synergizes with Tissue Movement to Build a Polarized Basement Membrane Architecture for Organ Morphogenesis.” *Developmental Cell* 38 (1): 47–60.

Jørgensen, Mette Christine, Jonas Ahnfelt-Rønne, Jacob Hald, Ole D. Madsen, Palle Serup, and Jacob Hecksher-Sørensen. 2007. “An Illustrated Review of Early Pancreas Development in the Mouse.” *Endocrine Reviews* 28 (6): 685–705.

Kesavan, Gokul, Fredrik Wolfhagen Sand, Thomas Uwe Greiner, Jenny Kristina Johansson, Sune Kobberup, Xunwei Wu, Cord Brakebusch, and Henrik Semb. 2009. “Cdc42-Mediated Tubulogenesis Controls Cell Specification.” *Cell* 139 (4): 791–801.

Kopinke, Daniel, and L. Charles Murtaugh. 2010. “Exocrine-to-Endocrine Differentiation Is Detectable Only prior to Birth in the Uninjured Mouse Pancreas.” *BMC Developmental Biology* 10 (April): 38.

Lacunza, E., V. Ferretti, C. Barbeito, A. Segal-Eiras, and M. V. Croce. 2010. “Immunohistochemical Evidence of Muc1 Expression during Rat Embryonic Development.” *European Journal of Histochemistry: EJH* 54 (4): e49.

Larsen, Hjalte List, Laura Martín-Coll, Alexander Valentin Nielsen, Christopher V. E. Wright, Ala Trusina, Yung Hae Kim, and Anne Grapin-Botton. 2017. “Stochastic Priming and Spatial Cues Orchestrate Heterogeneous Clonal Contribution to Mouse Pancreas Organogenesis.” *Nature Communications* 8 (1): 605.

Lawrence, Michael, Wolfgang Huber, Hervé Pagès, Patrick Aboyoun, Marc Carlson, Robert Gentleman, Martin T. Morgan, and Vincent J. Carey. 2013. “Software for Computing and Annotating Genomic Ranges.” *PLoS Computational Biology* 9 (8): e1003118.

Löf-Öhlin, Zarah M., Pia Nyeng, Matthew E. Bechard, Katja Hess, Eric Bankaitis, Thomas U. Greiner, Jacqueline Ameri, Christopher V. Wright, and Henrik Semb. 2017. “EGFR Signalling Controls Cellular Fate and Pancreatic Organogenesis by Regulating Apicobasal Polarity.” *Nature Cell Biology* 19 (11): 1313–25.

Luan, Zhou, Yoshihiro Morimoto, Atsushi Fushimi, Nami Yamashita, Wenhao Suo, Atrayee Bhattacharya, Masayuki Hagiwara, Caining Jin, and Donald Kufe. 2022. “MUC1-C Dictates Neuroendocrine Lineage Specification in Pancreatic Ductal Adenocarcinomas.” *Carcinogenesis* 43 (1): 67–76.

Lubarsky, Barry, and Mark A. Krasnow. 2003. “Tube Morphogenesis: Making and Shaping

Biological Tubes." *Cell* 112 (1): 19–28.
Mamidi, Anant, Christy Prawiro, Philip A. Seymour, Kristian Honnens de Lichtenberg, Abigail Jackson, Palle Serup, and Henrik Semb. 2018. "Mechanosignalling via Integrins Directs Fate Decisions of Pancreatic Progenitors." *Nature* 564 (7734): 114–18.
Mangan, Anthony J., Daniel V. Sietsema, Dongying Li, Jeffrey K. Moore, Sandra Citi, and Rytis Prekeris. 2016. "Cingulin and Actin Mediate Midbody-Dependent Apical Lumen Formation during Polarization of Epithelial Cells." *Nature Communications* 7 (August): 12426.
Martín-Belmonte, Fernando, Wei Yu, Alejo E. Rodríguez-Fraticelli, Andrew J. Ewald, Zena Werb, Miguel A. Alonso, and Keith Mostov. 2008. "Cell-Polarity Dynamics Controls the Mechanism of Lumen Formation in Epithelial Morphogenesis." *Current Biology: CB* 18 (7): 507–13.
Marty-Santos, Leilani, and Ondine Cleaver. 2016. "Pdx1 Regulates Pancreas Tubulogenesis and E-Cadherin Expression." *Development* 143 (1): 101–12.
Mederacke, Malte, Lisa Conrad, Roman Vetter, and Dagmar Iber. 2022. "Geometric Effects Position Renal Vesicles During Kidney Development." *bioRxiv*. https://doi.org/10.1101/2022.08.30.505859.
Metzger, Ross J., Ophir D. Klein, Gail R. Martin, and Mark A. Krasnow. 2008. "The Branching Programme of Mouse Lung Development." *Nature* 453 (7196): 745–50.
Mullapudi, Sri Teja, Giulia L. M. Boezio, Andrea Rossi, Michele Marass, Ryota L. Matsuoka, Hiroki Matsuda, Christian S. M. Helker, Yu Hsuan Carol Yang, and Didier Y. R. Stainier. 2019. "Disruption of the Pancreatic Vasculature in Zebrafish Affects Islet Architecture and Function." *Development* 146 (21). https://doi.org/10.1242/dev.173674.
Nyeng, Pia, Silja Heilmann, Zarah M. Löf-Öhlin, Nina Fransén Pettersson, Florian Malte Hermann, Albert B. Reynolds, and Henrik Semb. 2019. "p120ctn-Mediated Organ Patterning Precedes and Determines Pancreatic Progenitor Fate." *Developmental Cell* 49 (1): 31–47.e9.
Packard, Adam, Kylie Georgas, Odyssé Michos, Paul Riccio, Cristina Cebrian, Alexander N. Combes, Adler Ju, et al. 2013. "Luminal Mitosis Drives Epithelial Cell Dispersal within the Branching Ureteric Bud." *Developmental Cell* 27 (3): 319–30.
Pan, Xinchao, Ulrike Schnell, Courtney M. Karner, Erin V. Small, and Thomas J. Carroll. 2015. "A Cre-Inducible Fluorescent Reporter for Observing Apical Membrane Dynamics." *Genesis* 53 (3-4): 285–93.
Pierreux, Christophe E. 2021. "Shaping the Thyroid: From Peninsula to de Novo Lumen Formation." *Molecular and Cellular Endocrinology* 531 (July): 111313.
Puri, Sapna, and Matthias Hebrok. 2007. "Dynamics of Embryonic Pancreas Development Using Real-Time Imaging." *Developmental Biology* 306 (1): 82–93.
Reichert, Maximilian, and Anil K. Rustgi. 2011. "Pancreatic Ductal Cells in Development, Regeneration, and Neoplasia." *The Journal of Clinical Investigation* 121 (12): 4572–78.
Riccio, Paul, Cristina Cebrian, Hui Zong, Simon Hippenmeyer, and Frank Costantini. 2016. "Ret and Etv4 Promote Directed Movements of Progenitor Cells during Renal Branching Morphogenesis." *PLoS Biology* 14 (2): e1002382.
Rueden, Curtis T., Johannes Schindelin, Mark C. Hiner, Barry E. DeZonia, Alison E. Walter, Ellen T. Arena, and Kevin W. Eliceiri. 2017. "ImageJ2: ImageJ for the next Generation of Scientific Image Data." *BMC Bioinformatics* 18 (1): 529.
Sakurai, J., N. Hattori, M. Nakajima, T. Moriya, T. Suzuki, A. Yokoyama, and N. Kohno. 2007. "Differential Expression of the Glycosylated Forms of MUC1 during Lung Development." *European Journal of Histochemistry: EJH* 51 (2): 95–102.
Scheele, Colinda L. G. J., Edouard Hannezo, Mauro J. Muraro, Anoek Zomer, Nathalia S. M. Langedijk, Alexander van Oudenaarden, Benjamin D. Simons, and Jacco van Rheenen. 2017. "Identity and Dynamics of Mammary Stem Cells during Branching

Morphogenesis." *Nature* 542 (7641): 313–17.
Shaner, Nathan C., Robert E. Campbell, Paul A. Steinbach, Ben N. G. Giepmans, Amy E. Palmer, and Roger Y. Tsien. 2004. "Improved Monomeric Red, Orange and Yellow Fluorescent Proteins Derived from Discosoma Sp. Red Fluorescent Protein." *Nature Biotechnology* 22 (12): 1567–72.
Shih, Hung Ping, Devin Panlasigui, Vincenzo Cirulli, and Maike Sander. 2016. "ECM Signaling Regulates Collective Cellular Dynamics to Control Pancreas Branching Morphogenesis." *Cell Reports* 14 (2): 169–79.
Shu, Xiaokun, Nathan C. Shaner, Corinne A. Yarbrough, Roger Y. Tsien, and S. James Remington. 2006. "Novel Chromophores and Buried Charges Control Color in mFruits." *Biochemistry* 45 (32): 9639–47.
Sievert, Carson. 2020. *Interactive Web-Based Data Visualization with R, Plotly, and Shiny*. CRC Press.
Sznurkowska, Magdalena K., Edouard Hannezo, Roberta Azzarelli, Steffen Rulands, Sonia Nestorowa, Christopher J. Hindley, Jennifer Nichols, et al. 2018. "Defining Lineage Potential and Fate Behavior of Precursors during Pancreas Development." *Developmental Cell* 46 (3): 360–75.e5.
The R core Team. 2021. *R: A Language and Environment for Statistical Computing*. https://www.R-project.org/.
Türkvatan, Aysel, Ayşe Erden, Mehmet Akif Türkoğlu, and Özlem Yener. 2013. "Congenital Variants and Anomalies of the Pancreas and Pancreatic Duct: Imaging by Magnetic Resonance Cholangiopancreaticography and Multidetector Computed Tomography." *Korean Journal of Radiology: Official Journal of the Korean Radiological Society* 14 (6): 905–13.
Varner, Victor D., and Celeste M. Nelson. 2014. "Cellular and Physical Mechanisms of Branching Morphogenesis." *Development* 141 (14): 2750–59.
Villasenor, Alethia, Diana C. Chong, Mark Henkemeyer, and Ondine Cleaver. 2010. "Epithelial Dynamics of Pancreatic Branching Morphogenesis." *Development* 137 (24): 4295–4305.
Walma, David A. Cruz, and Kenneth M. Yamada. 2020. "The Extracellular Matrix in Development." *Development* 147 (10). https://doi.org/10.1242/dev.175596.
Wang, Shaohe, Rei Sekiguchi, William P. Daley, and Kenneth M. Yamada. 2017. "Patterned Cell and Matrix Dynamics in Branching Morphogenesis." *The Journal of Cell Biology* 216 (3): 559–70.
Warming, Søren, Nina Costantino, Donald L. Court, Nancy A. Jenkins, and Neal G. Copeland. 2005. "Simple and Highly Efficient BAC Recombineering Using galK Selection." *Nucleic Acids Research* 33 (4): e36.
Wickham, Hadley, Mara Averick, Jennifer Bryan, Winston Chang, Lucy McGowan, Romain François, Garrett Grolemund, et al. 2019. "Welcome to the Tidyverse." *Journal of Open Source Software* 4 (43): 1686.
Zhou, Qiao, Anica C. Law, Jayaraj Rajagopal, William J. Anderson, Paul A. Gray, and Douglas A. Melton. 2007. "A Multipotent Progenitor Domain Guides Pancreatic Organogenesis." *Developmental Cell* 13 (1): 103–14.

Fig 1 Generation of a novel apical protein reporter mouse for 4D live imaging.

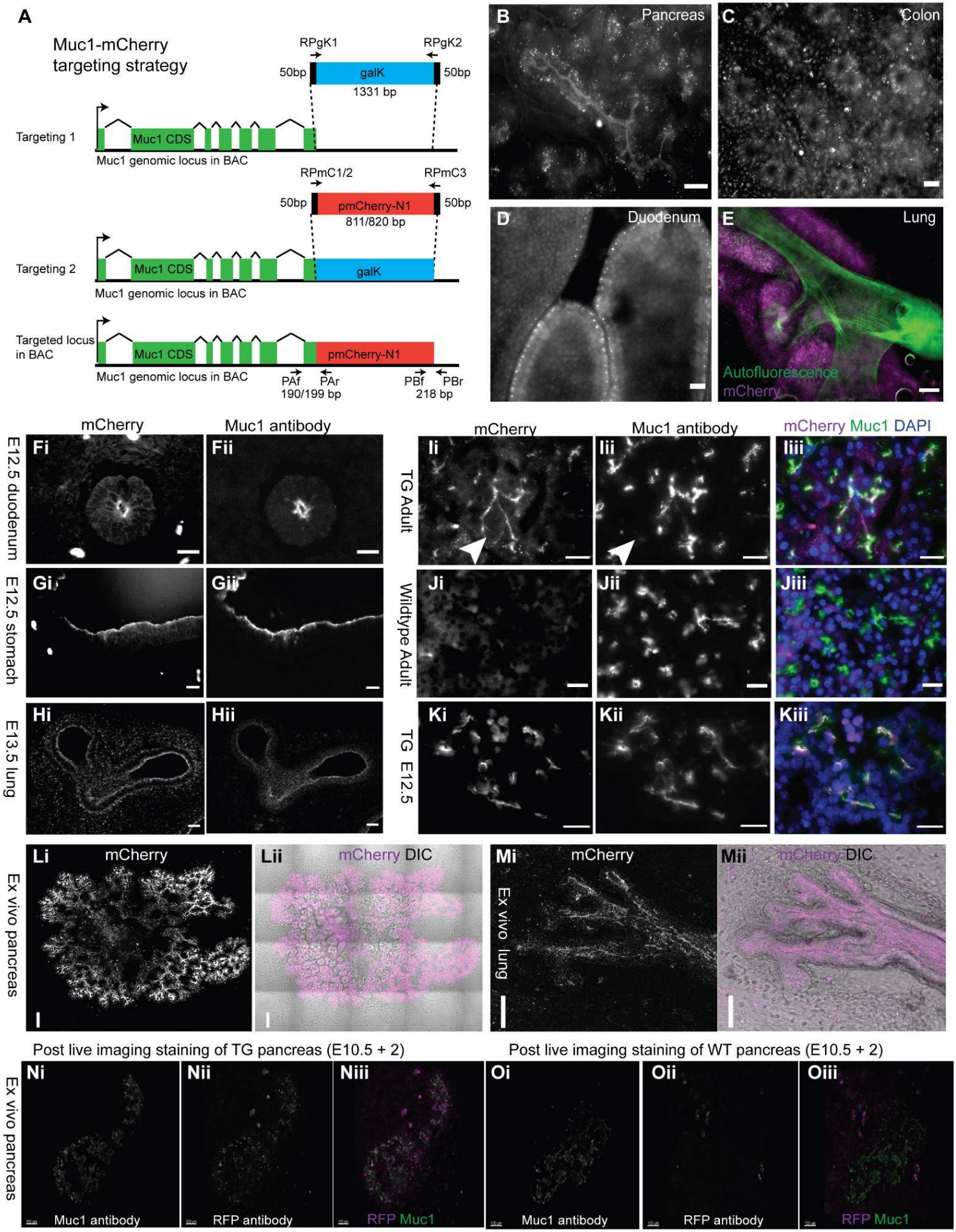

Fig 2: Lumenal network transformation is comparable in vivo and ex vivo.

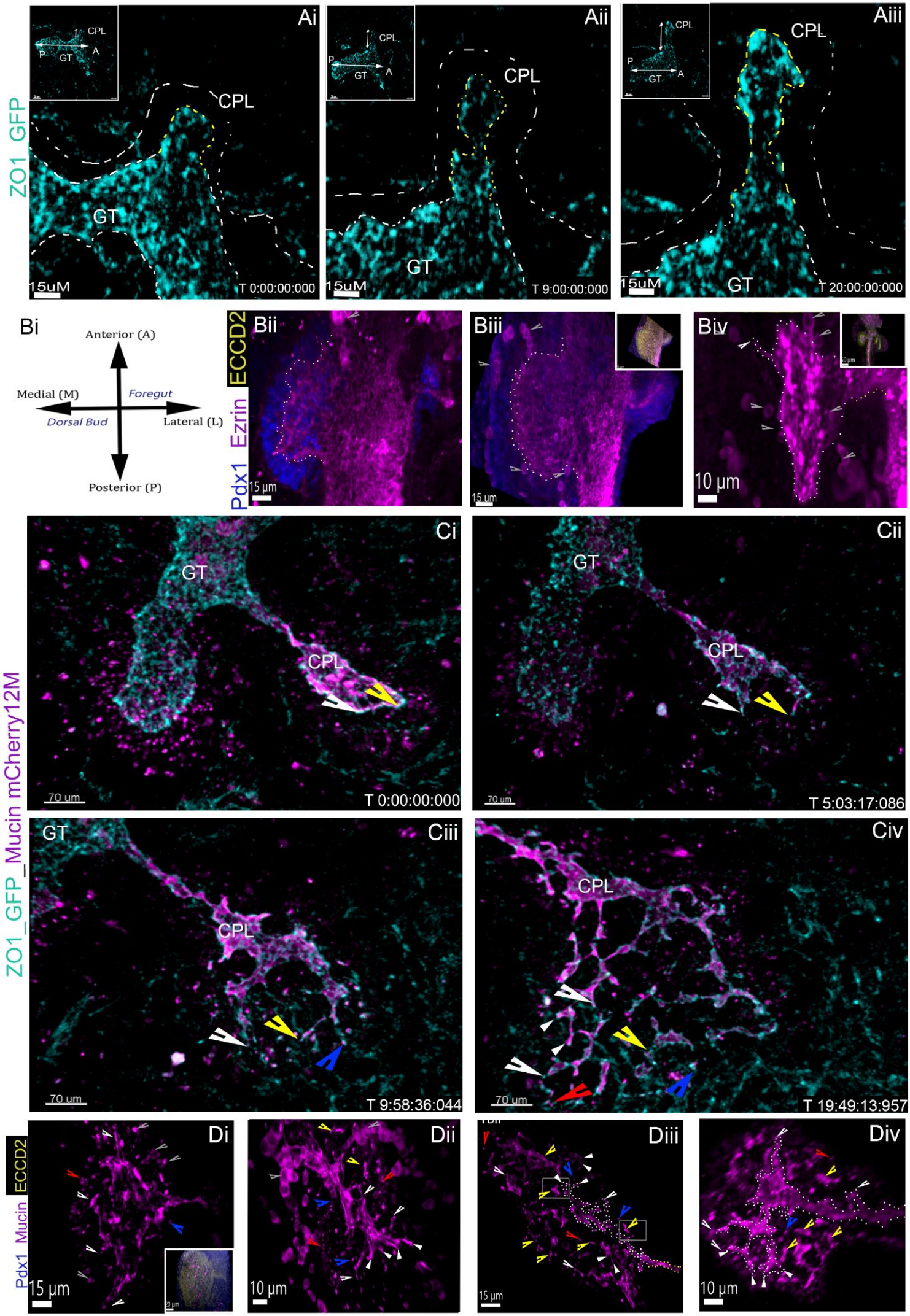

Fig 3 The pancreatic ductal network is largely derived from the central primary lumen through expansion and rearrangement of apical membranes

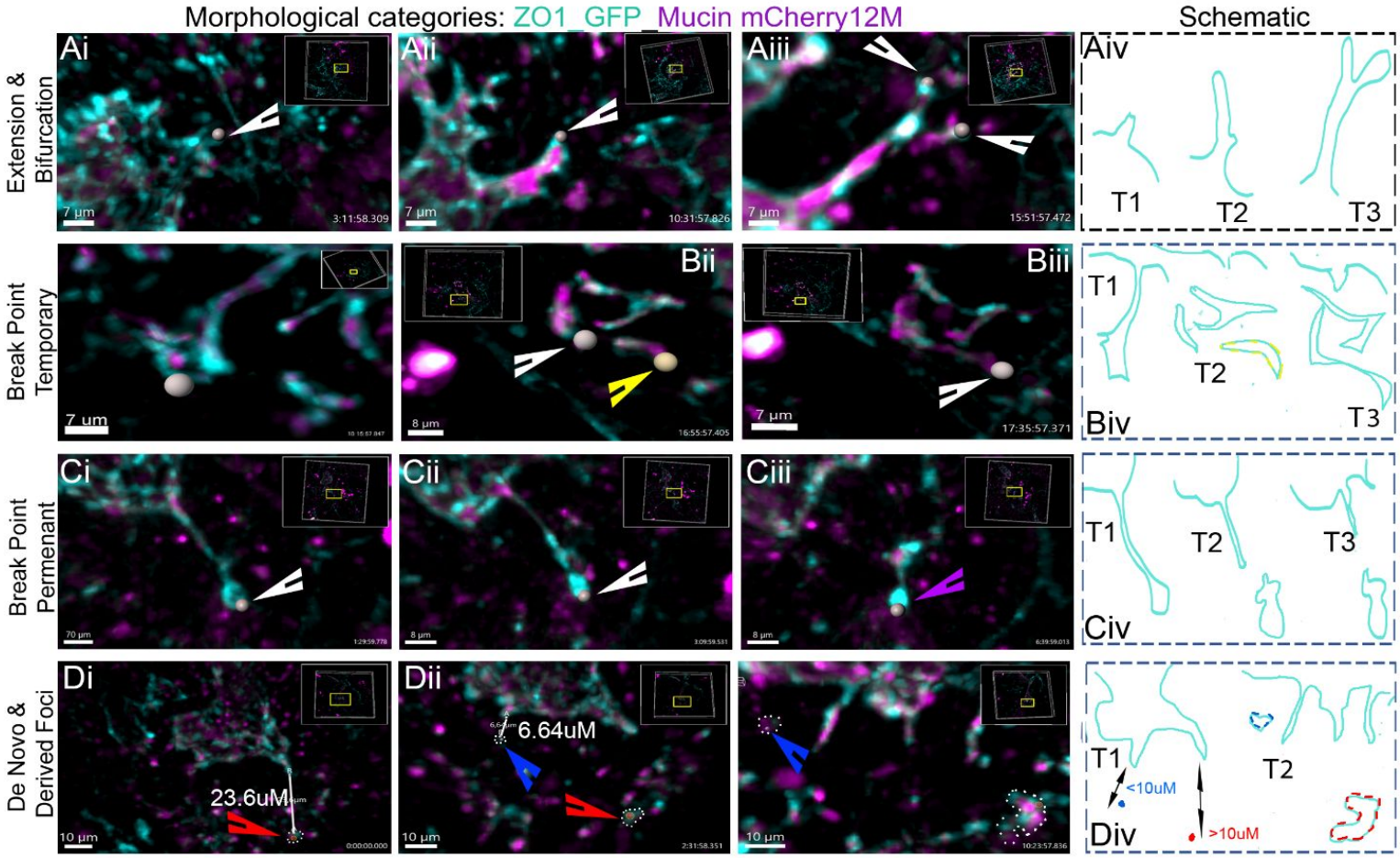

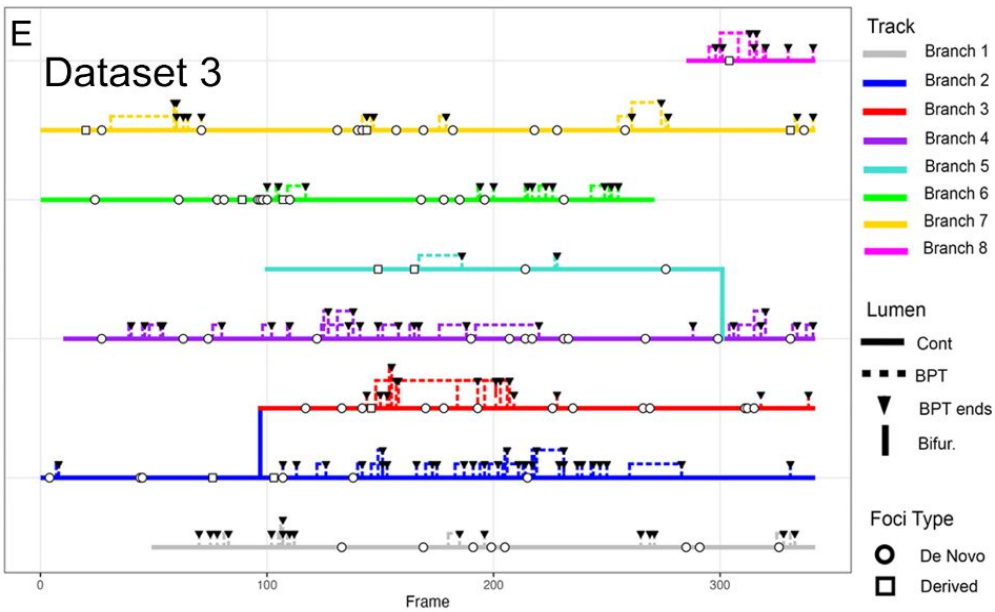

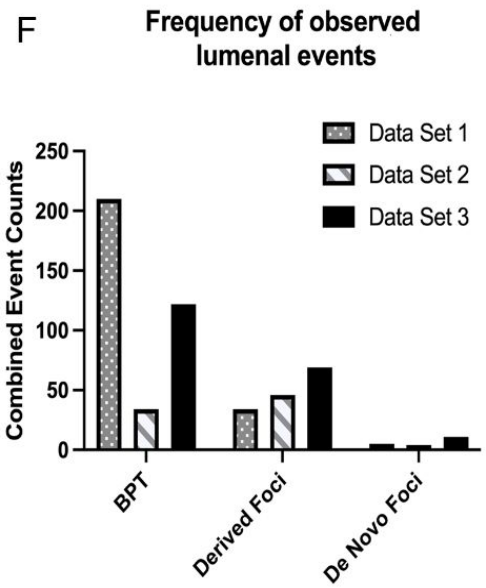

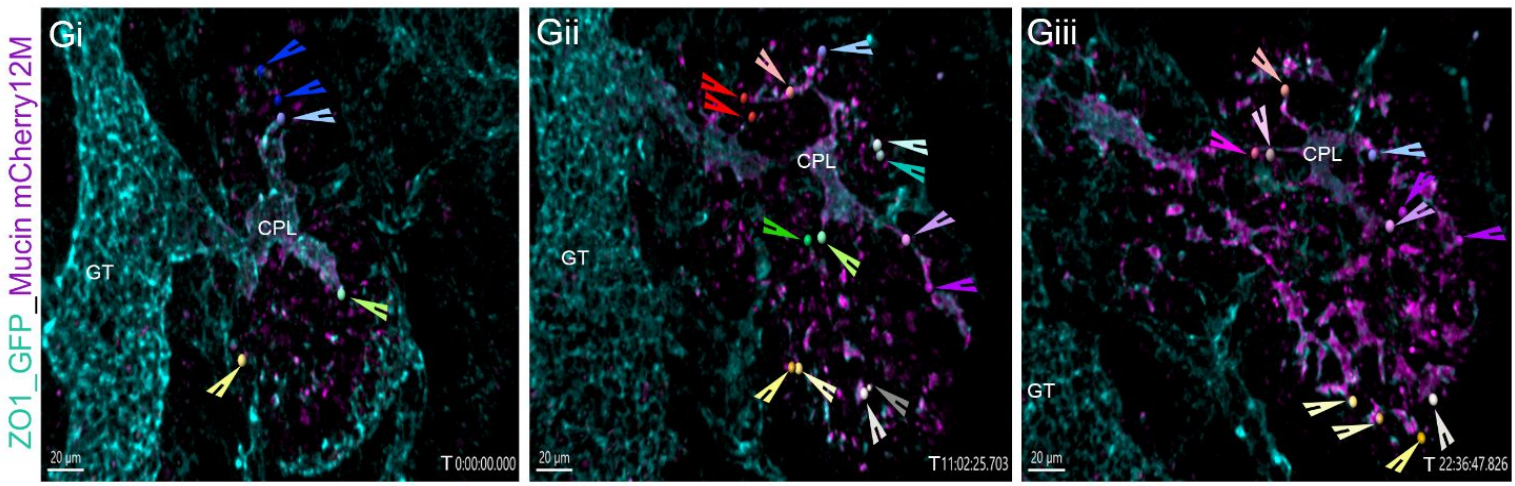

Fig 4: Characterization of loops

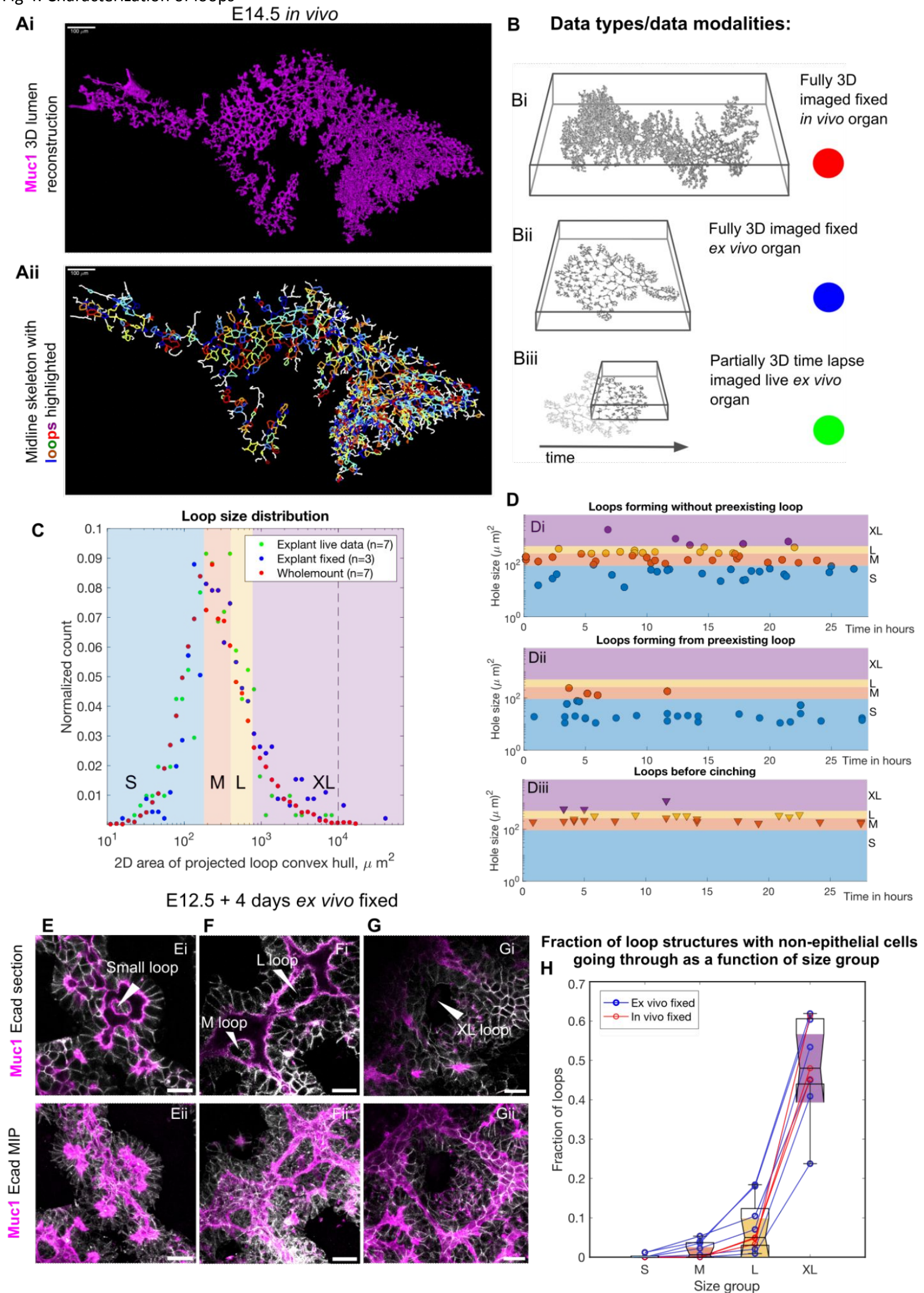

Fig.5 Tracking of Luminal structures

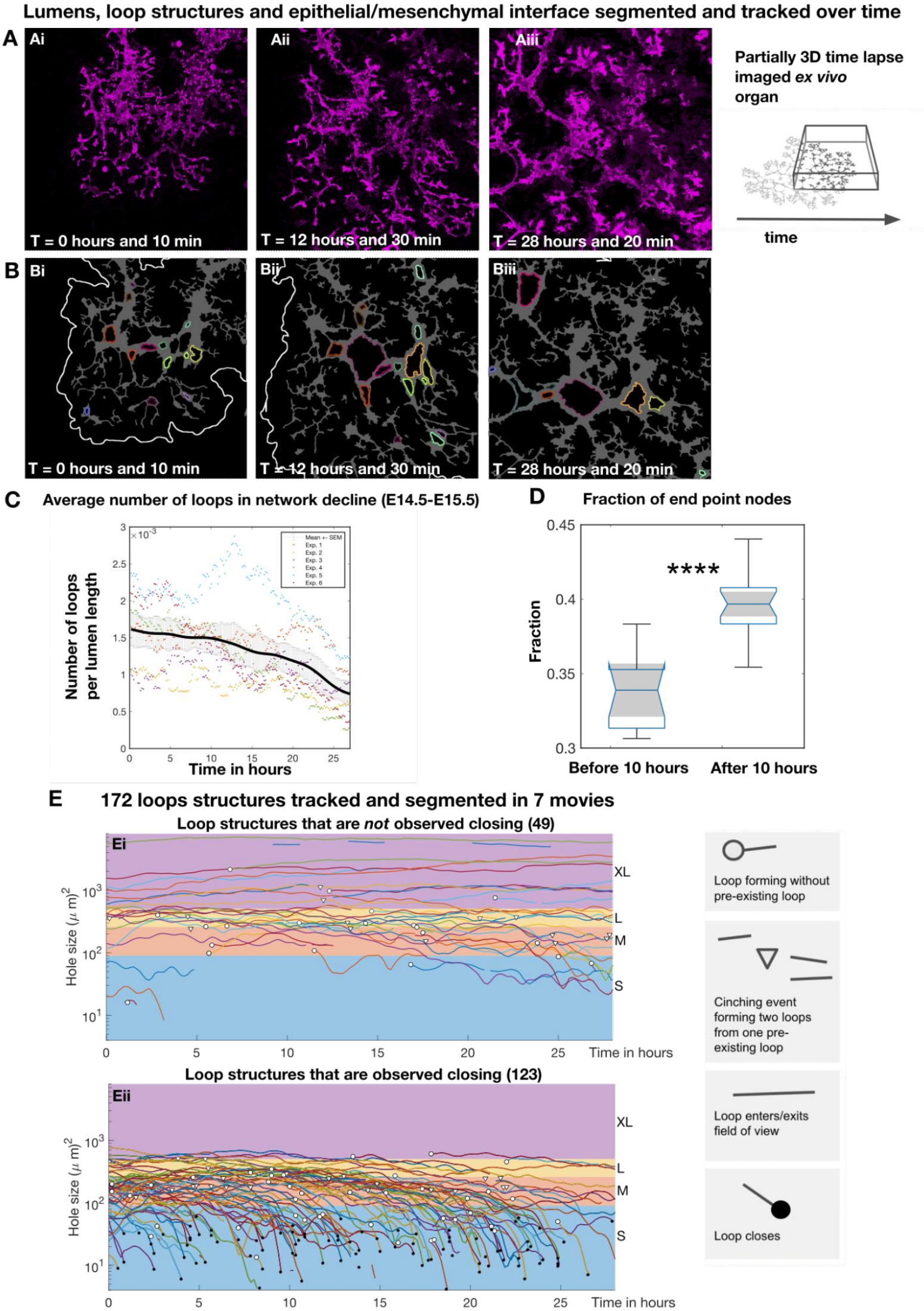

Fig.6. Loops structures dynamically change size and often contract and close.

A Example of a branch with 8 different loops forming, contracting, and closing

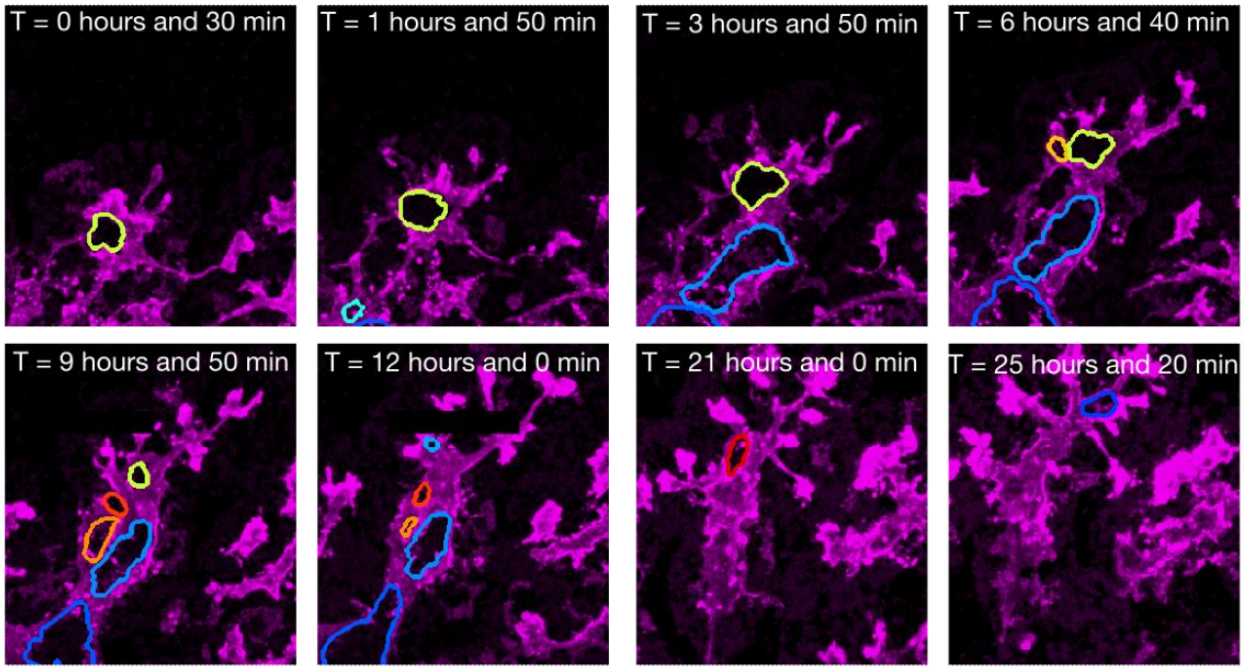

Partially 3D time lapse imaged *ex vivo* organ

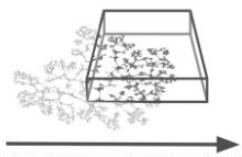

B Example of a gradually constricting loop structure that ends up closing:

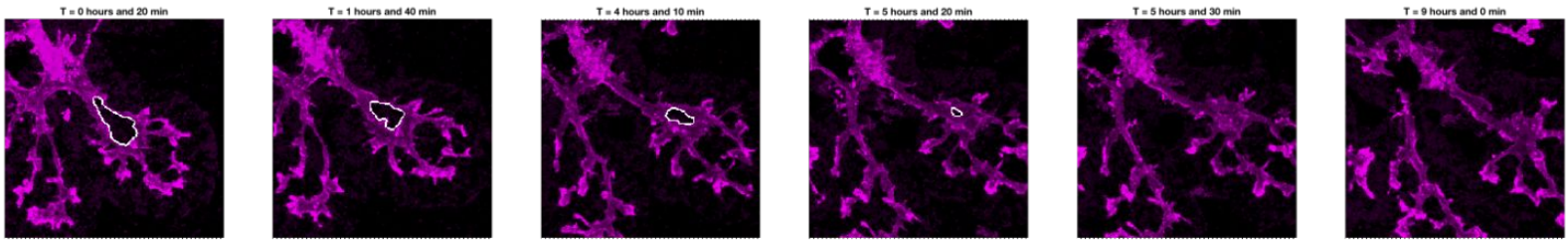

C Example of a loop breaking event:

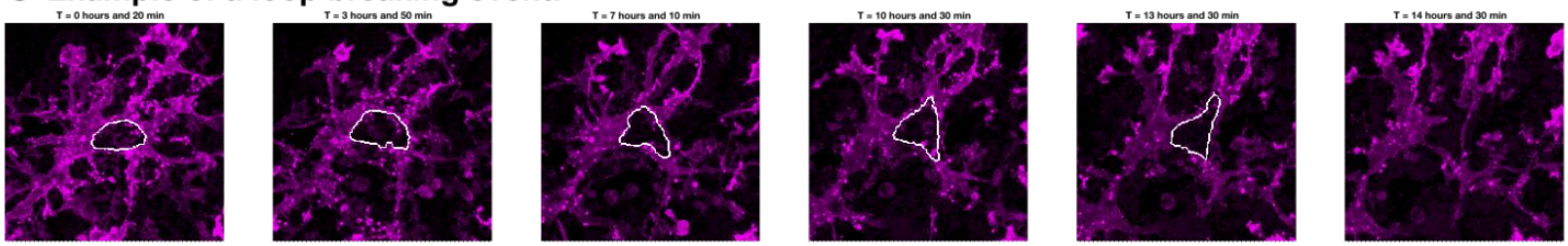

D Example of a loop 'cinching' event':

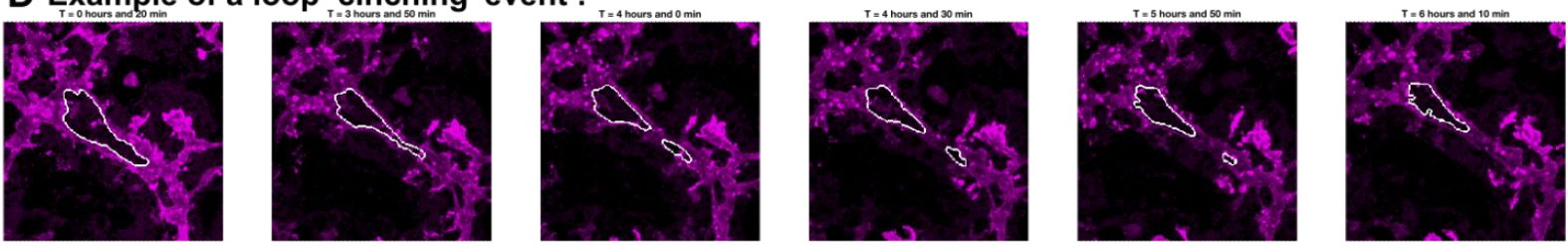

E Plexus resolves via loop closing, not lumen breaking

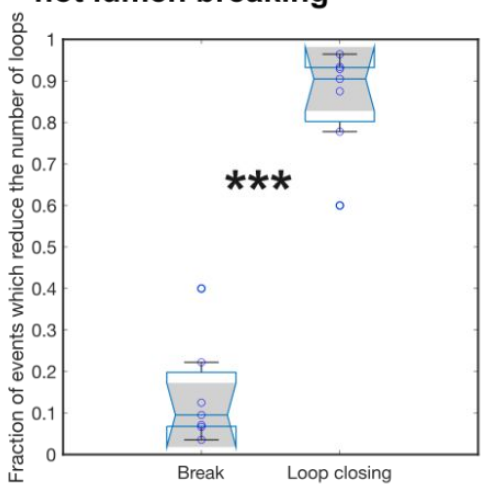

F Two types of loop closure dynamics

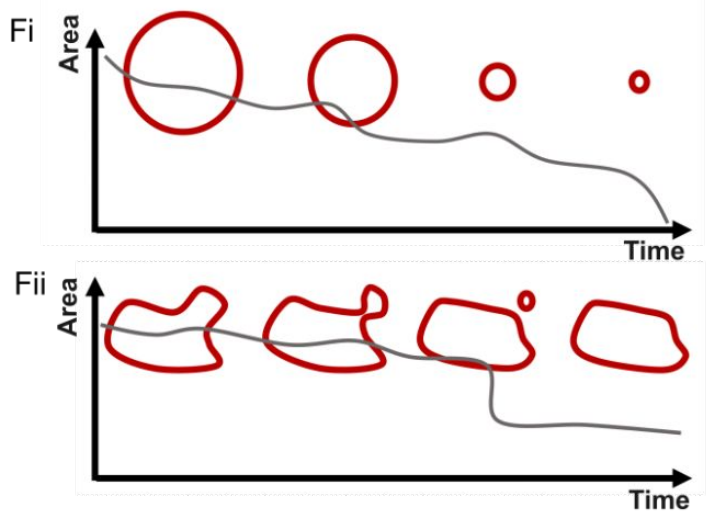

Fig 7: Static loop features associated with short term and long term dynamics (loop constriction and closure)

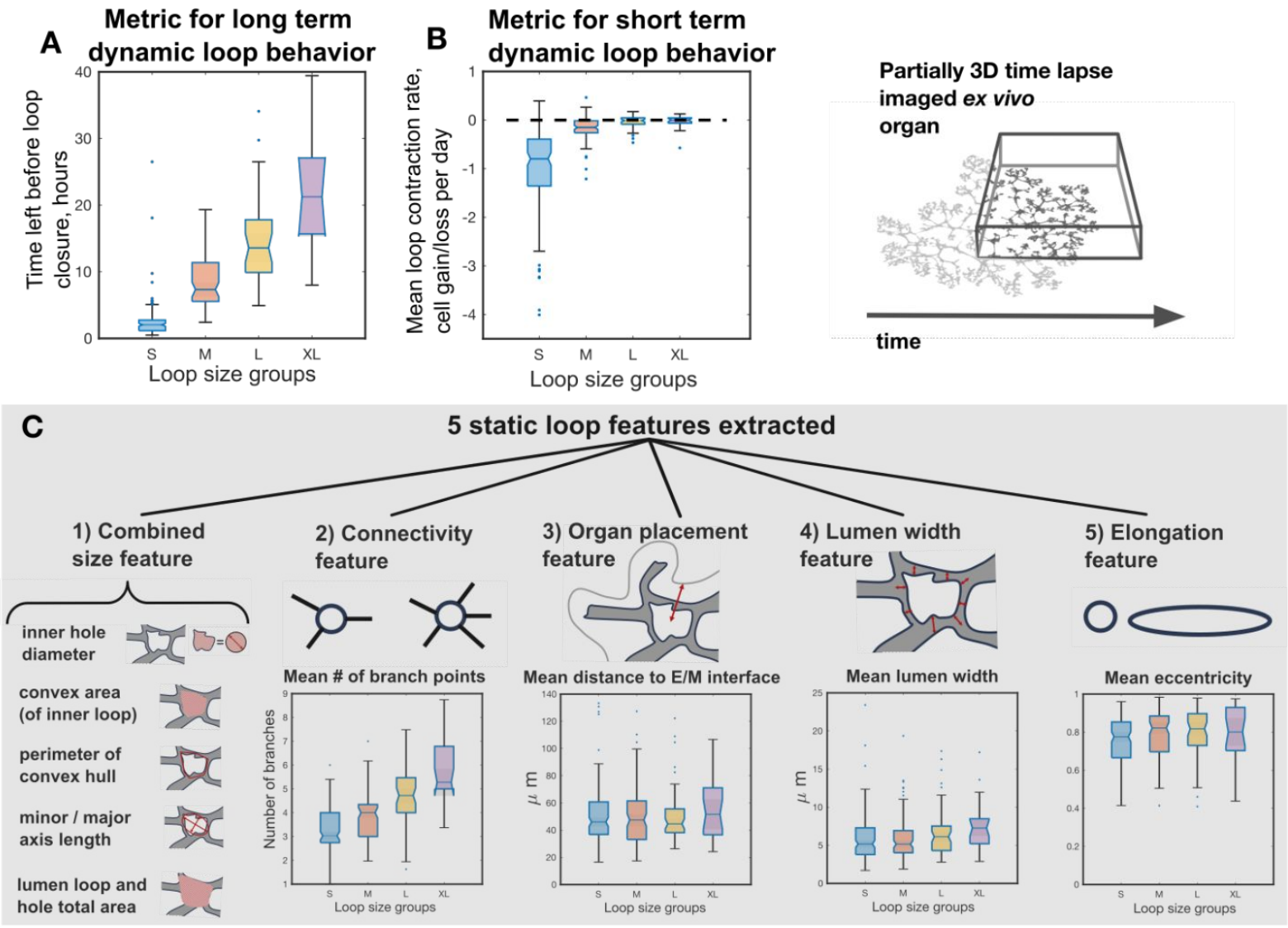

Long term, but not short term, loop dynamic behavior can be predicted from the extracted 5 static features

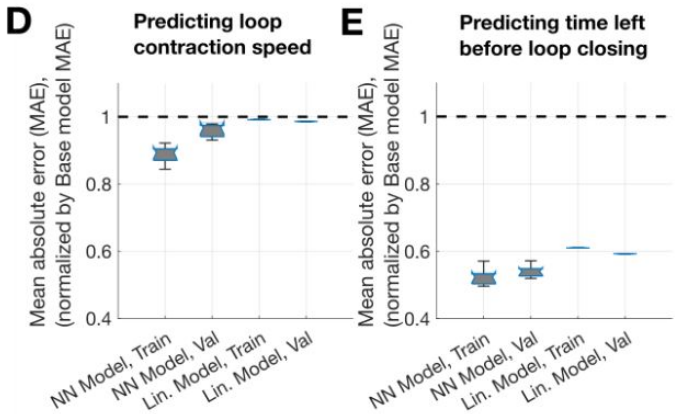

Feature 2. Connectivity feature

A positive change in the number of branch points is associated with a positive change in time left in all size groups

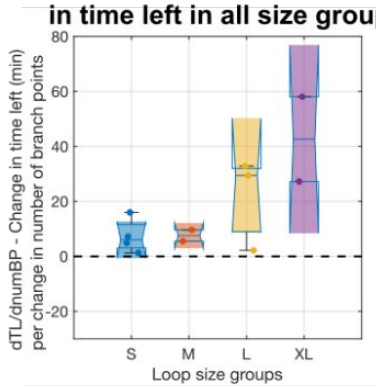

Feature 5. Elongation feature

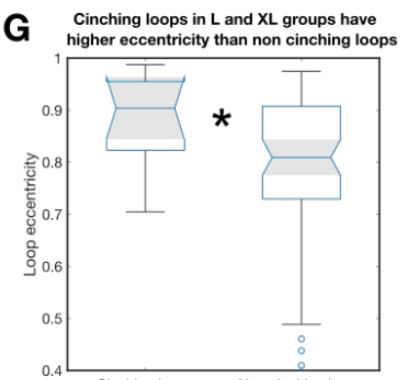

Feature 3. Organ placement feature

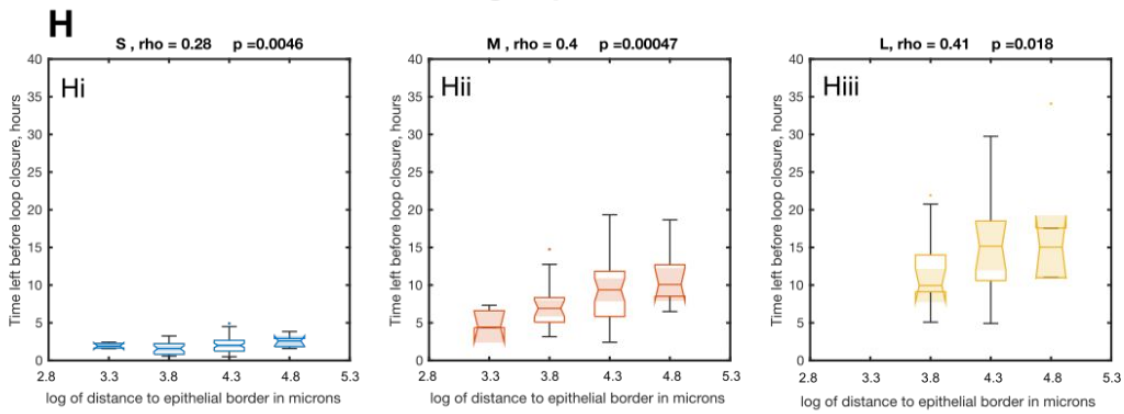

Fig 8: Comparative analysis of the inner luminal network and the outer epithelial branching

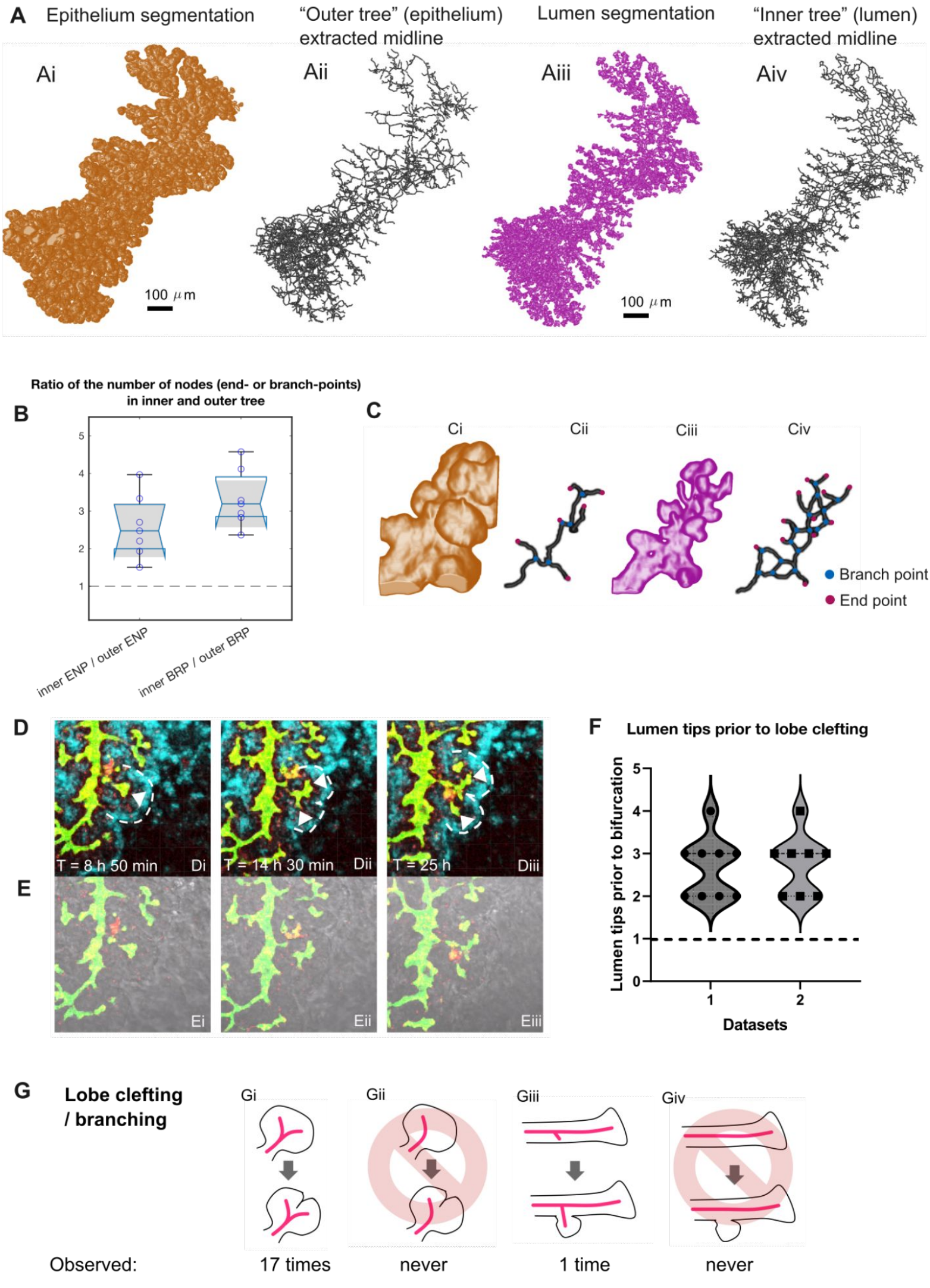

Supplementary material figures

S Fig 1.

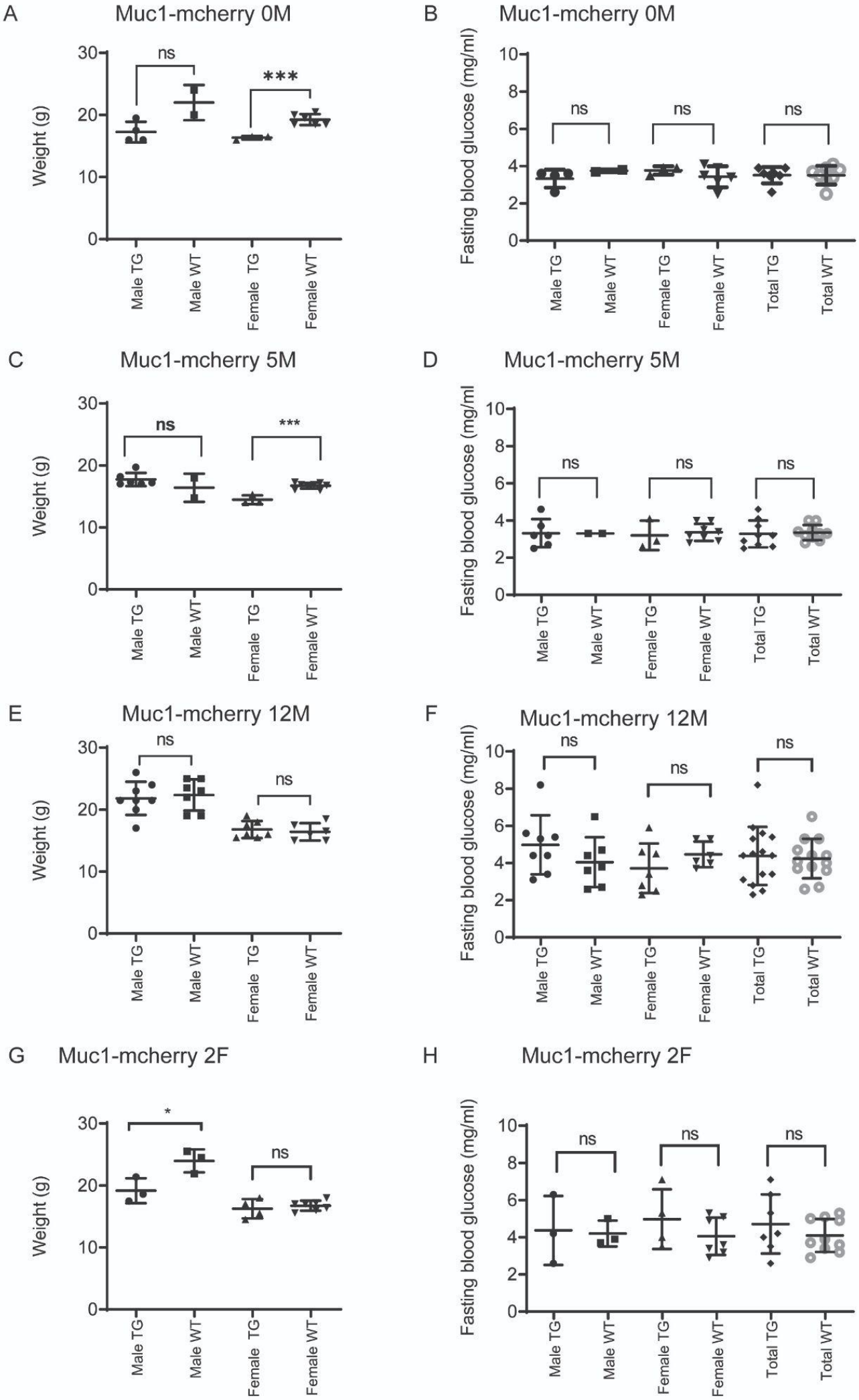
A
Muc1-mcherry 0M
Weight (g)
ns
***
Male TG
Male WT
Female TG
Female WT
B
Muc1-mcherry 0M
Fasting blood glucose (mg/ml)
ns
ns
ns
Male TG
Male WT
Female TG
Female WT
Total TG
Total WT
C
Muc1-mcherry 5M
Weight (g)
ns
***
D
Muc1-mcherry 5M
Fasting blood glucose (mg/ml
ns
ns
ns
E
Muc1-mcherry 12M
Weight (g)
ns
ns
F
Muc1-mcherry 12M
Fasting blood glucose (mg/ml)
ns
ns
ns
G
Muc1-mcherry 2F
Weight (g)
*
ns
H
Muc1-mcherry 2F
Fasting blood glucose (mg/ml)
ns
ns
ns

S Fig 2.

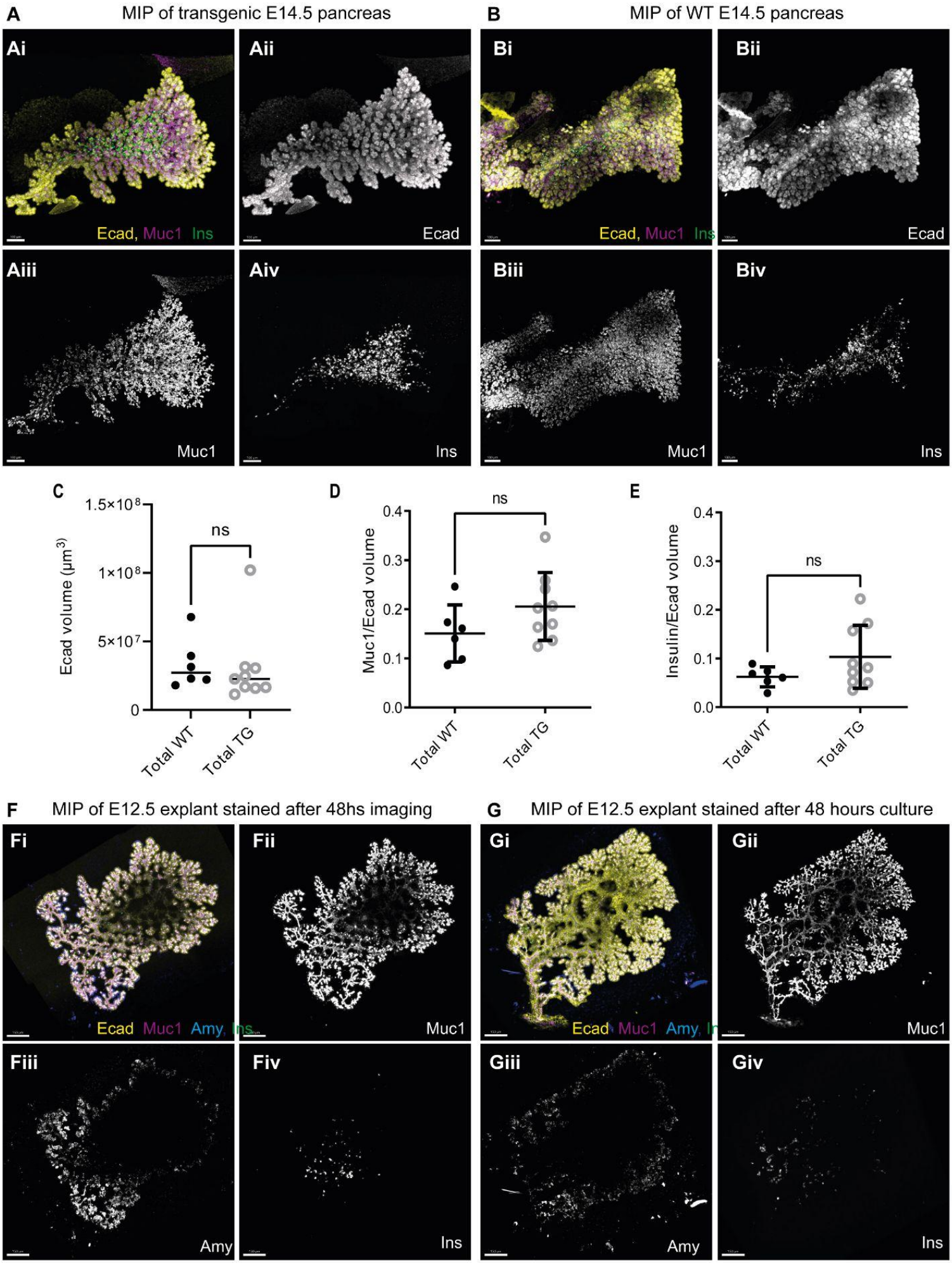
A
MIP of transgenic E14.5 pancreas
B
MIP of WT E14.5 pancreas
Ai
Ecad, Muc1 Ins
Aii
Ecad
Aiii
Muc1
Aiv
Ins
Bi
Ecad, Muc1 Ins
Bii
Ecad
Biii
Muc1
Biv
Ins
C
Ecad volume (µm³)
1.5×10⁸
1×10⁸
5×10⁷
0
ns
Total WT
Total TG
D
Muc1/Ecad volume
0.4
0.3
0.2
0.1
0.0
ns
Total WT
Total TG
E
Insulin/Ecad volume
0.4
0.3
0.2
0.1
0.0
ns
Total WT
Total TG
F
MIP of E12.5 explant stained after 48hs imaging
Fi
Ecad Muc1 Amy, Ins
Fii
Muc1
Fiii
Amy
Fiv
Ins
G
MIP of E12.5 explant stained after 48 hours culture
Gi
Ecad Muc1 Amy, In
Gii
Muc1
Giii
Amy
Giv
Ins

S Fig 3.Hierarchy of endogenous and reporter visualized Mucin expression comparative to ZO1-GFP expression in live and WMIF pancreatic foreguts.

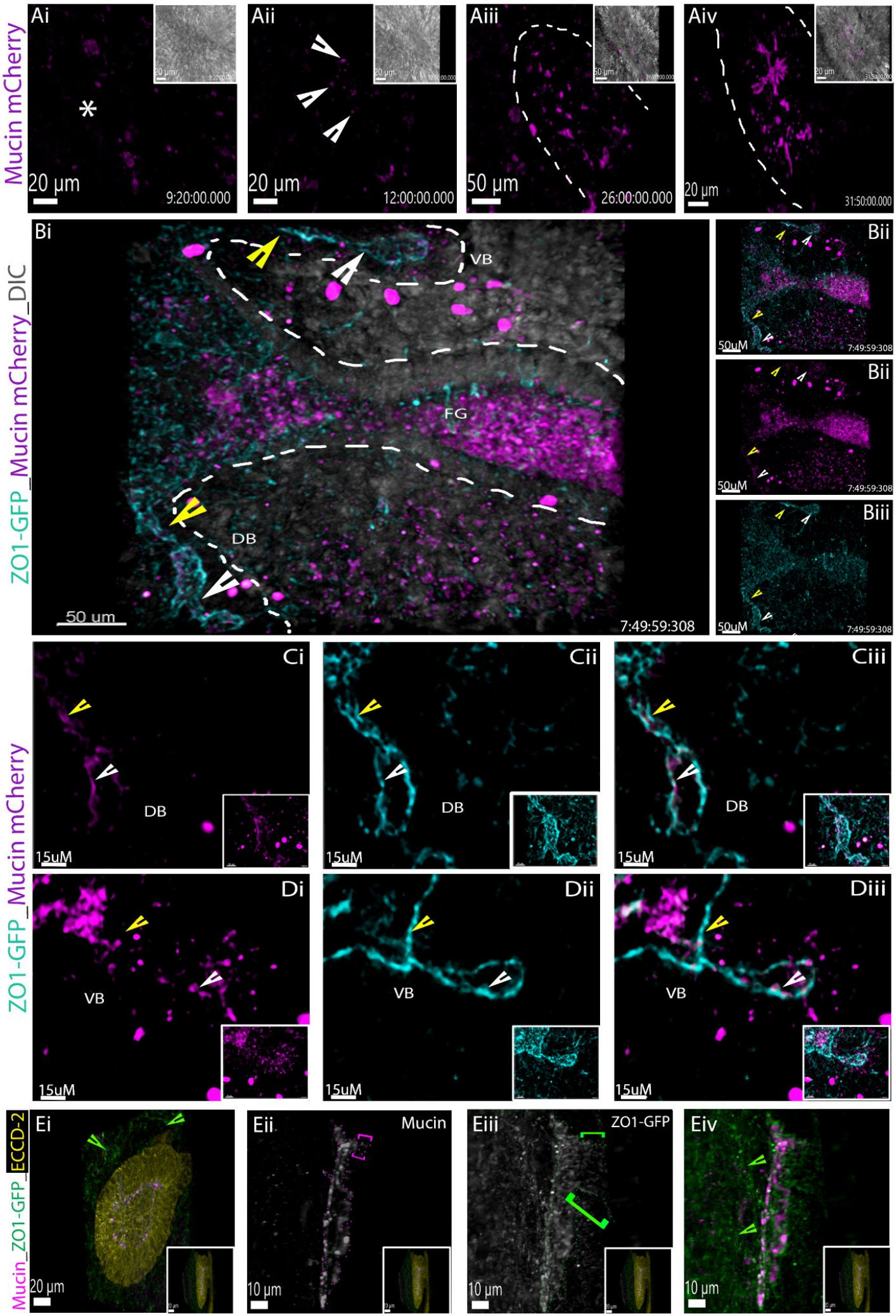

S Fig 4. WMIF of multiple apical proteins reveal consistent CPL transitions and variable luminal patency during secondary network establishment.

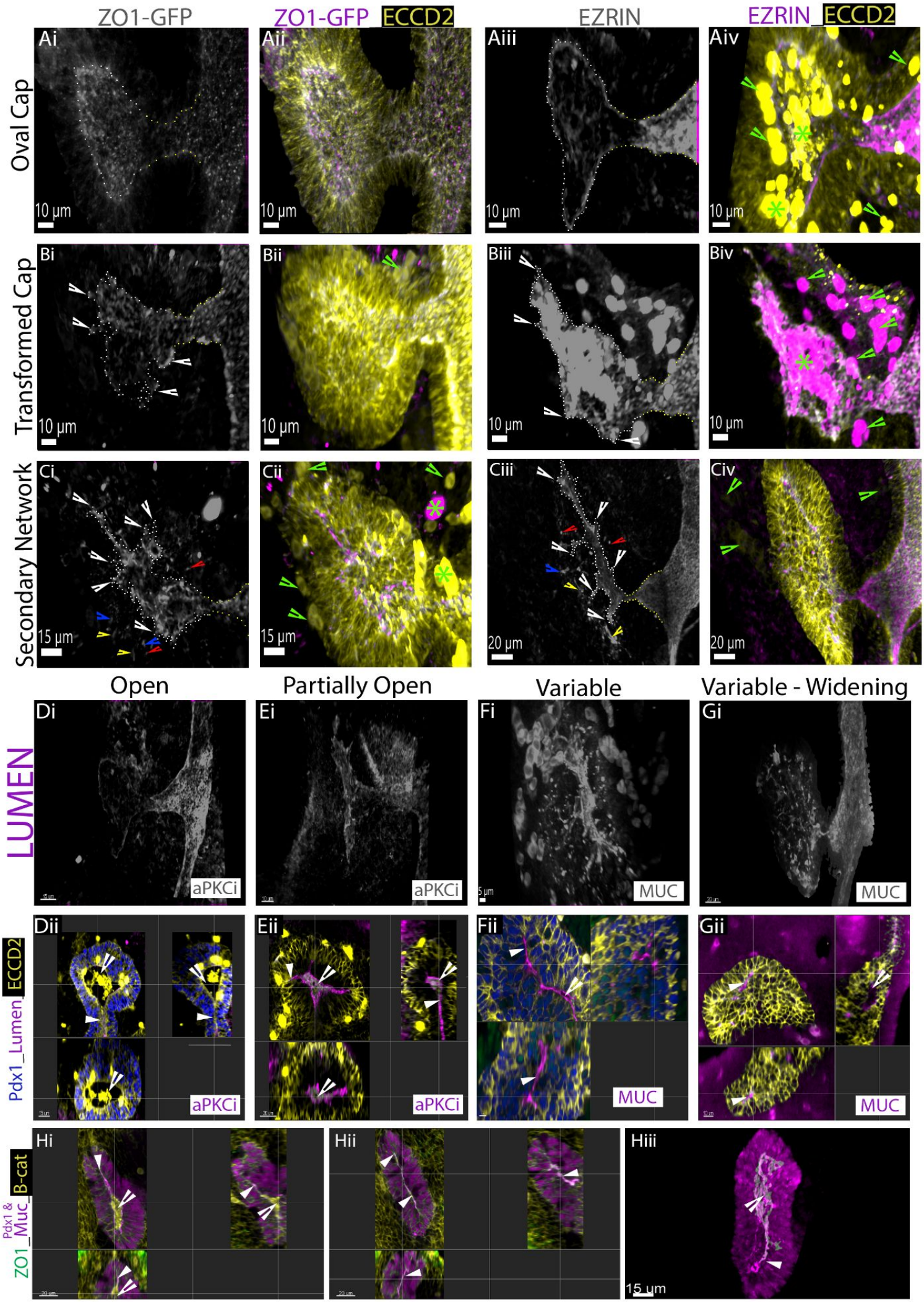

S Fig 5.Identifying endothelial expression of ZO1-GFP outside the pancreatic epithelium and estimating the average cell length of a pancreatic epithelial cell.

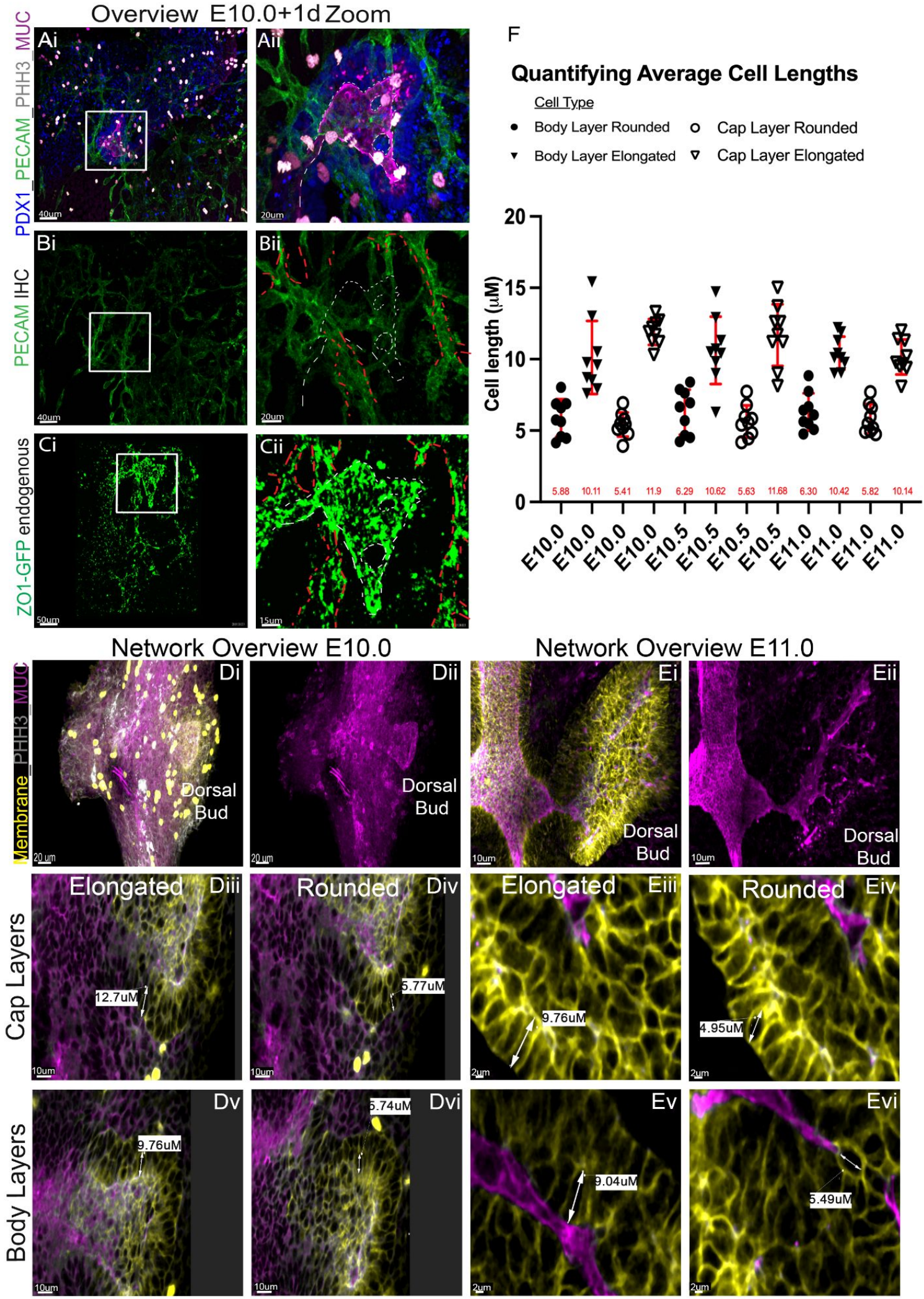

S Fig 6.Quantitative data to further support the conclusion that lumenal network is largely derived through expansion and rearrangement of apical membranes.

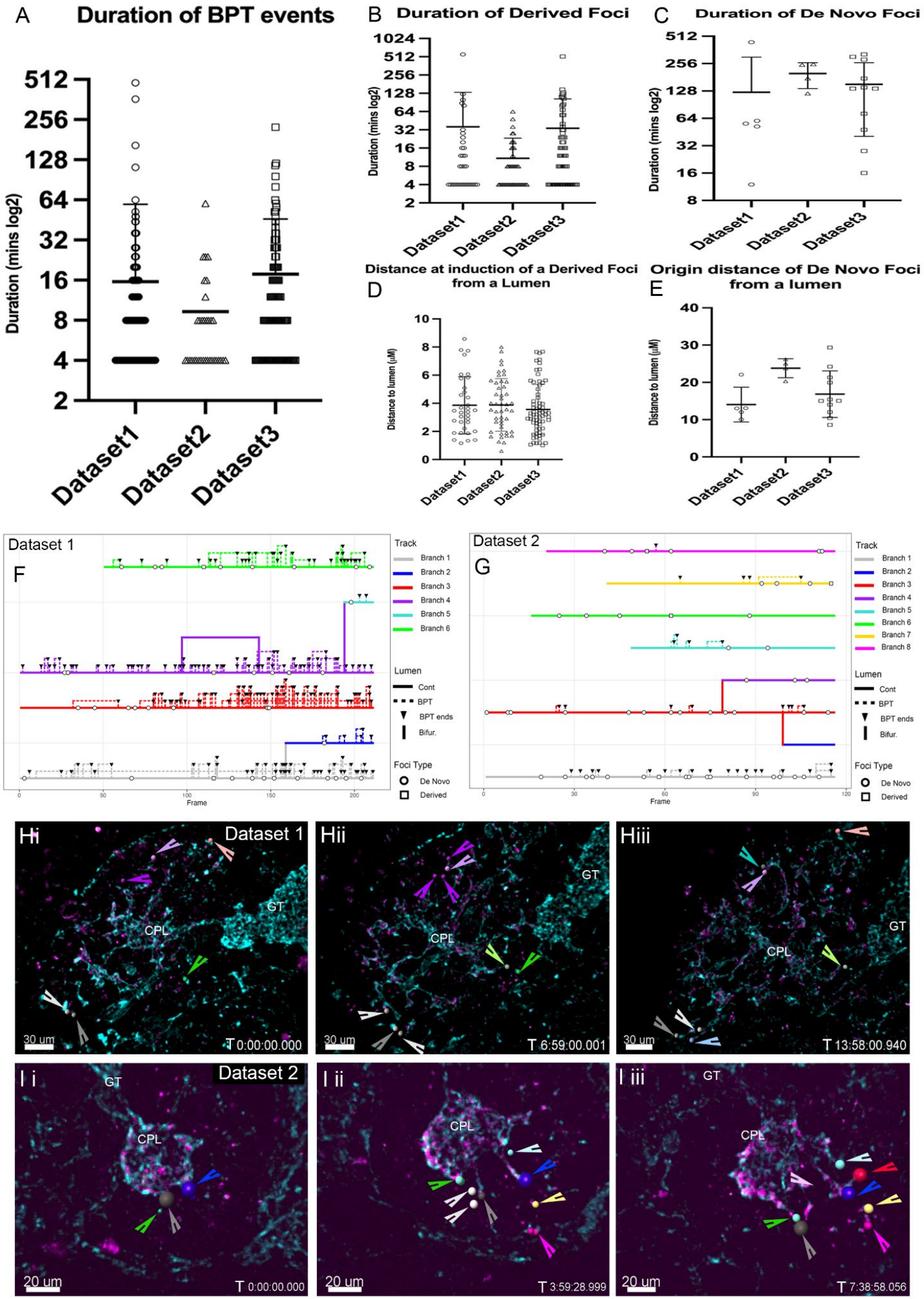

S Fig 7. Loop formation is a continuous feature through early and mid-gestation lumenal network transformations.

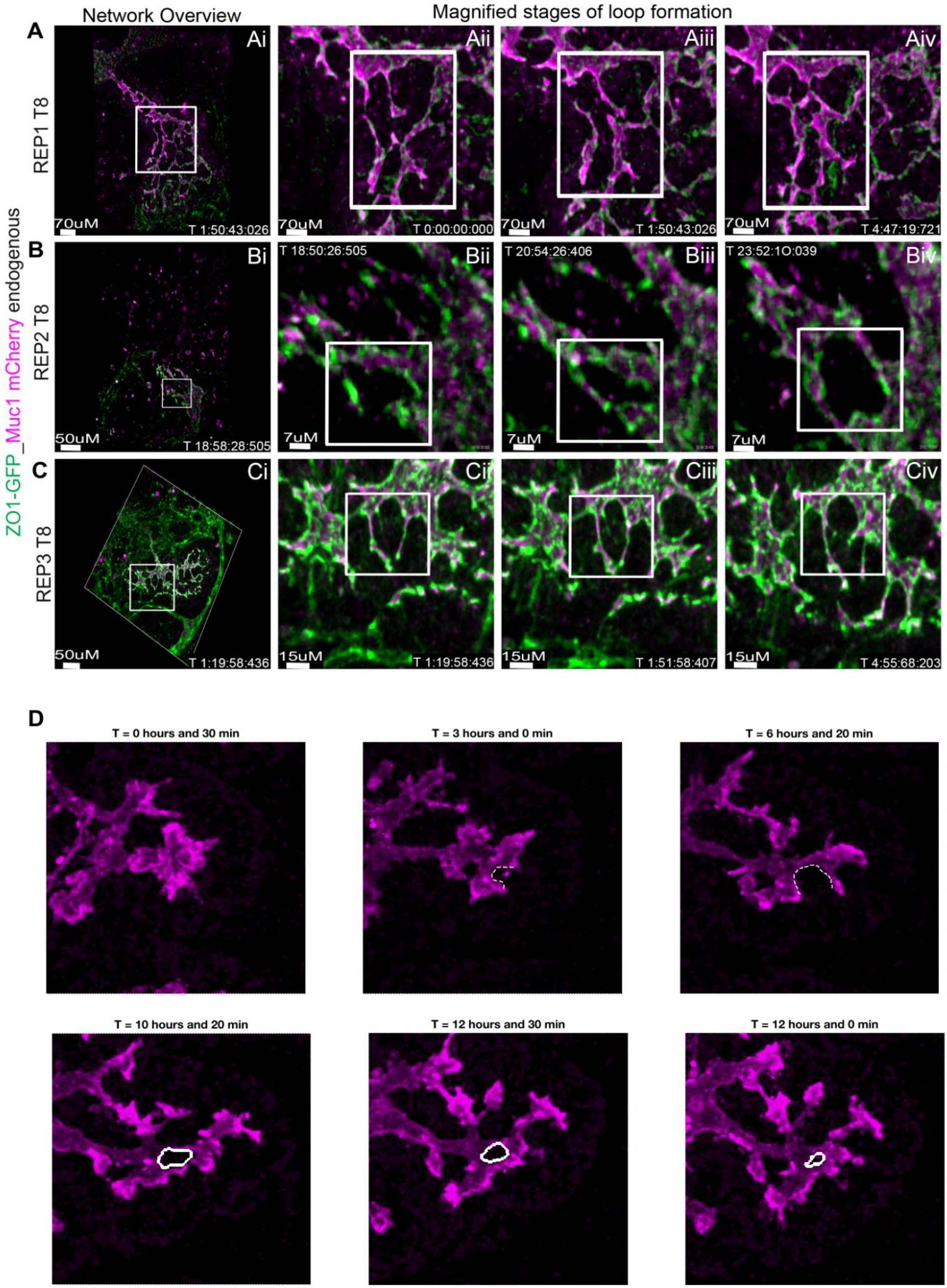

S Fig 8.

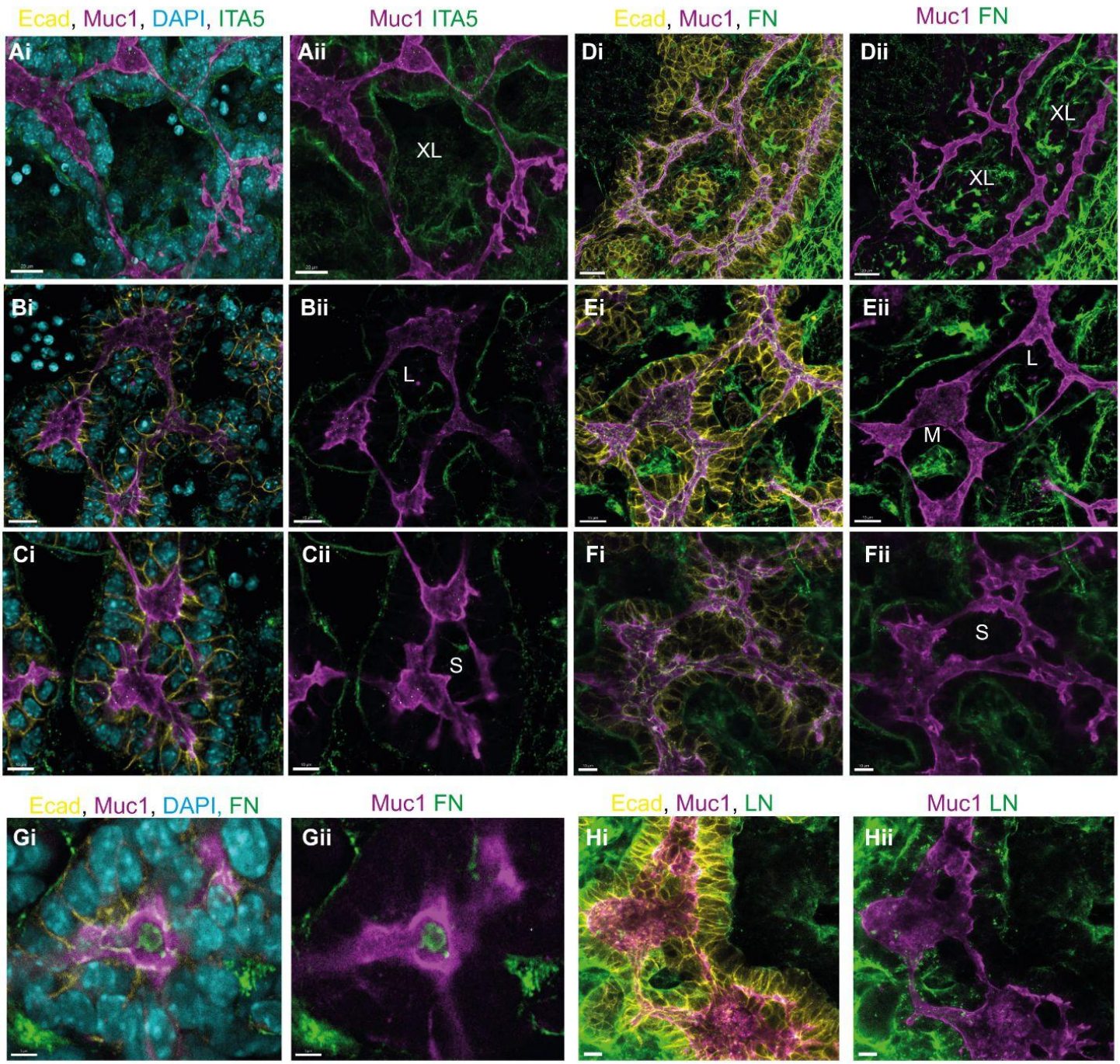
Ecad, Muc1, DAPI, ITA5
Muc1 ITA5
Ecad, Muc1, FN
Muc1 FN
Ai
Aii
XL
Di
Dii
XL
XL
Bi
Bii
L
Ei
Eii
L
M
Ci
Cii
S
Fi
Fii
S
Ecad, Muc1, DAPI, FN
Muc1 FN
Ecad, Muc1, LN
Muc1 LN
Gi
Gii
Hi
Hii

S Fig 9.

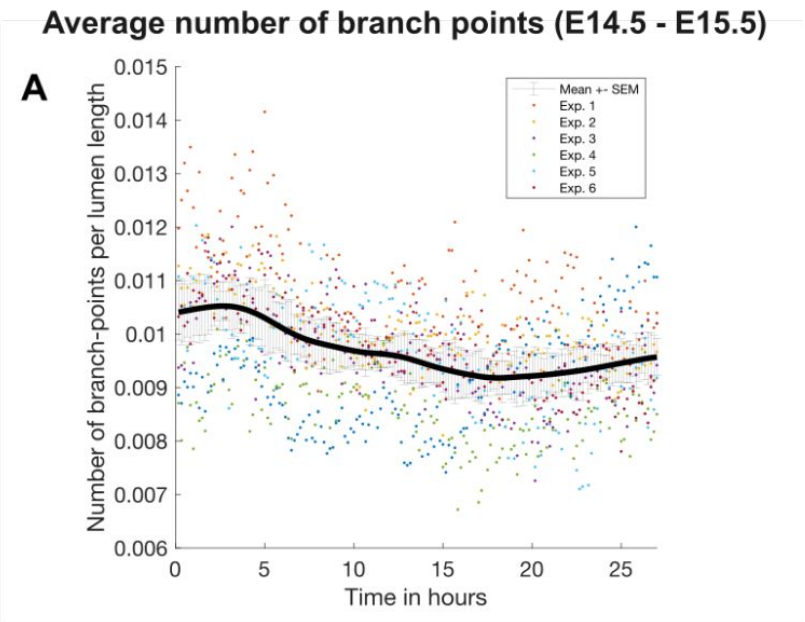
Average number of branch points (E14.5 - E15.5)
A
Number of branch-points per lumen length
Time in hours
Mean +- SEM
Exp. 1
Exp. 2
Exp. 3
Exp. 4
Exp. 5
Exp. 6

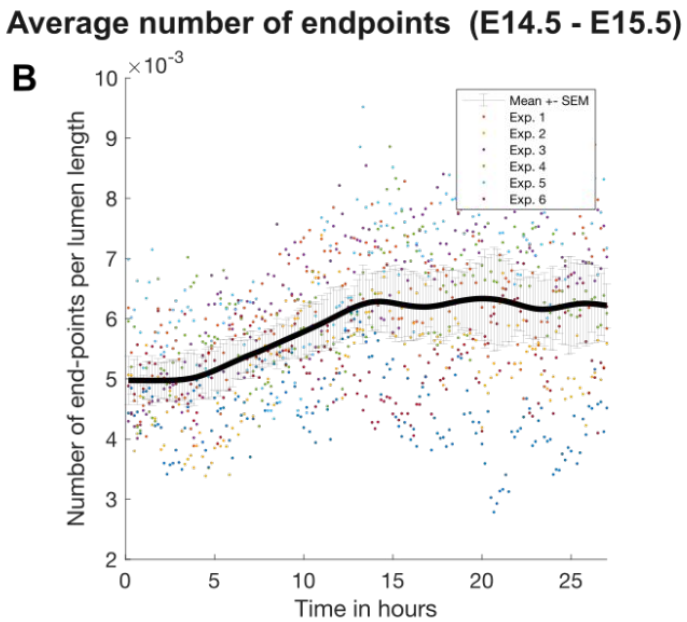
Average number of endpoints (E14.5 - E15.5)
B
Number of end-points per lumen length
Time in hours
Mean +- SEM
Exp. 1
Exp. 2
Exp. 3
Exp. 4
Exp. 5
Exp. 6

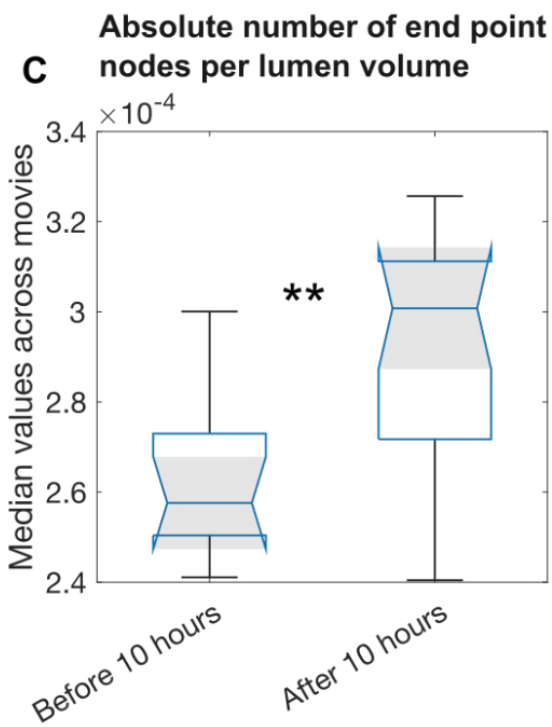
C
Absolute number of end point nodes per lumen volume
Median values across movies
**
Before 10 hours
After 10 hours

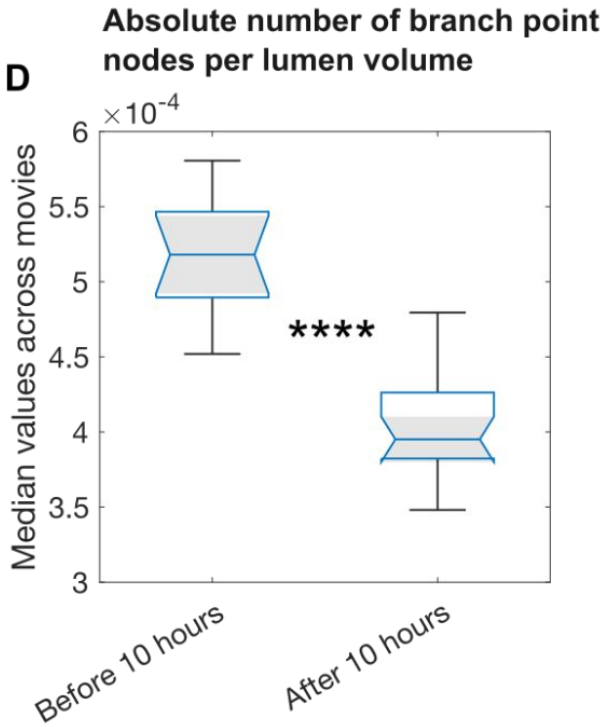
D
Absolute number of branch point nodes per lumen volume
Median values across movies
****
Before 10 hours
After 10 hours

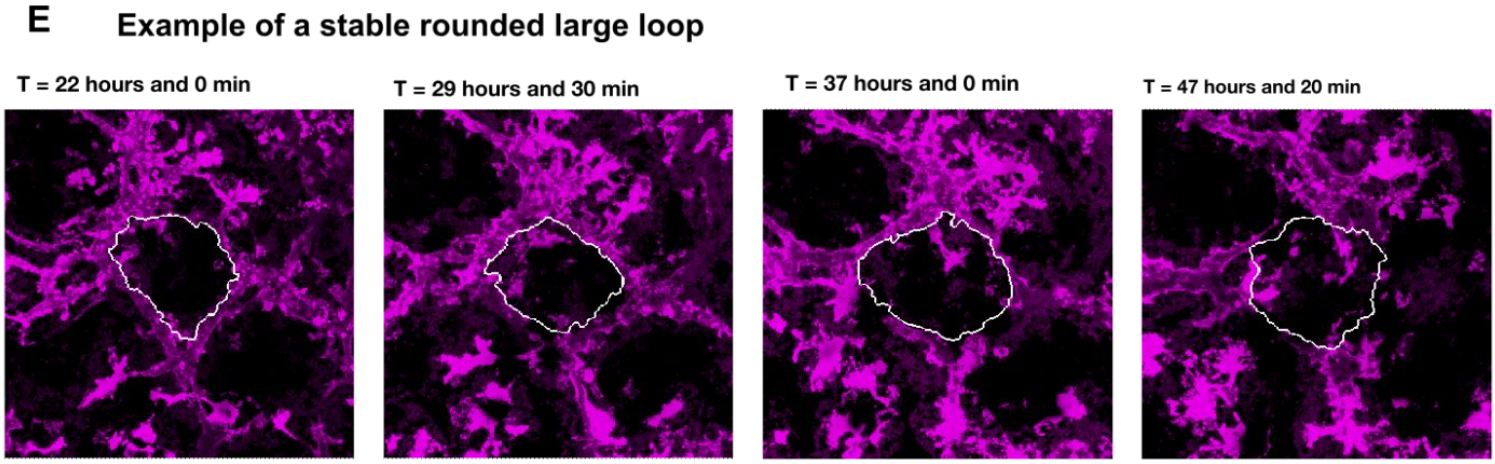
E
Example of a stable rounded large loop
T = 22 hours and 0 min
T = 29 hours and 30 min
T = 37 hours and 0 min
T = 47 hours and 20 min

S Fig 10

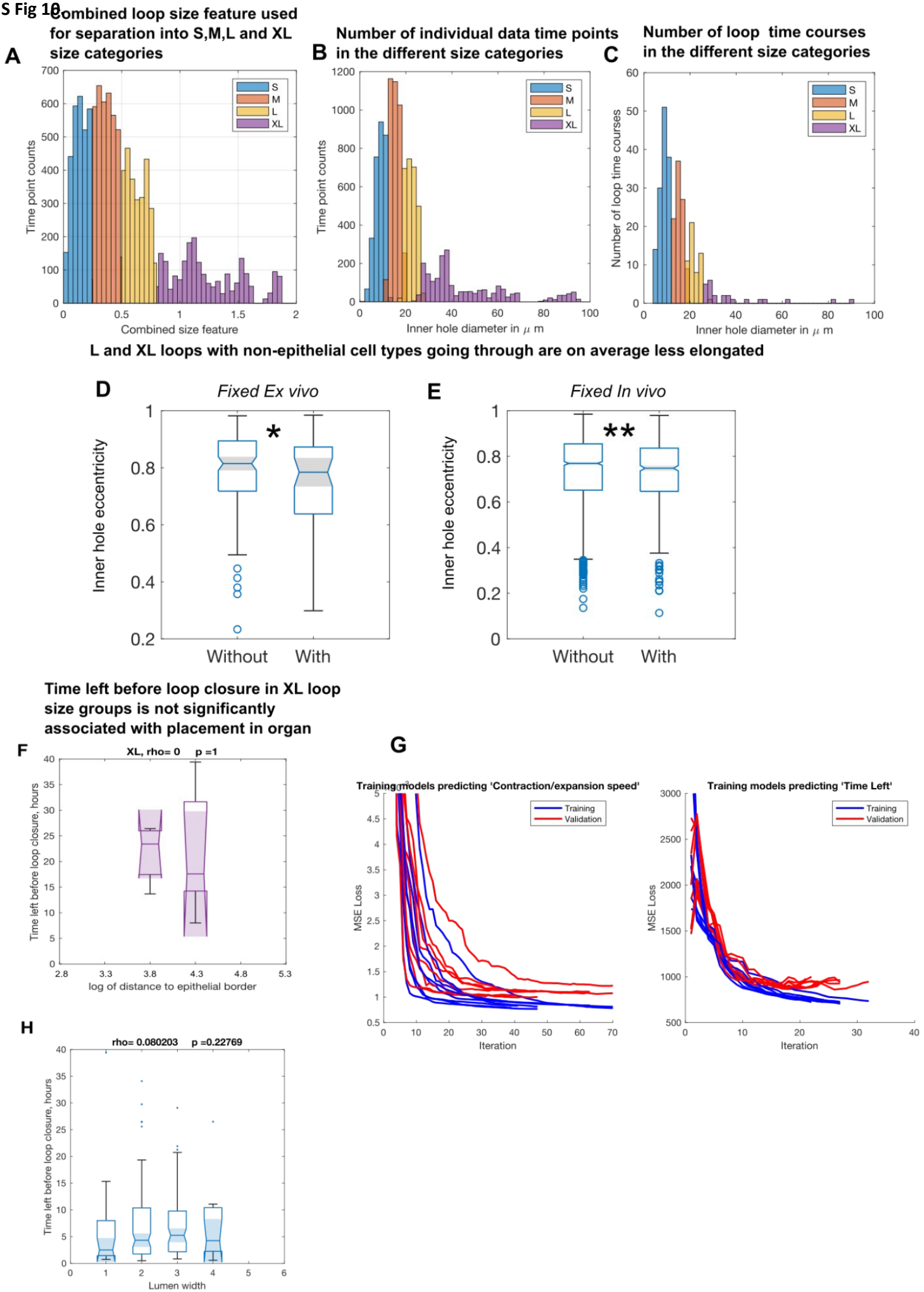
A
Combined loop size feature used for separation into S,M,L and XL size categories
Time point counts
Combined size feature
S
M
L
XL
B
Number of individual data time points in the different size categories
Time point counts
Inner hole diameter in μ m
C
Number of loop time courses in the different size categories
Number of loop time courses
Inner hole diameter in μ m
L and XL loops with non-epithelial cell types going through are on average less elongated
D
Fixed Ex vivo
Inner hole eccentricity
Without
With
E
Fixed In vivo
Inner hole eccentricity
Without
With
Time left before loop closure in XL loop size groups is not significantly associated with placement in organ
F
XL, rho= 0 p =1
Time left before loop closure, hours
log of distance to epithelial border
G
Training models predicting 'Contraction/expansion speed'
Training models predicting 'Time Left'
Training
Validation
MSE Loss
Iteration
H
rho= 0.080203 p =0.22769
Time left before loop closure, hours
Lumen width

S Fig 11.

A

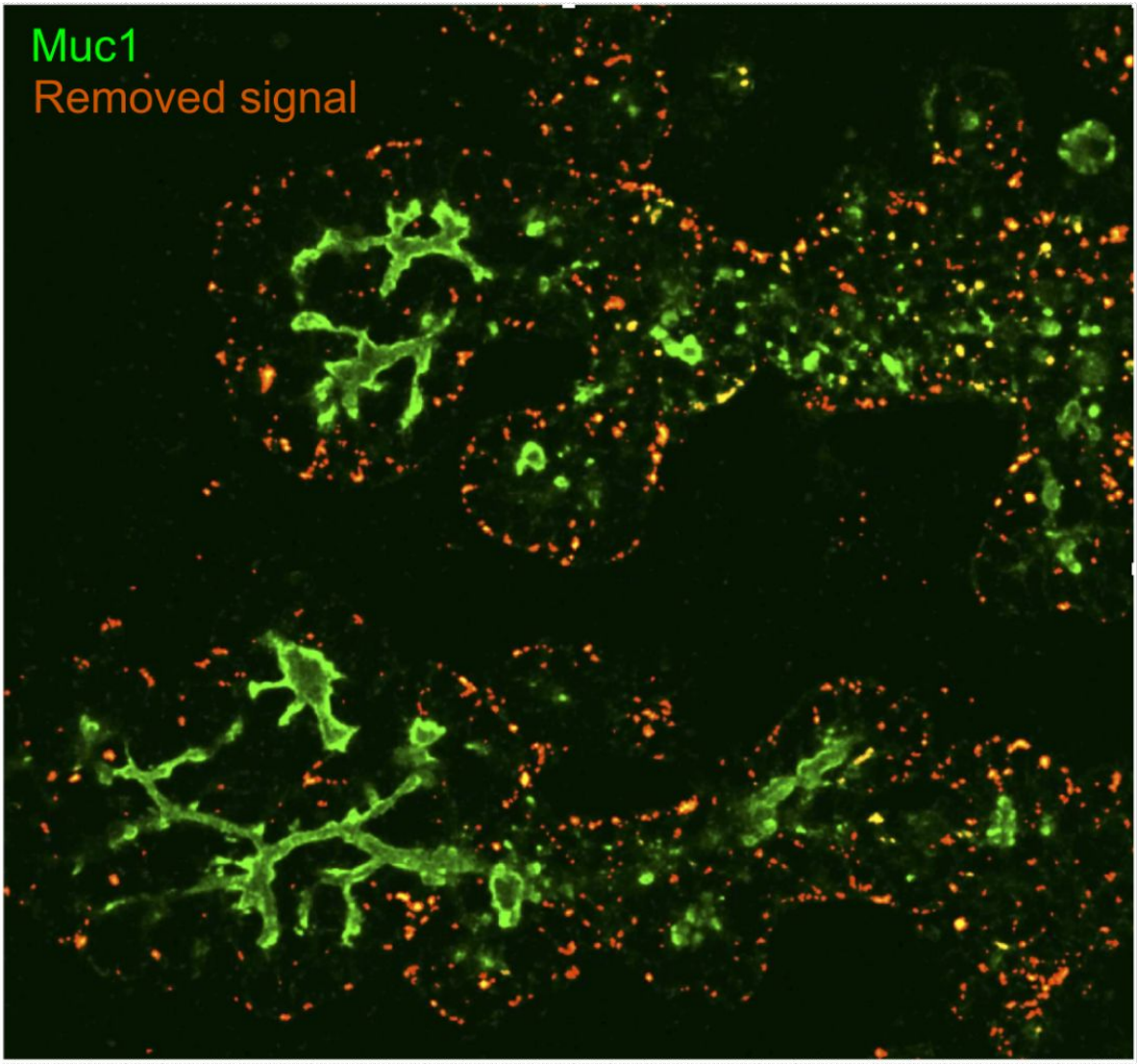
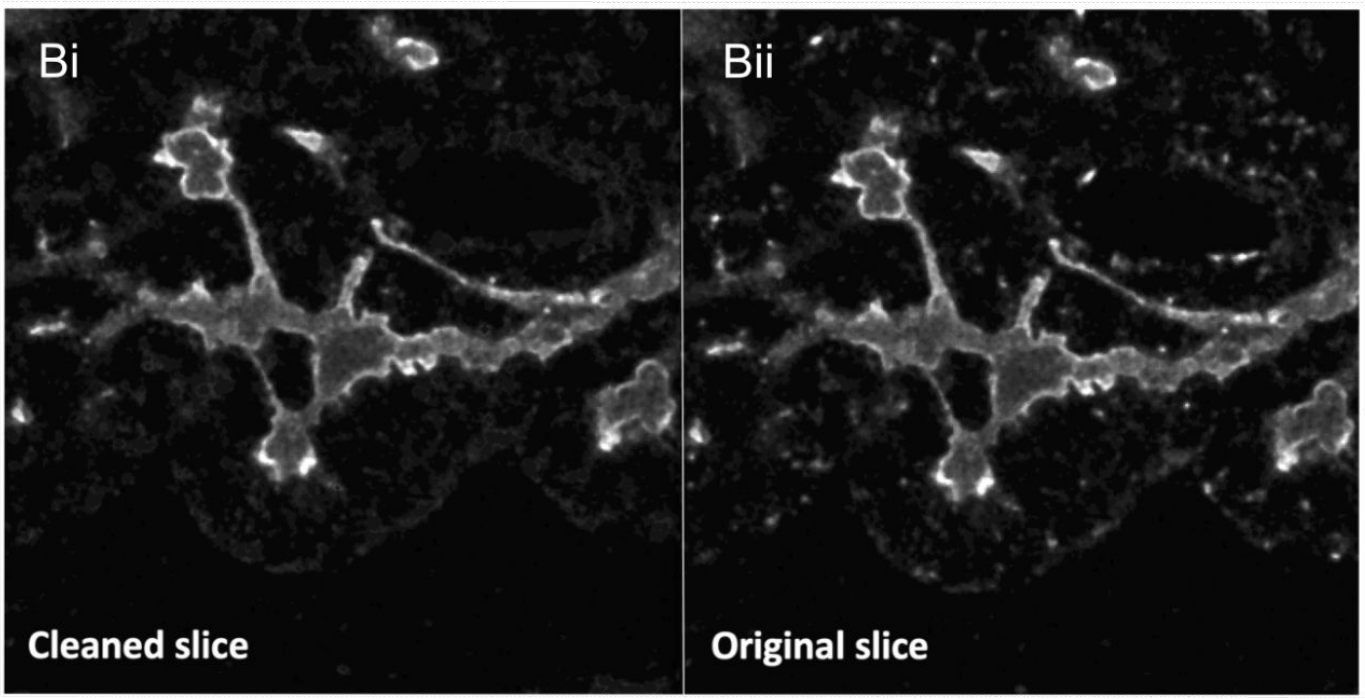
B